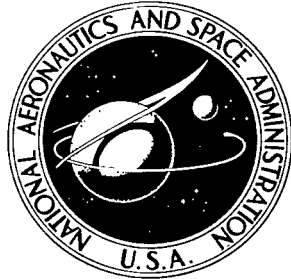


NASA TECHNICAL NOTE



NASA TN D-5399

C.1

NASA TN D-5399



LOAN COPY: RETURN TO  
AFWL (WL-2)  
KIRTLAND AFB, N MEX

# ENTRY AERODYNAMICS AT LUNAR RETURN CONDITIONS OBTAINED FROM THE FLIGHT OF APOLLO 4 (AS-501)

by Ernest R. Hillje

*Manned Spacecraft Center  
Houston, Texas*

NATIONAL AERONAUTICS AND SPACE ADMINISTRATION • WASHINGTON, D. C. • OCTOBER 1969

TECH LIBRARY KAFB, NM



0132214

**ENTRY AERODYNAMICS AT LUNAR RETURN CONDITIONS OBTAINED  
FROM THE FLIGHT OF APOLLO 4 (AS-501)**

By Ernest R. Hillje

Manned Spacecraft Center  
Houston, Texas

**NATIONAL AERONAUTICS AND SPACE ADMINISTRATION**

---

For sale by the Clearinghouse for Federal Scientific and Technical Information  
Springfield, Virginia 22151 — Price \$3.00

## ABSTRACT

The flight aerodynamic characteristics of the Apollo 4 entry configuration (Command Module 017) were calculated from onboard-recorded inertial-platform accelerations and attitudes and from reconstructed trajectory data. Modified trim-wind-tunnel data and hybrid data (modified wind-tunnel data adjusted to the flight-derived angle of attack) were compared to the flight-derived aerodynamics.

Comparison of the modified trim-wind-tunnel data to flight-derived data showed the initial trim angle of attack to be lower by approximately  $1.5^\circ$  and the resultant lift-to-drag ratio to be higher by approximately 10 percent. The flight-derived lift-to-drag ratio and the angles of attack in the hypersonic region were essentially linear with Mach number down to 6.0, at which point comparison of the modified trim-wind-tunnel data to flight-derived data showed much better agreement.

## TABLE OF CONTENTS

Section	Page
SUMMARY . . . . .	1
INTRODUCTION . . . . .	1
SYMBOLS . . . . .	3
MISSION DESCRIPTION . . . . .	5
ATMOSPHERIC ENTRY . . . . .	6
Entry Control . . . . .	6
Reconstructed Trajectory . . . . .	7
ENTRY-VEHICLE CONFIGURATION . . . . .	7
MODIFIED TRIM-WIND-TUNNEL DATA . . . . .	8
FLIGHT-DERIVED AERODYNAMICS . . . . .	9
Data Reduction Program . . . . .	9
Accuracy Assessment . . . . .	11
Hybrid Aerodynamic Data . . . . .	12
RESULTS AND DISCUSSION . . . . .	12
Factors Influencing the Data Comparisons . . . . .	13
Aerodynamic-Angles Data . . . . .	14
Lift-to-Drag-Ratio Data . . . . .	15
Aerodynamic Stability-Axis Force-Coefficient Data . . . . .	16
Aerodynamic Body-Axis Force-Coefficient Data . . . . .	19
CONCLUSIONS . . . . .	20
REFERENCES . . . . .	22

## TABLES

Table	Page
I SIGNIFICANT EVENTS DURING ENTRY . . . . .	23
II ESTIMATED COMMAND-MODULE CENTER OF GRAVITY AND MASS CHANGE DURING ENTRY . . . . .	24
III FLIGHT-DERIVED DATA INPUT REQUIREMENTS . . . . .	25

## FIGURES

Figure	Page
1      Apollo 4 mission profile	
(a) Launch into earth parking orbit . . . . .	26
(b) Injection into earth-intersecting coast ellipse . . . . .	27
(c) Atmospheric entry . . . . .	28
2      Apollo 4 launch vehicle configuration . . . . .	29
3      Recovery of the CM-017 forward heat shield . . . . .	30
4      The CM-017 shortly after landing, showing one main parachute still attached . . . . .	31
5      The CM-017 being hoisted aboard the recovery ship U.S.S. Bennington . . . . .	32
6      Entry trajectory control programs	
(a) Apollo guidance computer entry control . . . . .	33
(b) Bank-angle time history . . . . .	34
7      Time histories of trajectory parameters for atmospheric entry phase	
(a) Altitude $h$ , longitude $\theta_{GD}$ , and geodetic latitude $\phi_{GD}$ . . . . .	35
(b) Earth relative velocity $V$ , flight-path angle $\gamma$ , and azimuth $\sigma$ . . . . .	36
(c) Deceleration load factor $L_f$ . . . . .	37
8      Time histories of trajectory/atmosphere data	
(a) Dynamic pressure . . . . .	38
(b) Mach number $M_\infty$ . . . . .	39
(c) Reynolds number . . . . .	40
9      Command Module 017 external configuration. All linear dimensions are in inches	
(a) View looking aft . . . . .	41
(b) Side view. X-stations are in inches . . . . .	42
(c) View looking forward. Pad numbers are shown in circles . . . . .	43
(d) Detail of shear/compression pads. Dimensions are only approximate (in inches) . . . . .	44
(e) Details of umbilical system . . . . .	45

Figure	Page
(f) Exaggerated view of a cross section of the aft heat shield taken in the X-Z plane . . . . .	46
(g) Preflight photograph of CM-017 umbilical housing and ramp . . . . .	47
(h) Postflight photograph of CM-017 umbilical housing and ramp . . . . .	48
(i) Overall photograph of CM-017 on deck of recovery ship . . . . .	49
 10 Comparison of Apollo entry flow conditions with ground-facility capabilities . . . . .	50
 11 Formulation of modified trim-wind-tunnel and hybrid aerodynamic data . . . . .	51
 12 Body-axis system showing positive directions of aerodynamic angles and aerodynamic body force coefficients . . . . .	52
 13 Variation of modified wind-tunnel drag coefficient $C_D$ with modified wind-tunnel angle of attack $\alpha$ for $M_\infty = 6.0$ . . . . .	53
 14 Time histories of aerodynamic angles	
(a) Angle of attack $\alpha$ . . . . .	54
(b) Angle of sideslip $\beta$ . . . . .	55
(c) Aerodynamic roll angle $\phi_A$ . . . . .	56
(d) Resultant angle of attack $\alpha_R$ . . . . .	57
 15 Resultant angle of attack $\alpha_R$ plotted against Mach number $M_\infty$ . . . . .	58
 16 Time histories of lift-to-drag ratios	
(a) Vertical lift-to-drag ratio $(L/D)_V$ . . . . .	59
(b) Horizontal lift-to-drag ratio $(L/D)_H$ . . . . .	60
(c) Flight-derived resultant lift-to-drag ratio $(L/D)_R$ . . . . .	61
(d) Hybrid resultant lift-to-drag ratio $(L/D)_R$ . . . . .	62
 17 Resultant lift-to-drag ratio $(L/D)_R$ plotted against Mach number $M_\infty$	
(a) Flight-derived lift-to-drag ratio $(L/D)_R$ . . . . .	63
(b) Hybrid lift-to-drag ratio $(L/D)_R$ . . . . .	64

Figure		Page
18	Time histories of aerodynamic stability-axis force coefficients	
(a)	Vertical lift coefficient $C_{L,V}$ . . . . .	65
(b)	Horizontal lift coefficient $C_{L,H}$ . . . . .	66
(c)	Drag coefficient $C_D$ . . . . .	67
(d)	Resultant lift coefficient $C_{L,R}$ . . . . .	68
19	Time histories of aerodynamic body-axis force coefficients	
(a)	Axial-force coefficient $C_A$ . . . . .	69
(b)	Resultant normal-force coefficient $C_{N,R}$ . . . . .	70
(c)	Side-force coefficient $C_Y$ . . . . .	71
(d)	Normal-force coefficient $C_N$ . . . . .	72

ENTRY AERODYNAMICS AT LUNAR RETURN CONDITIONS OBTAINED  
FROM THE FLIGHT OF APOLLO 4 (AS-501)

By Ernest R. Hillje  
Manned Spacecraft Center

SUMMARY

Flight-derived aerodynamic characteristics of the Apollo 4 entry configuration have been obtained at lunar return conditions. Aerodynamic angles, lift-to-drag ratios, body-axis force coefficients, and stability-axis force coefficients were calculated from corrected onboard-recorded inertial-platform accelerations and attitudes and from a postflight-reconstructed entry trajectory. Modified trim-wind-tunnel data and hybrid data (modified wind-tunnel data adjusted to the flight-derived angle of attack) are presented for comparison purposes.

Comparison of the modified trim-wind-tunnel data with flight-derived data showed the initial trim angle of attack to be lower by approximately  $1.5^\circ$  and the resultant lift-to-drag ratio to be higher by approximately 10 percent. The flight-derived lift-to-drag ratio and angles of attack were essentially linear with Mach number down to 6.0, at which point comparison of the modified trim-wind-tunnel data to flight-derived data showed much better agreement (3 percent lower and  $0.5^\circ$  higher, respectively). The same trends existed in the flight-derived data of the previous Apollo mission (AS-202). In the transonic region, there were areas of poor agreement which could be the result of flight-data accuracy or of the influence of vehicle dynamics, or of both.

Comparisons of the modified trim-wind-tunnel data and the hybrid data to the flight-derived data indicated that the modified trim-wind-tunnel force data were reliable even at the initial-entry, high-Mach-number, low-Reynolds-number conditions. However, this comparison indicated that the modified wind-tunnel-determined trim attitudes were poor in the initial-entry hypersonic region and possibly in the transonic region.

INTRODUCTION

The Apollo command module (CM), or entry configuration, is essentially a blunted cone with a spherical-segment base. On the homeward leg of the journey through space, immediately prior to reaching the entry interface (400 000 feet), the spacecraft is oriented at a predicted aerodynamic trim attitude with the blunt base, or aft heat shield, forward. The blunt design produces the drag necessary to efficiently dissipate the kinetic energy associated with velocities of the lunar return mission. In addition, the configuration has an offset center of gravity (c.g.) to obtain the lift necessary to ensure

a sufficiently wide entry corridor and to exercise control of the landing point. The center of gravity for each flight is determined by preflight weight and balance procedures. To determine the best design and construction of a vehicle to withstand such extreme conditions, an extensive wind-tunnel testing program was initiated in early 1962.

Although a variety of facilities was used, no combination of the available facilities could provide a complete simulation of the pressure, temperature, and velocity levels experienced during an actual lunar return entry. To form a consistent set of wind-tunnel data, the results from the various facilities of the testing program were analyzed and faired with both Mach number and angle of attack. The data were then extrapolated to the highest expected flight Mach numbers, for which ground-facility data were not available. It was also necessary to modify the aerodynamic characteristics to account for differences (such as in external protuberances) between the flight configuration and the tested models and to account for asymmetry of the ablative material applied to the heat shield.

The Apollo space-flight test program began with two unmanned flights from Cape Kennedy, Florida, with uprated Saturn I launch vehicles. The first Apollo space flight (AS-201) occurred February 26, 1966, with CM-009 as the entry vehicle. Because a sophisticated inertial-measurement system was not required on this mission, a detailed determination of the aerodynamic characteristics of the entry vehicle was precluded.

The second space-flight test, Apollo mission AS-202, occurred August 25, 1966, with CM-011 as the entry configuration. Flight data in the form of inertial-platform attitudes and accelerations and a trajectory that was reconstructed from a combination of guidance-and-navigation (G&N) and radar-tracking data were used to calculate the entry flight-derived aerodynamic characteristics for AS-202. These flight results were compared with existing ground-facility data.

The third space-flight test, the Apollo 4 mission (AS-501), which used a Saturn V launch vehicle for the first time, was successfully accomplished November 9, 1967. This unmanned mission used CM-017, which had a heat shield designed to withstand lunar mission entry velocities. The principal objectives of the Apollo 4 mission were to demonstrate the structural and thermal integrity of the space vehicle and to verify the adequacy of the heat shield when subjected to entry at lunar return flight conditions. To reach lunar return flight conditions, the service propulsion system (SPS) engines were fired, and an entry velocity of 36 545 ft/sec was obtained.

The purpose of this report is to present the flight-derived aerodynamics for the Apollo 4 mission and to make comparisons with both the modified trim-wind-tunnel data and the hybrid data. The flight-derived aerodynamic force coefficients and ratios are presented relative to the osculating plane and in the stability-axis and the body-axis systems. Flight-derived force-coefficient data, based on dynamic pressure obtained from both a standard-atmosphere model and flight-measured pressures, are presented.

## SYMBOLS

$A_x, A_y, A_z$	acceleration along the body X-, Y-, and Z-axes, $\text{ft/sec}^2$
$A_{x,p}, A_{y,p}, A_{z,p}$	acceleration from the X-, Y-, and Z-axes of the inertial platform, $\text{ft/sec}^2$
$C_A$	aerodynamic body-axis axial-force coefficient, $-mA_x/q_\infty S$
$C_D$	aerodynamic drag coefficient
$C_{L,H}$	horizontal component of the lift coefficient relative to the orbital plane
$C_{L,R}$	resultant, or total, aerodynamic lift coefficient, $\sqrt{C_{L,H}^2 + C_{L,V}^2}$
$C_{L,V}$	vertical component of the lift coefficient relative to the orbital plane
$C_N$	aerodynamic body-axis normal-force coefficient, $-mA_z/q_\infty S$
$C_{N,R}$	aerodynamic body-axis resultant, or total, normal-force $\text{coefficient, } \sqrt{C_Y^2 + C_N^2}$
$C_{p,t}$	stagnation-pressure coefficient
$C_Y$	aerodynamic body-axis side-force coefficient, $mA_y/q_\infty S$
$d$	spacecraft reference diameter, 12.833 ft
$g$	acceleration of gravity at the surface of the earth, $32.1740 \text{ ft/sec}^2$
$h$	altitude, ft
$L_f$	deceleration load factor, $\sqrt{A_x^2 + A_y^2 + A_z^2/g}$
$L/D$	lift-to-drag ratio
$(L/D)_H$	horizontal component of the lift-to-drag ratio relative to the orbital plane, $C_{L,H}/C_D$

$(L/D)_R$	resultant (or total) lift-to-drag ratio, $C_{L,R}/C_D$
$(L/D)_V$	vertical component of lift-to-drag ratio relative to the orbital plane, $C_{L,V}/C_D$
$M_\infty$	Mach number
m	spacecraft mass, slugs
$p_t$	stagnation pressure, psia
$p_\infty$	free-stream pressure, psia
$q_\infty$	free-stream dynamic pressure, $\text{lb}/\text{ft}^2$
$q_\infty, p$	dynamic pressure based on flight pressure measurements, $\text{lb}/\text{ft}^2$
$Re_{2,d}$	Reynolds number behind the normal shock, based on d
$Re_\infty, d$	free-stream Reynolds number, based on d
S	reference area, $129.35 \text{ ft}^2$
t	elapsed time from the time of range zero, which is the first integral second of range time prior to the instant of Saturn instrument-unit umbilical disconnect, sec
u, v, w	individual components of spacecraft velocity with respect to the airstream along the body X-, Y-, and Z-axes, respectively, $\text{ft/sec}$
V	earth-relative spacecraft velocity, $\text{ft/sec}$
X, Y, Z	body-axis system (unless otherwise noted)
$\alpha$	angle of attack, deg
$\alpha_R$	resultant (or total) angle of attack, deg
$\beta$	angle of sideslip, deg
$\gamma$	flight-path angle of V relative to the local horizontal (positive up), deg

$\theta_C$	angle of radial plane measured about spacecraft X-axis, deg
$\theta_{GD}$	spacecraft longitude, deg
$\gamma, \phi, \psi$	gimbal angles of the inertial platform in pitch, roll, and yaw, respectively, deg
$\rho_2$	density of air behind the normal shock, slugs/ft <sup>3</sup>
$\rho_\infty$	free-stream density of air, slugs/ft <sup>3</sup>
$\sigma$	azimuth of V measured clockwise from north, deg
$\phi_A$	aerodynamic roll angle, deg
$\phi_{GD}$	spacecraft geodetic latitude, deg

Subscript:

$\infty$  free stream

## MISSION DESCRIPTION

The purpose of the Apollo 4 mission was to demonstrate the structural compatibility of the Saturn V launch vehicle with the spacecraft during the Saturn V launch conditions and to verify the adequacy of the heat shield when subjected to lunar return flight conditions. The Apollo 4 mission was the first launch of a Saturn V launch vehicle carrying an Apollo spacecraft. Launch occurred at 12:00:01 Greenwich mean time (G. m. t.) or 07:00:01 eastern standard time (e. s. t.) on November 9, 1967, from Complex 39A at Cape Kennedy, Florida. The launch window was restricted to the interval between 07:30 and 13:15 e. s. t. to provide both a daylight launch and at least 2 hours of daylight for CM recovery operations. Significant events along the mission trajectory are shown in figure 1. The launch phase included complete burns of the Saturn IC (S-IC) and Saturn II (S-II) stages and a partial burn of the Saturn IVB (S-IVB) stage (fig. 2). These burns resulted in a parking orbit of 101.1-nautical-mile apogee and 99.1-nautical-mile perigee. After approximately two orbits, the S-IVB stage reignited, placing the spacecraft into a simulated translunar trajectory. After the command and service module (CSM) separated from the S-IVB stage, the first firing of the SPS engine was performed. This firing represented a posigrade maneuver and resulted in a 9769-nautical-mile apogee coast ellipse.

Immediately before apogee, the state vector to initialize the navigation system for the second SPS burn and subsequent entry was updated in the Apollo guidance computer

(AGC). The second burn increased the velocity, duplicating the entry conditions that would result from a lunar return trajectory. Preflight trajectory simulations showed that an inertial flight-path angle of  $7.13^\circ$  below the horizontal ( $\pm 0.3^\circ$ ), a lift-to-drag ratio between 0.32 and 0.43, an inertial velocity of 36 333 ft/sec, and a target range of 2000 nautical miles would meet the minimum entry requirements. After the CM separated from the service module (SM), the guidance and control system began orienting the CM to the predetermined atmospheric-entry attitude of  $156.84^\circ$  angle of attack with the lift vector up. The spacecraft reached the entry interface (400 000 feet) at 08:19:28.5 ground elapsed time (g. e. t.) with an inertial velocity of 36 545 ft/sec and an inertial flight-path angle of  $-6.93^\circ$ . Landing occurred at 08:37:09.2 g. e. t., approximately 10 nautical miles from the planned landing point and approximately 550 nautical miles northwest of the Kauai, Hawaii, tracking station. The CM, the forward heat shield, and one of the three main parachutes (figs. 3 and 4) were hoisted aboard the primary recovery ship, the U.S.S. Bennington, approximately 2 hours 28 minutes after landing (fig. 5).

## ATMOSPHERIC ENTRY

### Entry Control

The entry aerodynamics for the Apollo CM are closely related to the AGC entry control logic (ref. 1); therefore, a brief description of the control programs is included (fig. 6(a)). After the CM separated from the SM and prior to reaching the entry interface at 400 000 feet, the spacecraft was oriented in pitch with its stability axis along the AGC-estimated relative wind-velocity vector with a bank-angle attitude of  $0^\circ$ , or lift up (fig. 6(b)). Pitch and yaw attitude control was maintained until 0.05g deceleration was reached. The spacecraft attitude was then maintained by aerodynamic forces and moments. Control of the rotational rates was retained in the rate damping mode. The roll rate gyro was coupled to the yaw electronics to give coordinated roll control about the velocity vector rather than about the spacecraft body X-axis. At the entry interface, the initial roll program of the INITIAL ENTRY phase was in command. The AGC estimated a 2084-nautical-mile inertial range to the targeted landing point and a 7.9-nautical-mile cross-range error at this time. When 0.05g was sensed (0.05g interface), the AGC automatically began the entry computations. A post-0.05g test determined if the lift vector, which was up initially, should be rolled down to ensure atmospheric capture. A decision was made to continue the flight with the lift vector up. When the aerodynamic deceleration level exceeded 0.2g and the altitude was decreasing at a rate less than 700 ft/sec, control was transferred to the HUNTEST phase. During the HUNTEST phase, steering was performed by a constant-drag routine until the difference between the desired and the predicted range was less than 25 nautical miles, and the predicted skip velocity was less than orbital velocity. To obtain the proper trajectory conditions, the Apollo 4 mission was flown lift vector down for approximately 22 seconds during the phase immediately after peak g. The UPCONTROL phase was entered at the same time that the lift vector was rolled back to lift vector up. In the UPCONTROL phase, the bank angle was controlled between  $40^\circ$  and  $90^\circ$  to provide the skip-velocity vector required to match the predicted range with the calculated range to target. Normally, the KEPLER, or BALLISTIC, phase would have been entered next, when the total deceleration had fallen below 0.2g. Since the spacecraft never reached this required condition during the UPCONTROL phase, the KEPLER phase was bypassed, and at a time near

the maximum skip altitude of 241 602 feet, the FINAL ENTRY phase was entered. In the FINAL ENTRY phase, or second entry, the CM was steered to the target point based on a linear perturbation about a stored reference trajectory. All steering calculations ended when the earth-relative velocity fell below 1000 ft/sec. At drogue parachute deployment time, the AGC indicated a target overshoot of 2.3 nautical miles. The times at which the AGC control phases occurred are given in table I. A more detailed analysis of the AGC performance during entry is given in reference 2.

### Reconstructed Trajectory

The trajectory data used in this paper are from the entry segment of the reconstructed trajectory that represents the Apollo 4 mission profile (ref. 3) from ignition of the S-IVB stage to splashdown (fig. 1). The entry segment of the reconstructed trajectory, or best-estimate trajectory (BET), is essentially a CM G&N trajectory corrected for CM inertial-measurement-unit (IMU) errors. The BET was made to fit significant events during the atmospheric-entry portion of the mission. The IMU corrections were determined by comparing data obtained from several independent sources during previous segments of the mission profile. The primary source, the Apollo CM G&N onboard trajectory data, was compared with radar tracking data (Manned Space Flight Network, C-band, unified S-band, and skin track), down-link telemetry data (S-IVB stage inertial unit and the CSM IMU), and high-speed radar tracking data from the Eastern Test Range (used during both the ascent phase and the second S-IVB stage engine burn). The event data that were matched near termination of the flight were time, as determined from baroswitch closure time, and altitude for the drogue and main parachute deployment, as determined from baroswitch pressure altitude presettings. The CM descent characteristics, based on previous experience, and the impact point coordinates, based on the recovery ship estimate, were then used to complete the BET to splashdown. The atmospheric data used were from the 15° north annual model of reference 4. This model was recommended for its similarity to rawinsonde (balloon) data obtained from Eniwetok Atoll, Marshall Islands, on the same day the Apollo 4 mission was flown. Trajectory data are presented in figure 7 as time histories of spacecraft position (altitude  $h$ , longitude  $\theta_{GD}$ , and geodetic latitude  $\phi_{GD}$ ), space-craft earth-relative velocity vector (velocity  $V$ , flight-path angle  $\gamma$ , and azimuth  $\sigma$ ), and deceleration load factor  $L_f$ . Time histories of data that require a definition of the atmosphere, as well as of trajectory data, are presented for dynamic pressure  $q_\infty$ , Mach number  $M_\infty$ , and Reynolds number (free-stream Reynolds number  $Re_{\infty, d}$ , and Reynolds number behind the normal shock  $Re_{2, d}$ ) in figure 8.

### ENTRY-VEHICLE CONFIGURATION

The CM-017 external configuration is shown in figure 9. Figures 9(a), 9(b), and 9(c) are detailed drawings of CM-017 showing all larger external projections, particularly the aft heat-shield projections which could affect airflow during atmospheric entry. In general, the spacecraft consists of three distinct sections termed forward, aft, and crew compartments, as indicated in the side view. Structural members and insulation

material join the heat shields to the primary internal structure. The forward and aft heat shields are continuous structures coated with an ablative material. The central heat shield (crew compartment) consists of a series of externally applied segments which are mechanically fastened to the primary structure. Some segments are removable to provide exterior access to the aft-compartment equipment.

As shown in figure 9(c), the aft heat shield has six compression or shear pads, or both, arranged in a circular pattern. These pads (fig. 9(d)), join the CM to the SM and are designed to transmit axial thrust loads acting either from or through the SM. The relative positions of the umbilical housing and the umbilical ramp are also shown in figure 9(c). Details A and B and section D-D of figure 9(e) describe the housing and ramp in detail.

Figure 9(f) is an exaggerated view showing a cross section of the aft heat shield taken in the X-Z plane. The center line of the aft heat shield shows a slight divergence from the structural CM center line. The heat shield reaches a maximum thickness of approximately 2.7 inches near the theoretical hypersonic stagnation point. The heat shield is then smoothed to a thickness of approximately 1.5 inches at the tangent point of the CM torus in the negative Z-direction. In the positive Z-direction at the tangent point of the torus, the thickness is approximately 1.6 inches.

#### MODIFIED TRIM-WIND-TUNNEL DATA

The modified trim-wind-tunnel data resulted from an analysis of smooth, symmetrical, CM ground-facility data which were adjusted to fit the specific entry flight configuration (CM-017) of the Apollo 4 mission. The Apollo wind-tunnel testing-program data (refs. 5 to 9) were faired with both Mach number and angle of attack to form a set of data consistent among the test facilities and test conditions. Because no data were obtained in the initial-entry, high-Mach-number, low-Reynolds-number flight regime (fig. 10), it was necessary to extrapolate the preflight data to this region.

Modifications were then made to adjust for the differences between the flight configuration and the tested models. The protuberances that would affect the aerodynamics are shown in figure 9. The significant effect was a change in the pitch- and yaw-moment coefficients (and consequently in the wind-tunnel-measured trim angles). This change was caused by the umbilical housing and ramp. In addition, because an unsymmetrical configuration results from the variable thickness of the ablative material on the aft heat shield, an analytical approximation of the change in trim angle of attack was made to correct for the effective cant angle between the center line of the forebody structure and the center line of the approximated ablative sphere. The approximation of the change to the trim angle of attack was extended to account for the effective offset (measured at the surface of the heat shield) between the respective center lines.

To properly correlate the modified trim-wind-tunnel data to the flight data, the same reference c. g. must be used. During atmospheric entry, the CM reaction control subsystem (RCS) used approximately 90 pounds of propellant to control the roll attitude of the spacecraft and to damp any spacecraft rates that were greater than the dead-band limits of  $\pm 2.0$  deg/sec for all the rate channels (pitch, yaw, and roll). In addition,

during entry, the spacecraft exchanges heat with the atmosphere by partial burnoff of the ablative material. A predicted weight loss using the postflight trajectory indicated that approximately 210 pounds were expended. The propellant and ablative-material weight losses were accounted for in determining the time history of the c.g. and the mass of the spacecraft. Modified trim-wind-tunnel data were then transferred to the flight c.g. values for the events and Mach numbers given in table II. Since the Y-axis c.g. movement was negligible during entry, it was taken as a constant. The Y-axis c.g. offset caused the spacecraft to trim about a plane that was offset rotationally from the spacecraft X-Z (pitch) plane. The modified trim-wind-tunnel data are presented for the flight c.g. and are referenced to the offset plane. Consequently, the comparison with the flight-derived data is restricted to data in the resultant angle-of-attack  $\alpha_R$  plane.

The basic wind-tunnel data, with modifications (fig. 11), represent the prediction of the CM trim aerodynamic characteristics based on ground-facility and analytical (as opposed to flight-derived) data. Flight-derived aerodynamic data available from a previous Apollo mission (ref. 10) were used to adjust the preflight-predicted aerodynamics for the Apollo 4 mission; however, these data are not presented in this paper so that a valid assessment of the modified trim-wind-tunnel data can be made, by comparison with the flight-derived data.

## FLIGHT-DERIVED AERODYNAMICS

### Data-Reduction Program

Flight-derived aerodynamic data were obtained from two major sources. The first source was the IMU, which included onboard-recorded data from accelerometers on the inertial platform and data from attitude sensors of the three IMU gimbals. The second major source of data was the reconstructed entry trajectory, or BET. From this source, the data-reduction program obtained the velocity and position of the spacecraft and the atmospheric state variables needed for the aerodynamic-coefficient calculations and for the correlation parameters.

The aerodynamic angles were calculated using the following relationships:

$$\alpha = \tan^{-1}\left(\frac{w}{u}\right) \quad (1)$$

$$\beta = \tan^{-1}\left(\frac{v}{\sqrt{u^2 + w^2}}\right) \quad (2)$$

$$\alpha_R = \tan^{-1}\left(\frac{\sqrt{v^2 + w^2}}{u}\right) \quad (3)$$

$$\phi_A = \tan^{-1} \left( \frac{v}{w} \right) \quad (4)$$

The velocities  $u$ ,  $v$ , and  $w$  in the body-axis frame (fig. 12) were obtained by rotating the earth-relative velocity vector through the earth-centered inertial and the inertial-platform axis systems to the body-axis system. This calculation required the earth-relative velocity vector and spacecraft position from the BET data, the IMU alignment on the launch pad, the g.e.t., and the IMU gimbal angles.

The aerodynamic force coefficients  $C_{L,R}$  and  $C_D$  were calculated by transforming the inertial-platform accelerations into the stability-axis frame and then by multiplying these by the ratio of spacecraft mass to the product of the dynamic pressure and reference area. The vertical and horizontal lift coefficients required an additional set of data (earth-relative flight-path angle and azimuth) to obtain the components of lift relative to the earth, or orbital plane. Spacecraft mass, dynamic pressure, and IMU gimbal-angle data were required to transform the platform accelerations into the body frame, so that the body-axis coefficients could be calculated.

Because flight stagnation-pressure  $p_t$  measurements were available, all coefficient calculations were based on both the dynamic pressure obtained from the BET, where

$$q_\infty = \frac{1}{2} \rho_\infty V^2 \quad (5)$$

and on the flight dynamic pressure determined from the following equation

$$q_\infty, p = \frac{p_t - p_\infty}{C_{p,t}} \quad (6)$$

Above  $M_\infty \approx 7$ , the stagnation-pressure coefficient

$$C_{p,t} = 2 - \frac{\rho_\infty}{\rho_2} \quad (7)$$

where the density ratio  $\rho_\infty/\rho_2$  was obtained from reference 11. Below  $M_\infty \approx 7$

$$C_{p,t} = \frac{\frac{p_t}{p_\infty} - 1}{0.7M_\infty^2} \quad (8)$$

where the pressure ratio  $p_t/p_\infty$  was obtained from reference 12, and the Mach number was obtained from the BET. These calculations of dynamic pressure are given in figure 8(a) and show reasonably good agreement. The lift-to-drag ratios were calculated directly from the coefficients and are independent of dynamic pressure. Data required for the individual flight-derived aerodynamic parameter calculations are given in table III.

The data-reduction program makes corrections for all systematic errors in the input data. These errors originate either from the detailed postflight analysis of the specific systems, such as the analysis made for the IMU data (ref. 13), or from analysis of the measurement involved.

#### Accuracy Assessment

The accuracy with which the flight-derived data can be determined depends on both the input measurement uncertainty about a mean value (measurement precision) and the closeness of the measurement to the true value (measurement accuracy). The input data were corrected for all detectable systematic errors determined postflight. The measurement precision was evaluated in an error analysis that was performed (ref. 14) to obtain a statistical determination of the probable system error. The method selected was a root-sum-square approach based on the Central Limit Theorem. The error analysis included more than 30 independent error sources that affected the following: inertial-platform alinement, inertial-platform accelerometer measurements, IMU gimbal-angle data, flight-measured stagnation-pressure data, atmospheric wind data, initial-velocity determination, and spacecraft mass.

The results of reference 14 show that the standard deviation in the resultant lift-to-drag ratio  $(L/D)_R$  was less than  $\pm 0.008$  (approximately 2 percent) for most of the Apollo 4 mission down to  $M_\infty \approx 13$ . The uncertainty band then increased rapidly because of the combined effects of propagating the inertial-platform errors through the entire entry phase and because of the possibility of low-altitude winds.

The uncertainty in the aerodynamic angles was  $\pm 3^\circ$  (except for  $\phi_A$  which was  $\pm 7^\circ$ ), down to  $M_\infty \approx 6$ , at which point these uncertainties begin to increase until they reach values of  $\pm 15^\circ$ ,  $\pm 18^\circ$ ,  $\pm 15^\circ$ , and  $\pm 40^\circ$  for  $\beta$ ,  $\alpha$ ,  $\alpha_R$ , and  $\phi_A$ , respectively, at drogue parachute deployment time. The large uncertainty in the flight aerodynamic

force coefficients based on  $q_{\infty, p}$  resulted from the uncertainty in pressure-transducer measurements, except in regions of high dynamic pressures. In the region of maximum dynamic pressure, the uncertainties in  $C_D$ ,  $C_{L,R}$ ,  $C_A$ , and  $C_{N,R}$  were  $\pm 0.04$ ,  $\pm 0.02$ ,  $\pm 0.045$ , and  $\pm 0.048$ , respectively. These standard deviations (taken in the hypersonic region for  $(L/D)_R$  and  $\alpha_R$ ) were used as the basis of the statements about the agreement of the various data sets made in the section of this report entitled "Results and Discussion."

### Hybrid Aerodynamic Data

The modified trim-wind-tunnel data represent the predicted entry configuration aerodynamics at the flight-estimated c.g. To eliminate the dependence of the modified wind-tunnel-force data on these trim attitudes, an additional set of data was generated. These hybrid aerodynamic data were formed by obtaining a flight-derived angle of attack and trajectory Mach number for each flight-data point and interpolating the modified wind-tunnel data as a function of test angle of attack and test Mach number (fig. 11). This produced the hybrid aerodynamic force coefficient and lift-to-drag-ratio data. As an example, a hybrid value for  $C_D$ , at flight time  $t = 30\ 506$  seconds, where the flight-derived  $\alpha_R = 151.96^\circ$  and the trajectory Mach number  $M_{\infty} = 6.0$ , may be obtained from figure 13, which shows the variation of the modified wind-tunnel  $C_D$  with test angle of attack for  $M_{\infty} = 6.0$ . The value of the modified wind-tunnel  $C_D$  at the modified wind-tunnel trim angle is also shown in figure 13.

The hybrid data were compared to both the flight-derived and the modified trim-wind-tunnel aerodynamic data where appropriate. This type of data (hybrid) was first presented in reference 10 for CM-011 (Apollo mission AS-202). These data indicated that the poor prediction of  $(L/D)_R$  at the higher Mach numbers, which occurred during AS-202, was the result of poor estimates of the trim attitude derived from the modified wind-tunnel data, and not the result of errors in the modified wind-tunnel force coefficient data.

### RESULTS AND DISCUSSION

Flight-derived data are grouped by aerodynamic angles (figs. 14 and 15), lift-to-drag ratios (figs. 16 and 17), aerodynamic stability-axis force coefficients (fig. 18), and aerodynamic body-axis force coefficients (fig. 19). Comparison is made in all groups, wherever appropriate, with modified trim-wind-tunnel and hybrid data. In addition, flight-derived aerodynamic force coefficient data, based on dynamic pressure determined from the flight-derived stagnation pressure, are included in figures 18 and 19.

## Factors Influencing the Data Comparisons

Influencing factors, or data peculiarities, may affect the comparison of flight-derived, modified trim-wind-tunnel, and hybrid data. Data peculiarities can be grouped by source of data (modified trim-wind tunnel, hybrid, and flight-derived) and by type of data (aerodynamic angle, aerodynamic lift-to-drag ratio, and aerodynamic force coefficient). The following are some of the more pronounced factors:

1. In comparing the flight-derived aerodynamics, which are a function of time, to the modified trim-wind-tunnel data, which are a function of the test-facility conditions, a correlation parameter must be chosen. Mach number is the obvious choice because it is a basic, simply calculated flow parameter and because it is widely used in the field of aerodynamics. Flow conditions in the ground-test facilities can be stringently controlled; therefore, the Mach number for the modified trim-wind-tunnel data is relatively accurate (ref. 6). The flight Mach number obtained from the BET data, however, depends on the trajectory altitude and the model atmosphere, both of which can be subject to large uncertainties. Consequently, the flight-derived Mach number (and the other trajectory-atmosphere-dependent parameters) cannot be considered as accurate as the Mach number presented for the modified trim-wind-tunnel data. This factor influences all aerodynamic data comparisons.

2. The ground-facility data, which represent a steady-state condition, indicate that there are flow regions in which the aerodynamic-trim values undergo many changes. In actual flight, these regions are traversed rapidly. Before a steady-state trim attitude can be established for the flow condition of the static data, the vehicle encounters a different flow environment. Therefore, at a given Mach number, the flight-derived aerodynamic-trim values may differ considerably from wind-tunnel steady-state values. There are also times when the flight-derived data may reflect a transient response to dynamic conditions encountered. This transient response occurs in the region of RCS engine firing, in flow regions where negative damping is present, or in the region of the transonic-flow regime and affects the comparison of both hybrid data and modified trim-wind-tunnel data with the flight-derived data.

3. The comparison of the modified trim-wind-tunnel data and the flight-derived data is considered invalid where the atmosphere is too thin to trim the CM at a steady-state condition. Because of the typical Apollo skip-type entry trajectory, this situation can exist both in the region of the initial-entry interface (considered to begin at 400 000 feet) and during the skip region. (The skip region is also called the BALLISTIC, or KEPLER, phase in the AGC control terminology.) The flight-derived data presented in this paper for the Apollo 4 mission did not exhibit the relatively large amplitude excursions in the skip region that the previous mission (AS-202) exhibited (ref. 10). The Apollo 4 data show a lower skip altitude and higher velocity, which resulted in a higher dynamic pressure for the Apollo 4 mission. This was confirmed by the fact that the BALLISTIC phase of the AGC control logic was bypassed.

4. Flight-derived aerodynamic angles can be obtained for all entry times, even though the CM is not aerodynamically trimmed, because the data required for these calculations (IMU gimbal angles) are continuously available. Flight-derived aerodynamic forces, however, require sensed accelerations; therefore, in the initial-entry region, both the flight-derived aerodynamic force coefficients and the lift-to-drag ratios will exhibit much scatter. This condition lasts until the entry acceleration

builds up to measurable levels. This condition is also present in the skip region, with the degree of scatter being related to the skip altitude.

5. The flight-derived force data, in the form of averaged values (as opposed to instantaneous values), are obtained from pulse-integrating pendulous accelerometers which accumulate velocity changes (pulses) over a 2-second interval. The pulses are then averaged over this interval to obtain the accelerations. The flight-derived aerodynamic force coefficients and lift-to-drag ratios, therefore, may not show peak amplitudes that correspond to the peak amplitudes obtained from the flight-derived aerodynamic angles. This factor will influence the comparison of the flight-derived data with the hybrid data in that the hybrid data will show larger oscillation amplitudes. The comparison of the flight-derived data with the modified trim-wind-tunnel data will benefit from this influencing factor because the averaging effect of the flight accelerometers results in more of a mean value for the flight-derived aerodynamic force coefficient and lift-to-drag-ratio data.

6. The flight-derived force coefficients are calculated both from a dynamic pressure  $q_\infty$ , obtained from the trajectory velocity and a standard atmosphere model, and from a dynamic pressure  $q_\infty, p$ , calculated from the flight-measured stagnation-pressure data. If the flight-measured stagnation pressure  $p_t$  is at least 5 percent of the full-scale measurement value, the latter method should give a more accurate time history of dynamic pressure at the higher altitudes where model atmosphere uncertainties are traditionally large. (These regions of low  $p_t$  are noted on fig. 8(a)).

7. Flight-measured IMU gimbal-angle data, which are required for the calculation of the flight-derived aerodynamic angles and the body-axis force coefficients, were missing in several regions during entry. These missing data were calculated from trends and levels established from comparison with the backup attitude reference system. These flight-derived data points are noted in the figures by a flagged symbol. This procedure should not compromise the accuracy of the affected flight-derived data calculations. Table III indicates the aerodynamic parameters that are affected by the IMU gimbal-angle data  $\theta$ ,  $\psi$ ,  $\phi$ .

#### Aerodynamic-Angle Data

The aerodynamic angles defined in figure 12 are presented as time histories in figure 14. In figure 15,  $\alpha_R$  is repeated as a function of Mach number. The flight-derived data show that the spacecraft was not at the aerodynamic trim attitude at the entry interface; but as the spacecraft plunged into the thicker atmosphere, it soon became trimmed at  $\alpha \approx 154.5^\circ$  with  $\beta \approx 2^\circ$ . The point at which the CM was judged to be in a steady-state trim attitude was determined by comparing the flight-measured dynamics to six-degree-of-freedom trajectory simulation dynamics. The dynamic pressure, the deceleration load factor, and the altitude at which trim was obtained in the simulations were correlated with these flight data, which showed the estimated trim point to be  $t = 30\ 010$  seconds, where  $M_\infty \approx 38.0$ . At trim, the modified trim-wind-tunnel  $\alpha_R$  was approximately  $1.5^\circ$  lower than the flight-derived value of

$\alpha_R \approx 154.5^\circ$ . The flight  $\alpha_R$  then decreased almost linearly, with respect to the Mach number, to approximately  $153^\circ$  at  $M_\infty = 6.0$  and  $t = 30\ 505$  seconds. At this point, the modified trim-wind-tunnel value was approximately  $0.5^\circ$  higher than the flight-derived value. Agreement is alternately poor and good from this point in the trajectory to the end, with the difference in  $\alpha_R$  reaching  $10^\circ$  near  $M_\infty = 0.9$ . The region of poor agreement at transonic speeds is possibly the result of the uncertainty in the Mach number, the result of the comparison of static and dynamic data (data comparison influencing factors 1 and 2 in the section of this report entitled "Factors Influencing the Data Comparisons"), or the results of the accuracy of the flight-derived aerodynamic data.

### Lift-to-Drag-Ratio Data

The lift-to-drag ratio  $L/D$  is the most important aerodynamic parameter of concern to the trajectory control analyst. During the initial-entry phase, the available  $L/D$  is used in defining the entry corridor for the lunar return mission. In the period from initial entry to the time the spacecraft approaches the maximum-altitude point of the typical Apollo skip phase, the available  $L/D$  determines the ranging and maneuverability footprint potential. The flight-derived resultant lift-to-drag ratio  $(L/D)_R$  has been separated into a component in the osculating plane (vertical lift-to-drag ratio  $(L/D)_V$ ) and a component perpendicular to the osculating plane (horizontal lift-to-drag ratio  $(L/D)_H$ ). The  $(L/D)_V$  presented in figure 16(a) indicates that the spacecraft entered the atmosphere in the planned full-positive lift attitude and maintained this condition until the altitude rate was reduced to less than -700 ft/sec (fig. 6 and table I).

The subsequent AGC control phases, HUNTEST and UPCONTROL, shaped the trajectory so that the trajectory conditions necessary to prevent skip-out and to ensure enough ranging capability were attained. The  $(L/D)_V$  time history shows that, to ensure this ranging capability, a period of full-negative lift had to be flown shortly after the first peak  $g$  ( $t = 30\ 045$  seconds). This period was followed by a period of zero lift (bank angle of  $90^\circ$ ). The AGC determined that the KEPLER phase need not be used to acquire the range necessary to reach the target. Therefore, the FINAL ENTRY phase was entered approximately at the maximum skip altitude ( $t = 30\ 263$  seconds). The FINAL ENTRY phase used  $(L/D)_V$  values close to those the AGC control was designed to use. A comparison of cross-range error to the predicted lateral-ranging capability of the spacecraft determined the direction the spacecraft was rolled to modulate the  $(L/D)_R$  or, alternately, to generate an  $(L/D)_H$ . Figure 16(b) shows how the  $(L/D)_H$  was alternated so that the spacecraft would not incur any cross-range error at landing.

In figure 16(c), the flight-derived  $(L/D)_R$  is presented as a function of time and, in figure 17(a), as a function of Mach number. The flight-derived entry  $(L/D)_R$  was designated as the average value between the point at which the spacecraft is trimmed and the first peak  $g$  (which occurs at approximately the same time as pullup). The

spacecraft was judged to be in a steady-state trim attitude at  $t = 30\ 010$  seconds, and the first peak  $g$  occurred at  $t = 30\ 045$  seconds. Therefore, the average entry flight-derived  $(L/D)_R$  was 0.368. The modified trim-wind-tunnel  $(L/D)_R$ , which was approximately 10 percent higher during this period, showed only fair agreement. Shortly after the first peak  $g$ , the roll maneuver to negative lift and the return to positive lift were clearly accentuated by the flight-derived data scatter. The lowest hypersonic flight-derived  $(L/D)_R$  of 0.360 (data scatter points omitted) was reached during this period. The hypersonic  $(L/D)_R$  then increased almost linearly with respect to the decreasing Mach number and increasing flight time, reaching a value of  $(L/D)_R = 0.410$  at  $M_\infty = 6.0$  and  $t = 30\ 505$  seconds (similar to AS-202, ref. 10). The modified trim-wind-tunnel value was only 3 percent below the flight-derived value at  $M_\infty = 6.0$ .

The maneuvering region of the entry flight, where the majority of the trajectory shaping necessary to reach the targeted impact point is done, was the region between the first peak  $g$  ( $t = 30\ 045$  seconds) and the start of the AGC FINAL ENTRY control phase ( $t = 30\ 253$  seconds). The average flight-derived  $(L/D)_R$  in this region was 0.372. Below  $M_\infty = 6.0$ , agreement between flight-derived and modified trim-wind-tunnel data is good (within 5 percent) with two exceptions. In the transonic region ( $1.20 > M_\infty > 0.9$ ), the modified trim-wind-tunnel data show poor agreement with the flight-derived data. The peak modified trim-wind-tunnel  $(L/D)_R$  value is 0.64 (at  $M_\infty = 1.2$ ), which is approximately 25 percent higher than the peak flight-derived  $(L/D)_R$  of 0.505 in this region (at  $M_\infty = 1.13$ ). At  $M_\infty < 0.5$ , the difference is also approximately 25 percent.

The hybrid data (figs. 16(d) and 17(b)) can be used to assess the accuracy of the modified trim-wind-tunnel force data, because the hybrid data are not dependent on the trim attitudes obtained from the modified trim-wind-tunnel data. Comparison of the hybrid data with the flight-derived data in the hypersonic regime shows near-perfect agreement (0 to 5 percent), with essentially the same levels and the same linear trend with respect to time and Mach number. A comparison of figure 16(c) with figure 16(d) and figure 17(a) with figure 17(b) shows this near-perfect agreement. In the transonic region ( $M_\infty < 1.65$ ), agreement is only good to fair (5 to 15 percent). The good agreement of these two sets of data for most of the flight indicates that the modified trim-wind-tunnel data accurately represent the aerodynamic  $(L/D)_R$  variation with respect to  $\alpha_R$  at almost all Mach numbers, including the initial-entry, high-Mach-number ( $M_\infty \approx 38$ ), low-Reynolds-number ( $Re_{\infty, d} \approx 1.0 \times 10^4$ ) region.

#### Aerodynamic Stability-Axis Force-Coefficient Data

Time histories of the lift coefficients  $C_{L,V}$ ,  $C_{L,H}$ , and  $C_{L,R}$ , and the drag coefficient  $C_D$  are presented in figure 18. The trend of the flight-derived vertical and horizontal lift coefficients is identical to that exhibited by the vertical and

horizontal lift-to-drag ratios (figs. 16(a) and 16(b), respectively). The two sets of flight-derived coefficient data differ because of the differences in  $q_{\infty}$  and  $q_{\infty}, p$ .

In figure 18(c), the modified trim-wind-tunnel  $C_D$  is compared to the flight-derived  $C_D$  based on  $q_{\infty}, p$ . The modified trim-wind-tunnel  $C_D$  closely follows the flight-derived  $C_D$  (within 5 percent), starting lower in the high-hypersonic region, where the modified trim-wind-tunnel  $\alpha_R$  (fig. 14(d)) is lower than the flight-derived  $\alpha_R$ , and becoming higher at approximately the same time ( $t \approx 30\ 420$  seconds and  $M_{\infty} \approx 14$ ) that the modified trim-wind-tunnel  $\alpha_R$  crosses the flight-derived  $\alpha_R$ . The modified trim-wind-tunnel  $C_D$  is higher than the flight-derived  $C_D$  for the remainder of the flight, with large differences (10 to 15 percent) between data taken at  $M_{\infty} = 3.0$  and  $M_{\infty} = 1.35$  and below  $M_{\infty} = 0.9$ . The differences near the end of the flight (below  $M_{\infty} \approx 3.0$ ) are due to inaccurate determination of  $q_{\infty}, p$  which occurs for two known reasons. First, in this region, the slope of the pressure ratio  $p_t/p_{\infty}$ , designated a function of velocity, is steep; consequently, a small error in the velocity can result in a large error in  $p_t/p_{\infty}$ . Second, near the end of flight, the trim angle of attack, and therefore the stagnation point have changed (fig. 14(d)) so that the pressure sensor which was used to measure  $p_t$  may no longer be coincident with the stagnation point.

At hypersonic Mach numbers, the flight-derived  $C_D$  based on  $q_{\infty}$  (ref. 4) was within 7 percent of the flight-derived  $C_D$  based on  $q_{\infty}, p$ , with one exception. Where the altitude was above approximately 200 000 feet (fig. 7(a)), the flight-derived  $C_D$  based on  $q_{\infty}$  formed a symmetrical curve about the point of maximum-skip altitude. This curve, instead of the expected straight line, indicates that this model atmosphere is a poor fit in this altitude region or that the trajectory altitude is inaccurate in this altitude region, or both. Below  $M_{\infty} = 4.0$ , the modified trim-wind-tunnel data agree better with the trend of the flight-derived  $C_D$  based on  $q_{\infty}$  (within 5 percent) than with the trend of the flight-derived  $C_D$  based on  $q_{\infty}, p$ . However, regions of only fair agreement occur at transonic speeds. This agreement corroborates the hypothesis that  $q_{\infty}, p$  values become inaccurate near the end of the flight. However, the calculation of  $q_{\infty}$  and, therefore, the flight-derived coefficient data based on  $q_{\infty}$ , was good in the lower altitude region of the flight because the model atmosphere selected was based on a comparison of rawinsonde data measurements (available to 105 000 feet) with the model atmospheres of reference 4. Figure 7(a) shows that  $t = 30\ 545$  seconds at 105 000 feet, and figure 8(b) shows that  $M_{\infty} = 3.5$  at this time; thus defining the trajectory conditions below which relatively good values of the flight-derived aerodynamic coefficients based on  $q_{\infty}$  would be expected.

The hybrid  $C_D$  shows excellent agreement with the flight-derived  $C_D$  based on  $q_\infty, p$  (about 2.5-percent maximum difference) down to  $M_\infty = 4.0$ . From this point, the hybrid data closely follow the flight-derived data based on  $q_\infty$  to the end of the flight. Because these hybrid data are not subject to the same variations in dynamic pressure that the two sets of flight-derived coefficient data are subjected to, the hybrid data can again be used to assess the flight-derived-data sets. Comparisons of the sets of  $C_D$  data show that the flight-derived  $C_D$  based on  $q_\infty, p$  is accurate down to  $M_\infty \approx 4.0$ , where the flight-derived  $C_D$  based on  $q_\infty$  becomes the better set. Furthermore, the good agreement between the hybrid data and the flight-derived  $C_D$  based on  $q_\infty, p$  for  $M_\infty > 4.0$  suggests that the hybrid  $C_D$  data could be used with flight-measured accelerations to obtain a fairly accurate density time history in the higher altitude region.

The  $C_D$  data comparisons in the transonic region do not show any large differences (neglecting the flight-derived data based on  $q_\infty, p$ ), although the flight-derived  $\alpha_R$  showed deviations up to approximately  $10^\circ$  in the transonic region (fig. 14(d)). The modified trim-wind-tunnel  $C_D$  at transonic Mach numbers and in the range  $150^\circ < \alpha_R < 160^\circ$  is relatively insensitive to  $\alpha_R$  ( $C_D$  changes by approximately 0.05 for a  $10^\circ$  change in  $\alpha_R$ ); therefore, the  $C_D$  level would be expected to be approximately the same for all data sets.

The resultant lift-coefficient  $C_{L,R}$  data sets in figure 18(d) show approximately the same comparison as the  $C_D$  data sets show. The comparison of the modified trim-wind-tunnel data with the flight-derived data based on  $q_\infty, p$  shows  $C_{L,R}$  to be slightly higher (4 percent) at the high-hypersonic Mach numbers, because the modified trim-wind-tunnel  $\alpha_R$  is lower at this time. Rather than crossing, as did the  $C_D$  data, the two sets of  $C_{L,R}$  data merge and remain close down to  $M_\infty \approx 4.0$ . At this time, the modified trim-wind-tunnel data again became higher than the flight-derived data based on  $q_\infty, p$  which, again, indicates that the flight-derived coefficient data based on  $q_\infty, p$  are poor in this region.

The flight-derived  $C_{L,R}$  based on  $q_\infty$  showed a large discrepancy in the trajectory skip region, as did the  $C_D$  data, because the value of  $q_\infty$  is higher than  $q_\infty, p$  in the trajectory skip region (fig. 8(a)). Below  $M_\infty = 4.0$ , the flight-derived data based on  $q_\infty$  again appear to be better than the flight-derived data based on  $q_\infty, p$ . Comparison of the hybrid  $C_{L,R}$  data to both sets of the flight-derived  $C_{L,R}$  data was similar to comparison of the hybrid  $C_D$  data to both sets of flight-derived  $C_D$  data. Comparison of the modified trim-wind-tunnel data with the three  $C_{L,R}$

data sets in the transonic region of flight show  $C_{L,R}$  differences up to 50 percent where there were small  $C_D$  differences. These  $C_{L,R}$  differences are the result of the more consistent variation of the modified trim-wind-tunnel data among the transonic Mach numbers and the steeper slopes of  $C_{L,R}$  with respect to the modified trim-wind-tunnel  $\alpha_R$ .

In a previous section of this report, comparisons of the  $(L/D)_R$  data showed several Mach-number regions of fair to poor agreement between the modified trim-wind-tunnel data and the flight-derived data. This discrepancy could have been caused by the use of inaccurate modified trim-wind-tunnel values for either aerodynamic forces or trim attitudes (aerodynamic moments), or both. The  $C_D$  data comparisons of hybrid to flight-derived data based on  $q_\infty, p$  show excellent agreement down to  $M_\infty = 4.0$ , indicating poor determination of the CM trim attitude from the modified trim-wind-tunnel data (i.e., poor moment data). These comparisons did little toward clarifying the data discrepancy in the transonic region. The aerodynamic drag coefficient  $C_D$  is not sensitive to  $\alpha_R$  variations near trim at transonic and subsonic speeds. However, the data comparisons of hybrid  $C_{L,R}$  to flight-derived  $C_{L,R}$  based on  $q_\infty$  show improved agreement over the data comparisons of modified trim-wind-tunnel  $C_{L,R}$  to flight-derived  $C_{L,R}$  in the transonic region. These comparisons indicate poor definition of the dynamic trim attitude in the transonic region. At the lowest Mach numbers, both hybrid and modified trim-wind-tunnel  $C_{L,R}$  data show poor agreement with flight-derived  $C_{L,R}$  data; however, this disagreement is explained by the flight-derived data accuracy at this point in the flight.

#### Aerodynamic Body-Axis Force-Coefficient Data

Time histories of the three basic body-axis force coefficients  $C_A$ ,  $C_Y$ , and  $C_N$  and the resultant, or total, normal-force coefficient  $C_{N,R}$  are presented in figure 19.

A comparison of the axial-force-coefficient  $C_A$  data sets shown in figure 19(a) is similar to the comparison of the  $C_D$  data sets discussed in a previous section of this report. The primary difference is a higher overall magnitude. A detailed examination showed the percent differences to be nearly identical; therefore, all comments for the  $C_D$  data comparisons apply as well to the  $C_A$  data comparisons.

The  $C_{N,R}$  data comparisons in figure 19(b) differ from the other force-coefficient comparisons in that  $C_{N,R}$  is of such a small magnitude that small errors can result in large percent differences. For example, the best flight-derived data (near maximum  $q_\infty, p$ ) could show percent differences up to 40 percent. This fact considered, the same general trend is shown by the sets of data with excellent (within

25 percent) to good (within 50 percent) agreement down to  $M_{\infty} = 1.35$ . Comparison below this point is difficult because of the flight-derived-data accuracy and because of the influence of other previously discussed factors in the transonic region.

The side-force coefficient  $C_Y$  and the normal-force coefficient  $C_N$  are shown in figures 19(c) and 19(d), respectively. Neither hybrid nor modified trim-wind-tunnel data are shown on these figures; however, the flight-derived  $C_N$  time histories are generally similar to the flight-derived  $C_{N,R}$  time histories. The flight-derived  $C_Y$  time histories reflect the sign and magnitude that would be expected from the sign and magnitude of the flight-derived angle of slideslip  $\beta$  (fig. 14(b)).

## CONCLUSIONS

The flight-derived aerodynamic characteristics of the Apollo 4 entry configuration (Command Module 017) have been calculated from onboard-recorded inertial-platform accelerations and attitudes and from reconstructed trajectory data. The results have been compared with modified trim-wind-tunnel data and with hybrid data (modified wind-tunnel data adjusted to flight-derived angle of attack). Examination of these comparisons resulted in the following conclusions.

1. At the initial-entry point, the flight-derived, steady-state resultant trim angle of attack was approximately  $154.5^\circ$ , and the average resultant lift-to-drag ratio was approximately 0.368 (modified trim-wind-tunnel data showing values  $1.5^\circ$  lower and 10 percent higher, respectively). The trend in the hypersonic region was essentially linear with respect to Mach number, reaching a flight-derived trim resultant angle of attack of approximately  $153^\circ$  and a flight-derived trim resultant lift-to-drag ratio of approximately 0.410 at a Mach number of 6.0 (modified trim-wind-tunnel values of  $0.5^\circ$  higher and 3 percent lower, respectively). Good agreement was shown from a Mach number of 4.0 down to a Mach number of 1.35 and below a Mach number of 0.9, with deviations in trim resultant angle of attack up to  $10^\circ$  and in trim resultant lift-to-drag ratio up to 25 percent in the transonic region.

2. When the modified wind-tunnel data were adjusted to the flight-derived angle of attack (hybrid data), these hybrid data agreed with the flight-derived data down to a Mach number of 1.2. This agreement indicates (as data from the previous Apollo space flight (AS-202) indicate) that the modified wind-tunnel force data are reliable even at the initial-entry, high-Mach-number ( $\approx 38$ ), low-Reynolds-number ( $\approx 1.0 \times 10^4$ ) conditions, but that the modified wind-tunnel trim attitudes (moment data) are poor in the initial-entry hypersonic (Mach number greater than 18) region and possibly in the transonic region (Mach number greater than 0.9 and less than 1.20). Differences in the transonic region and below are probably the result of flight-derived data accuracy or of the influence of vehicle dynamics, or of both.

3. The flight-derived aerodynamic force-coefficient data based on the flight-measured stagnation pressure appear to be reliable down to a Mach number of 4.0. Below this point, the poor agreement with the hybrid data is attributed to poor

flight-measured pressure data. In the region below a Mach number of 4.0, the flight-derived coefficients, based on a standard-atmosphere model, are considered slightly better.

## REFERENCES

1. Morth, Raymond: Reentry Guidance for Apollo. MIT/IL Rept. R-532, Jan. 1966.
2. Flight Analysis Section: Reentry Postflight Trajectory Reconstruction and Guidance Evaluation for AS-501 (CSM-017). Document 05952-H477-R0-00, TRW Systems, Mar. 1968.
3. Flight Analysis Section: Apollo Mission 4/AS-501 Trajectory Reconstruction and Postflight Analysis. Note 68-FMT-615, TRW Systems, Mar. 1968.
4. U. S. Committee on Extension to the Standard Atmosphere (COESA): U.S. Standard Atmosphere Supplements, 1966.
5. Moseley, William C., Jr.; and Martino, Joseph C.: Apollo Wind Tunnel Testing Program — Historical Development of General Configurations. NASA TN D-3748, 1966.
6. Moseley, William C., Jr.; Moore, Robert H., Jr.; and Hughes, Jack E.: Stability Characteristics of the Apollo Command Module. NASA TN D-3890, 1967.
7. Jorgensen, Leland H.; and Graham, Lawrence A.: Predicted and Measured Aerodynamic Characteristics for Two Types of Atmosphere-Entry Vehicles (U). NASA TM X-1103, 1965.
8. Neal, Luther, Jr.: An Exploratory Investigation of a Mach Number of 6.9 into the Use of Aerodynamic Controls for Modulating the Lift-Drag Ratio of an Apollo Type Configuration (U). NASA TM X-816, 1963.
9. Wilkinson, D. B.: Hypersonic Shock Tunnel Tests of the 0.05 Scale Apollo Force Model FS-8 (U). Cornell Aeronautical Laboratory Report AA-1712-W-1, 1962.
10. Hillje, Ernest R.: Entry Flight Aerodynamics from Apollo Mission AS-202. NASA TN D-4185, 1967.
11. Lewis, Clark H.; and Burgess, E. G., III: Altitude-Velocity Table and Charts for Imperfect Air. AEDC-TDR-64-214, Jan. 1965.
12. Ames Research Staff: Equations, Tables, and Charts for Compressible Flow. NACA Rept. 1135, 1953.
13. System Engineering and Test Analysis Section, Apollo 4 Mission Report, Supplement 9: Guidance and Navigation Error Analysis-Final Report. Document 05952-H394-R0-00, TRW Systems, Feb. 1968.
14. Perez, Leopoldo F.: Command Module Entry Aerodynamics Data Accuracy Analysis for Apollo Mission AS-501 (Apollo 4). Document D2-118046-2. Boeing Company, Sept. 1968.

TABLE I. - SIGNIFICANT EVENTS DURING ENTRY

Event or AGC entry control phase	AGC entry control program, number	Time, sec	Remarks
CM/SM separation		29 882.6	
INITIAL ENTRY (initial roll)	63		
Entry interface (400 000 ft)		29 968.54	
0.05g interface	64	<sup>a</sup> 29 999	
First peak g		30 045	
HUNTEST		<sup>a</sup> 30 045	Altitude rate = -679 ft/sec
UPCONTROL	65	<sup>a</sup> 30 085	
KEPLER or BALLISTIC	66		Not required for Apollo 4 mission
FINAL ENTRY	67	<sup>a</sup> 30 253	
Second peak g		30 431	
Guidance termination		<sup>a</sup> 30 601	V < 1000 ft/sec
Drogue parachute deployment		30 678.6	
Main parachute deployment		30 725.8	
Landing		31 029.2	

<sup>a</sup>Apollo guidance computer time.

TABLE II. - ESTIMATED COMMAND-MODULE CENTER OF GRAVITY AND  
MASS CHANGE DURING ENTRY

Mach number	Time, sec	Event	Center of gravity, (a) in.		Mass, slugs	Weight, lb
			X-axis (b)	Z-axis (c)		
25.6	29 968.54	Entry	1039.58	6.57	369.7	11 959
29.2	30 045	First peak g	1039.62	6.56	368.2	11 857
12.6	30 431	Second peak g	1039.70	6.49	364.2	11 731
6.0	30 505		1039.72	6.45	363.8	11 715
4.0	30 538		1039.73	6.42	363.5	11 705
3.0	30 553		1039.74	6.41	363.4	11 702
2.4	30 564		1039.74	6.40	363.2	11 696
2.0	30 572		1039.74	6.39	363.2	11 694
1.65	30 581		1039.75	6.38	363.1	11 692
1.35	30 590		1039.75	6.37	363.0	11 688
1.2	30 596		1039.75	6.37	362.9	11 686
1.1	30 602		1039.76	6.36	362.9	11 684
0.9	30 618		1039.76	6.34	362.5	11 674
0.7	30 637		1039.77	6.32	362.5	11 672
0.42	30 678.6	Drogue deployment	1039.79	6.27	362.1	11 659
0.4	30 680		1039.79	6.27	362.1	11 659

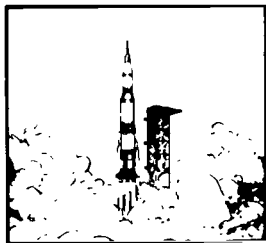
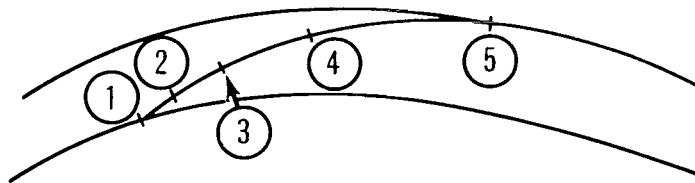
<sup>a</sup>Centers of gravity are in the NASA reference system.

<sup>b</sup>The longitudinal reference (body X-axis) has an origin 1000 inches below the tangency line of the CM substructure mold line.

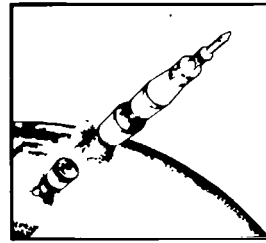
<sup>c</sup>The Z-axis measurement includes the constant Y-axis offset of 0.3 inch.

TABLE III. - FLIGHT-DERIVED DATA INPUT REQUIREMENTS

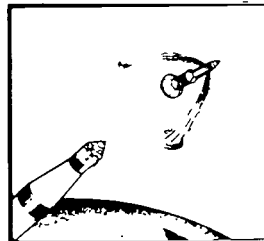
Input	Output													
	$\alpha$	$\beta$	$\alpha_R$	$\phi_A$	$C_A$	$C_Y$	$C_N$	$C_{N,R}$	$C_L$	$C_D$	$C_{L,V}$	$C_{L,H}$	$(L/D)_R$	$(L/D)_V$
<b>BET:</b>														
$V$	X	X	X	X						X	X	X		
$\gamma$	X	X	X	X						X	X	X	X	
$\sigma$	X	X	X	X					X	X	X	X	X	
$\theta_{GD}$	X	X	X	X					X	X	X	X	X	
$\phi_{GD}$	X	X	X	X					X	X	X	X	X	
$q_\infty$					X	X	X	X	X	X	X	X		
g. e. t.	X	X	X	X					X	X	X	X	X	X
<b>IMU:</b>														
$\theta$	X	X	X	X	X	X	X	X						
$\phi$	X	X	X	X	X	X	X	X						
$\psi$	X	X	X	X	X	X	X	X						
$A_{x,p}$					X	X	X	X	X	X	X	X	X	X
$A_{y,p}$					X	X	X	X	X	X	X	X	X	X
$A_{z,p}$					X	X	X	X	X	X	X	X	X	X
<b>Miscellaneous:</b>														
$m$					X	X	X	X	X	X	X	X		
$s$					X	X	X	X	X	X	X	X		
Lift-off time	X	X	X	X					X	X	X	X	X	X
$q_\infty, p$					X	X	X	X	X	X	X			



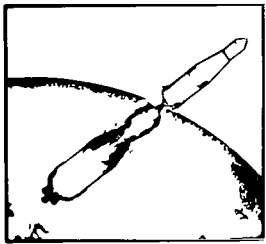
① Lift-off,  
12:00:01 G.m.t.



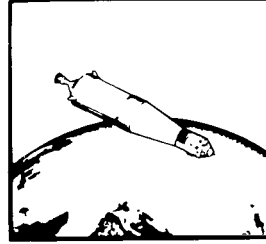
② S-II ignition,  
00:02:32.2 g.e.t.



③ Launch-escape-system jettison,  
00:03:07.2 g.e.t.



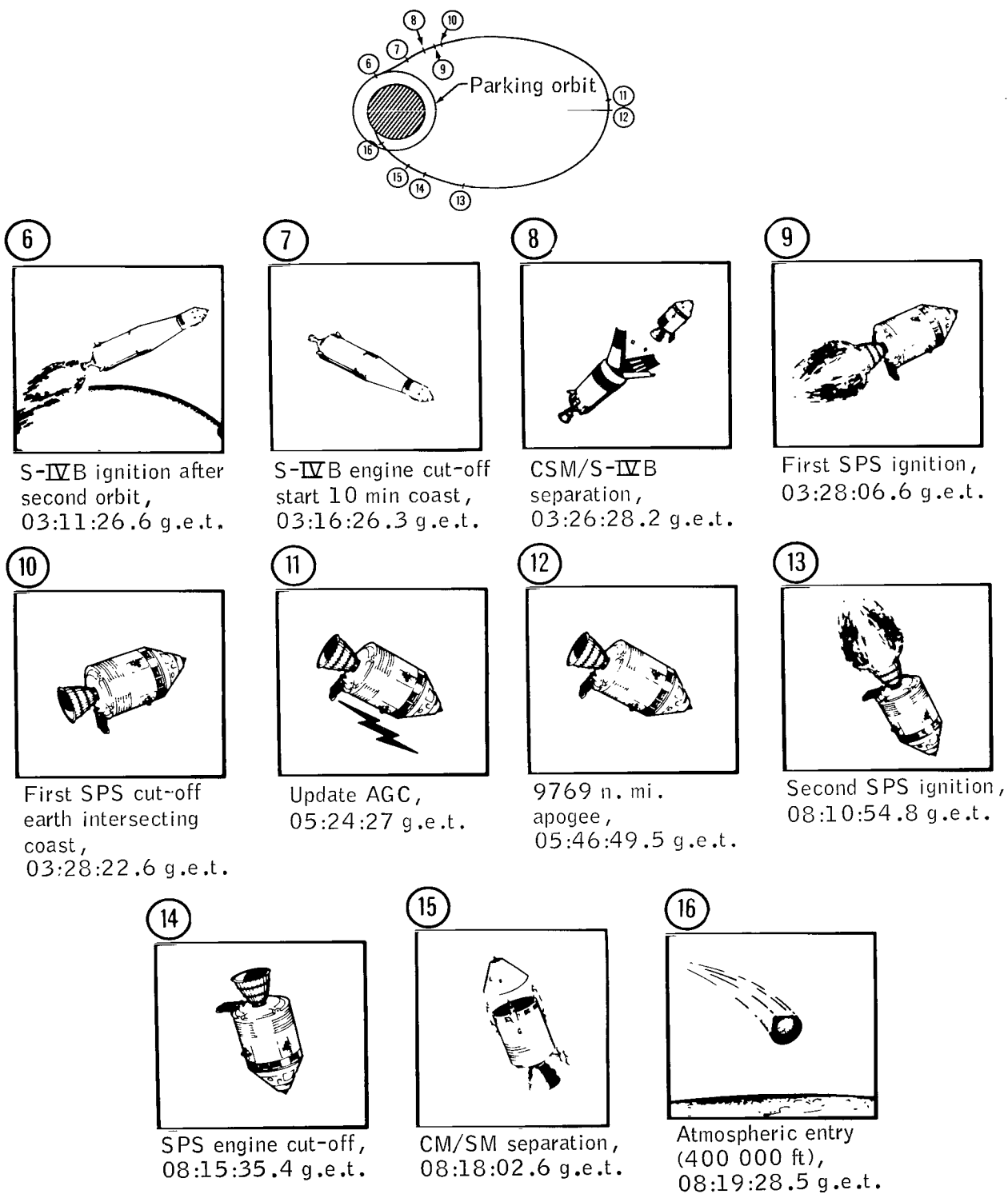
④ S-IVB ignition,  
00:08:40.7 g.e.t.



⑤ S-IVB engine cut-off,  
earth parking orbit,  
00:11:15.6 g.e.t.

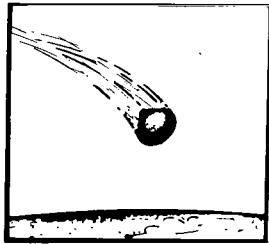
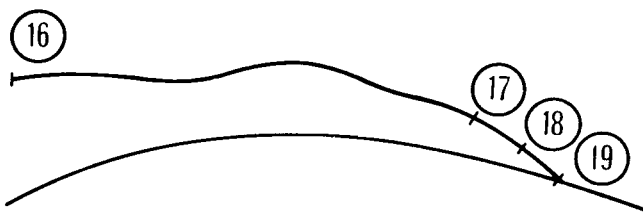
(a) Launch into earth parking orbit.

Figure 1. - Apollo 4 mission profile.

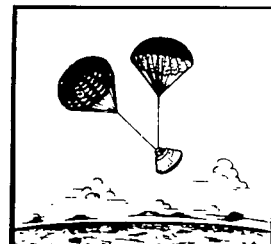


(b) Injection into earth-intersecting coast ellipse.

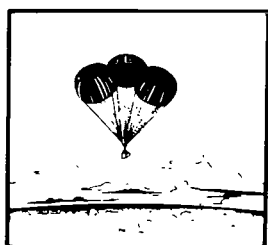
Figure 1. - Continued.



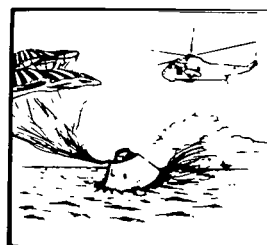
16 Atmospheric entry,  
08:19:28.5 g.e.t.



17 Drogue parachute  
deployment,  
08:31:18.6 g.e.t.



18 Main parachute  
deployment,  
08:32:05.8 g.e.t.



19 CM landing,  
08:37:09.2 g.e.t.

(c) Atmospheric entry.

Figure 1. - Concluded.

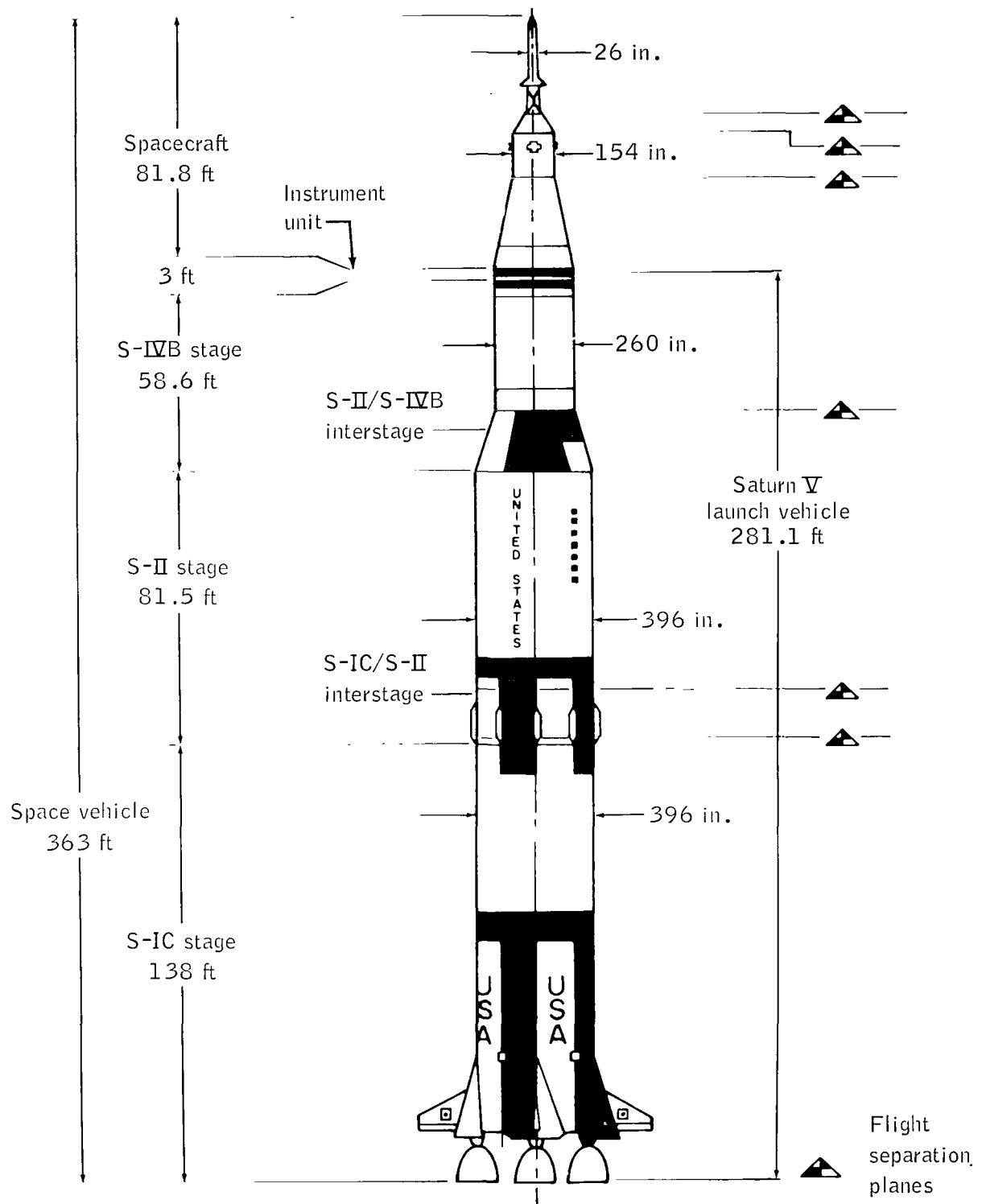


Figure 2. - Apollo 4 launch vehicle configuration.



Figure 3. - Recovery of the CM-017 forward heat shield.

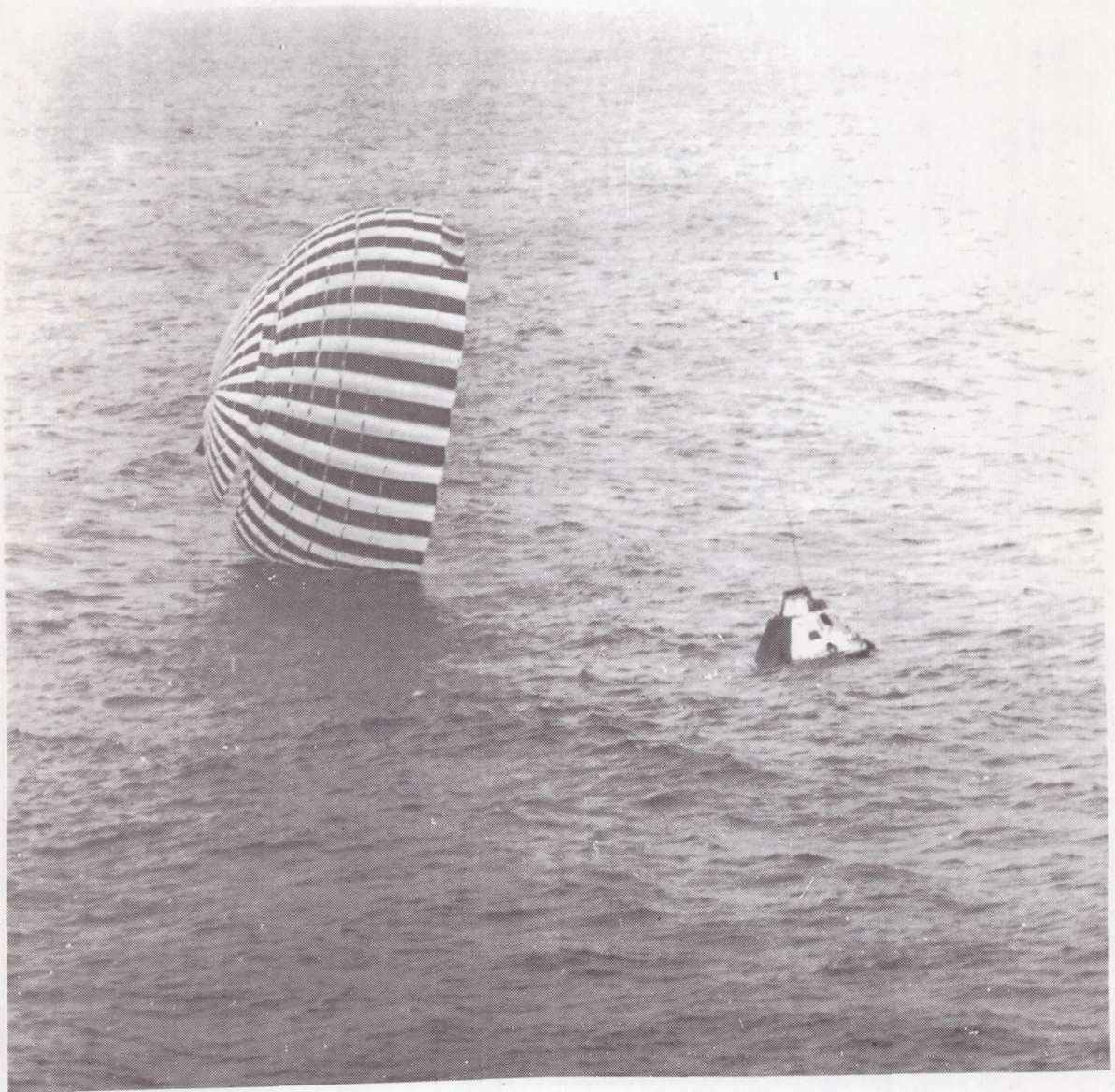


Figure 4. - The CM-017 shortly after landing, showing one main parachute still attached.

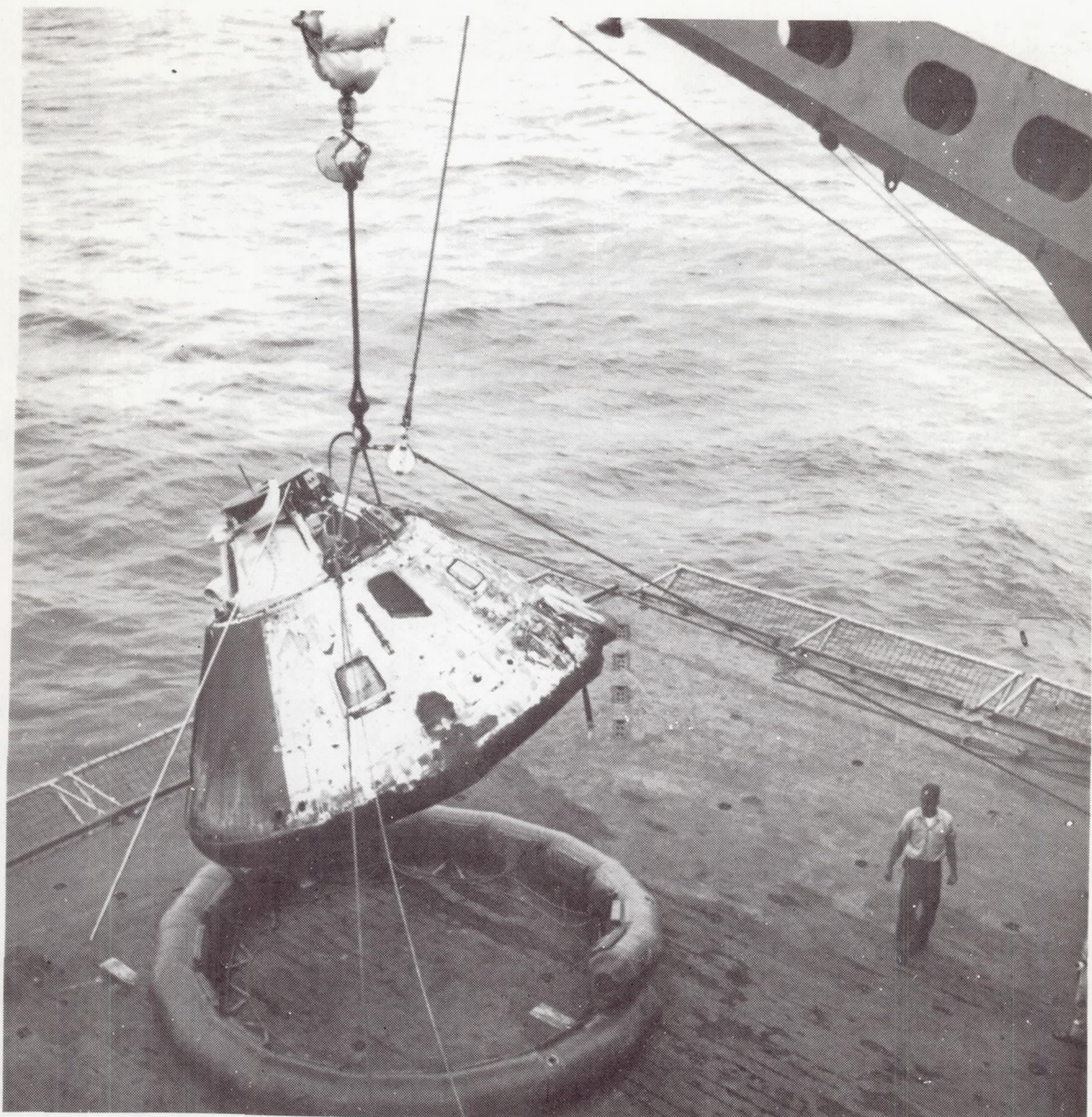
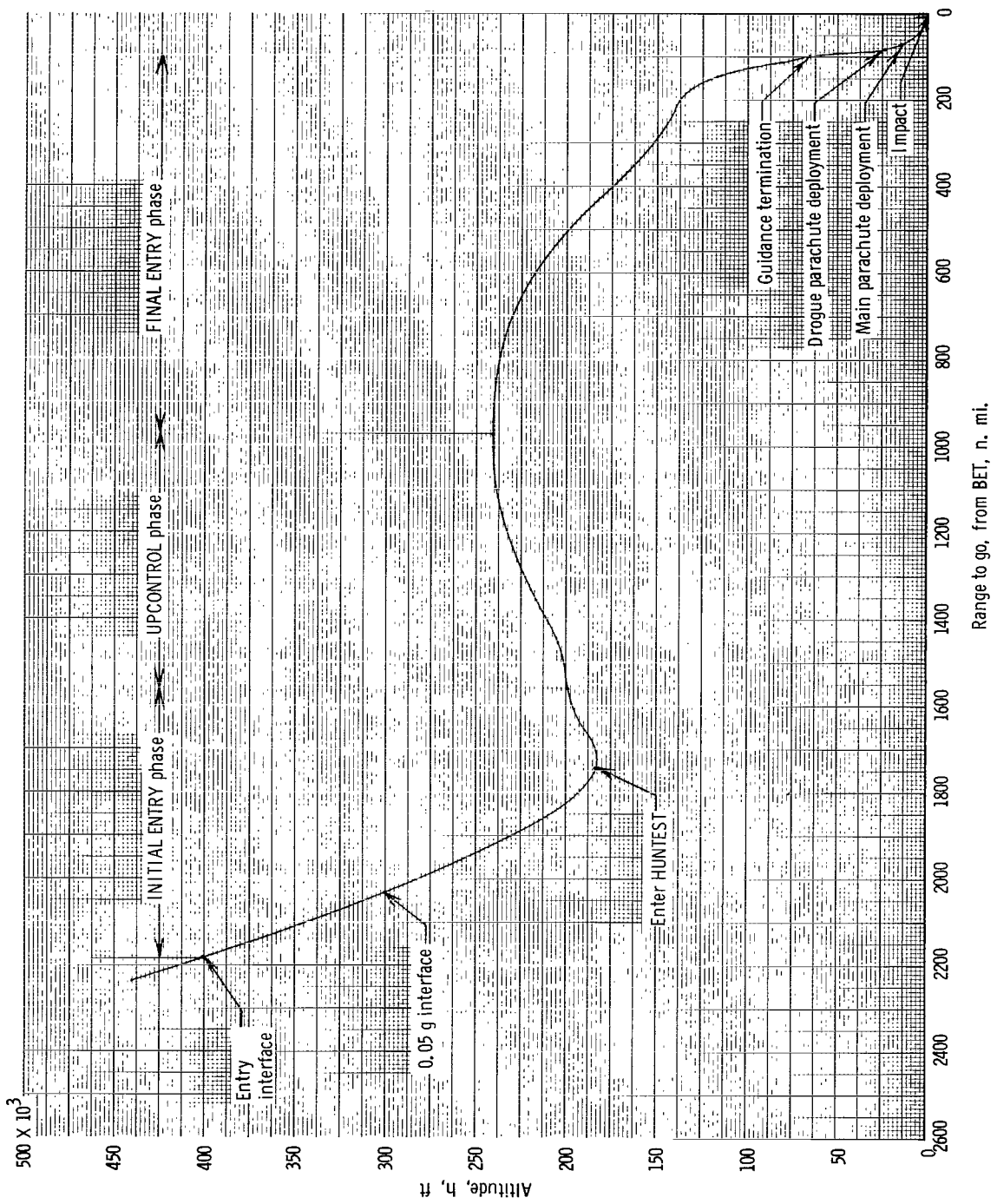
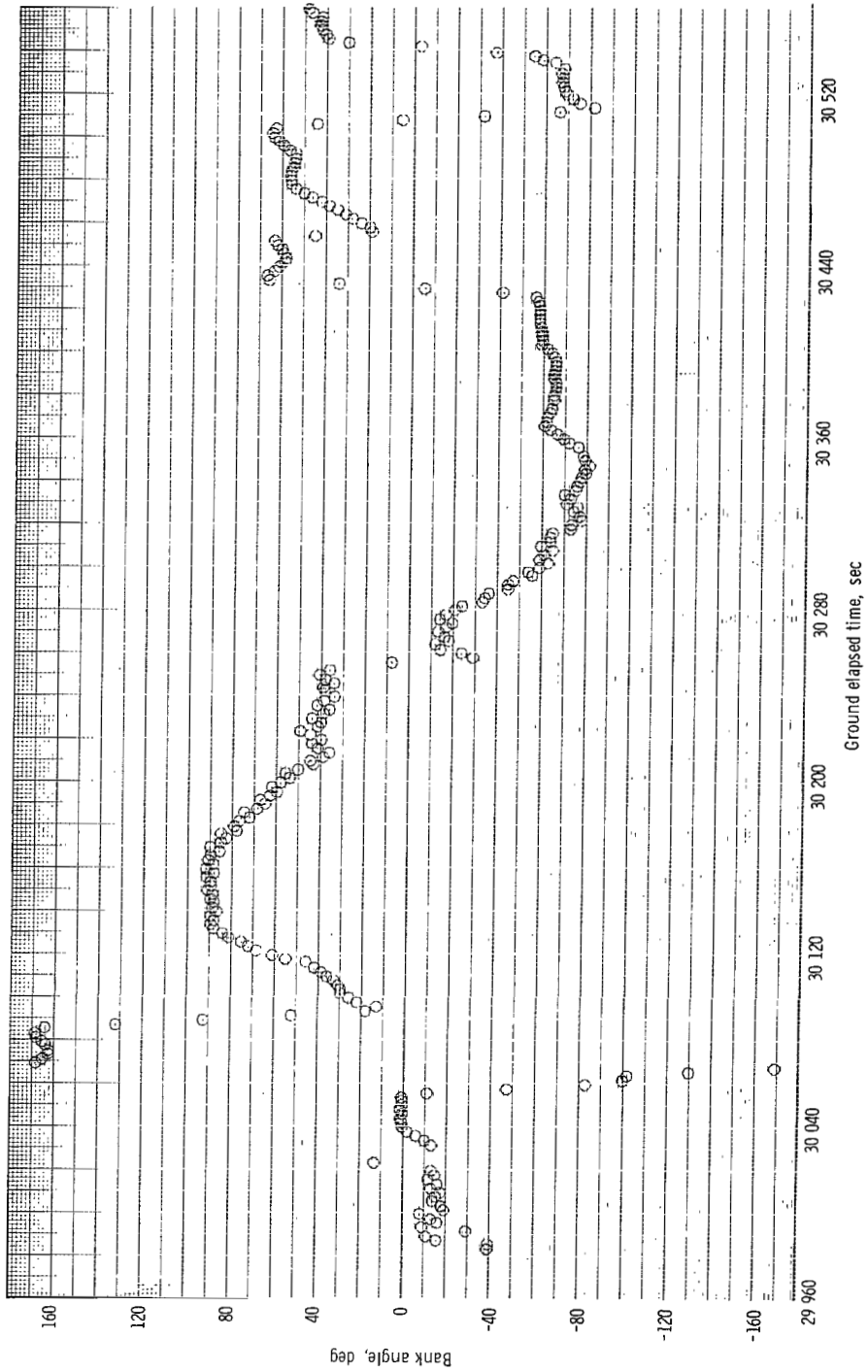


Figure 5. - The CM-017 being hoisted aboard the recovery ship  
U. S. S. Bennington.



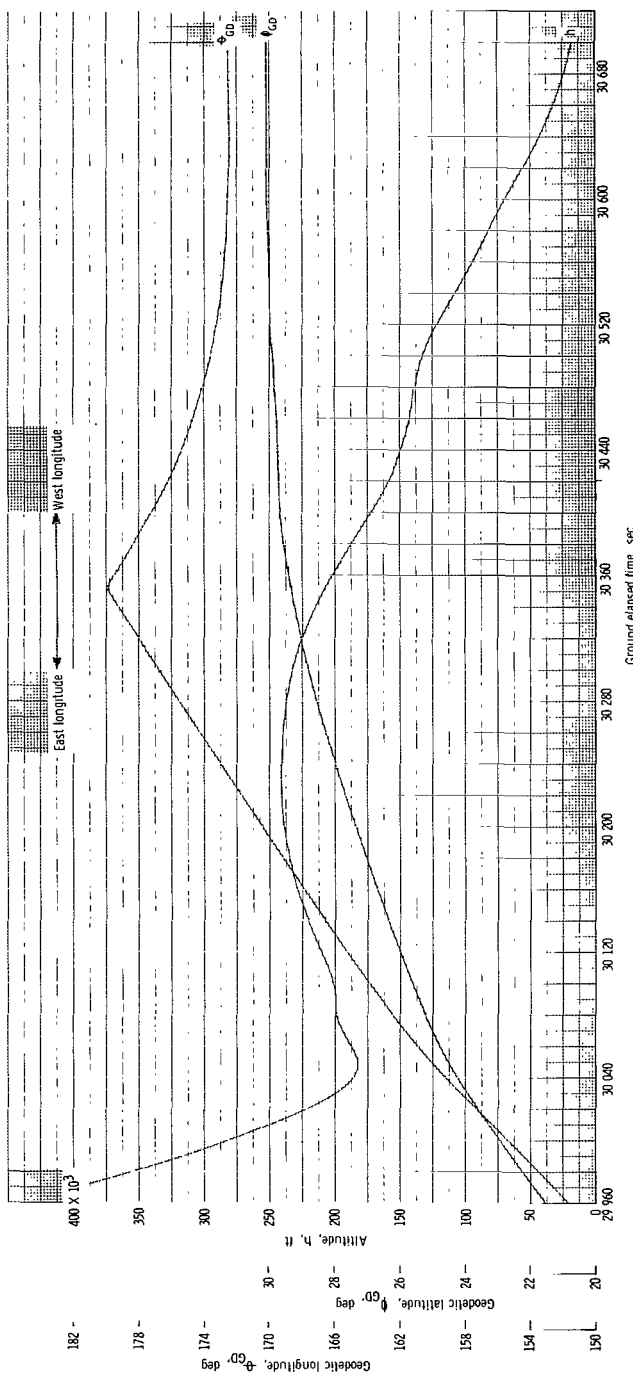
(a) Apollo guidance computer entry control.

Figure 6. - Entry trajectory control programs.



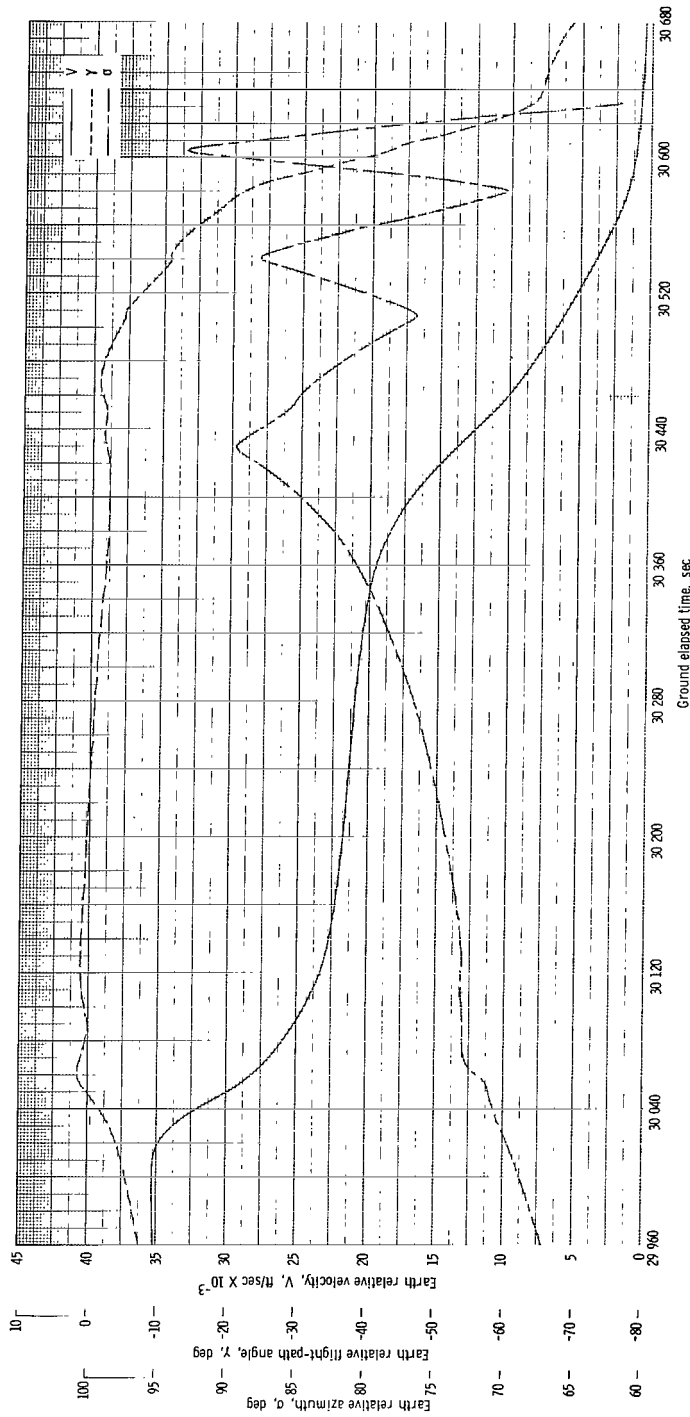
(b) Bank-angle time history.

Figure 6. - Concluded.



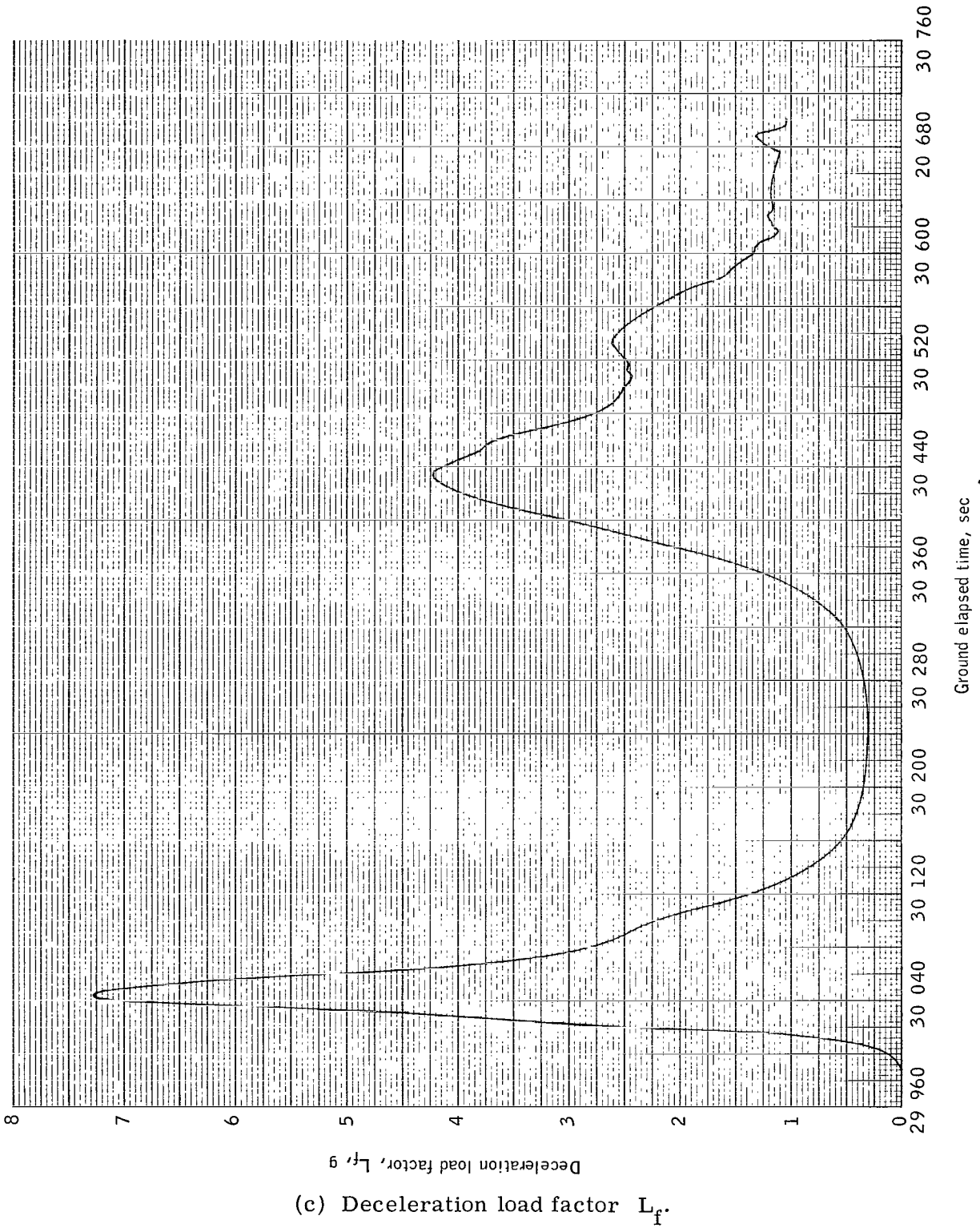
(a) Altitude  $h$ , longitude  $\phi_{GD}$ , and geodetic latitude  $\psi_{GD}$ .

Figure 7. - Time histories of trajectory parameters for atmospheric entry phase.



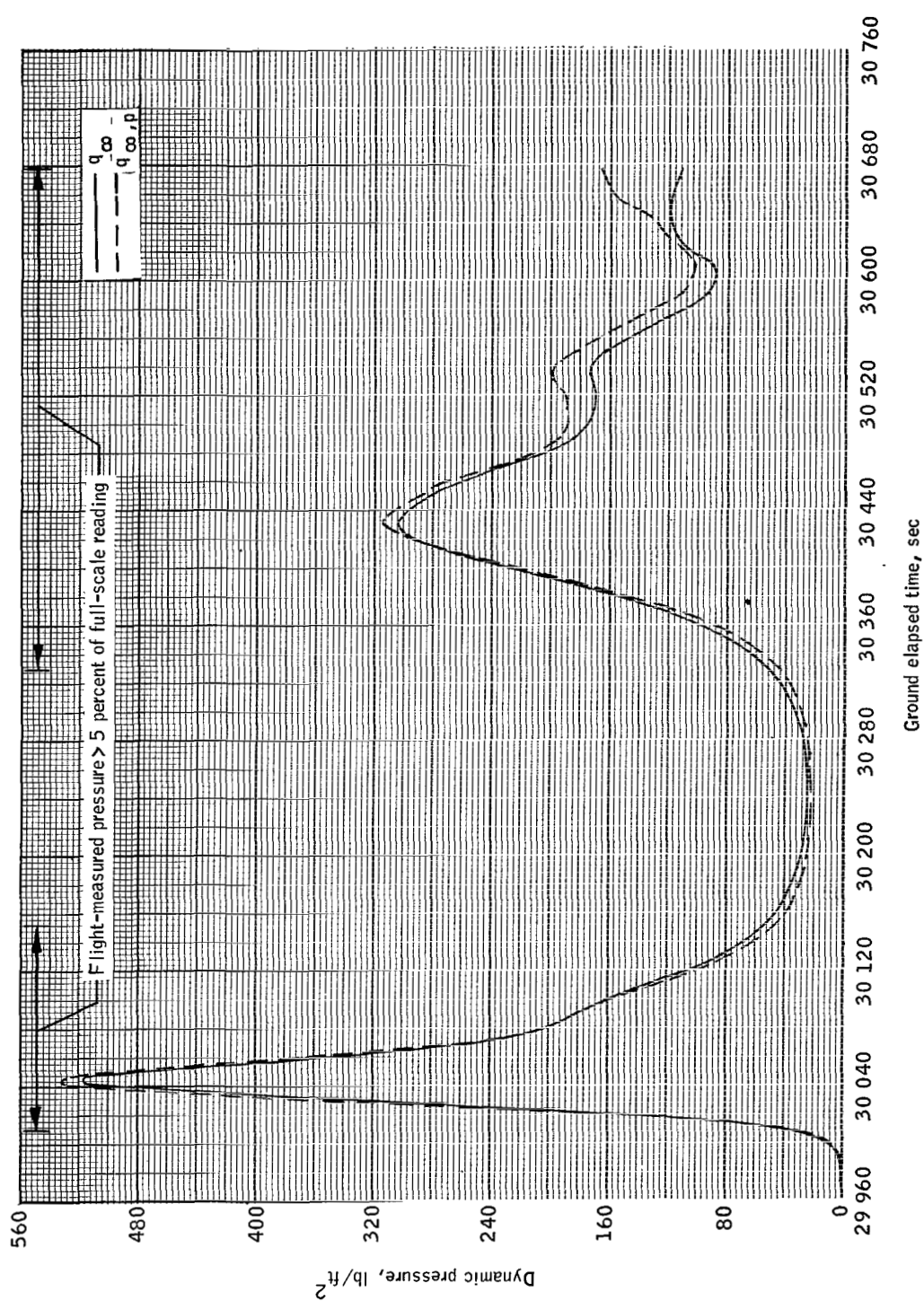
(b) Earth relative velocity  $V$ , flight-path angle  $\gamma$ , and azimuth  $\sigma$ .

Figure 7. - Continued.



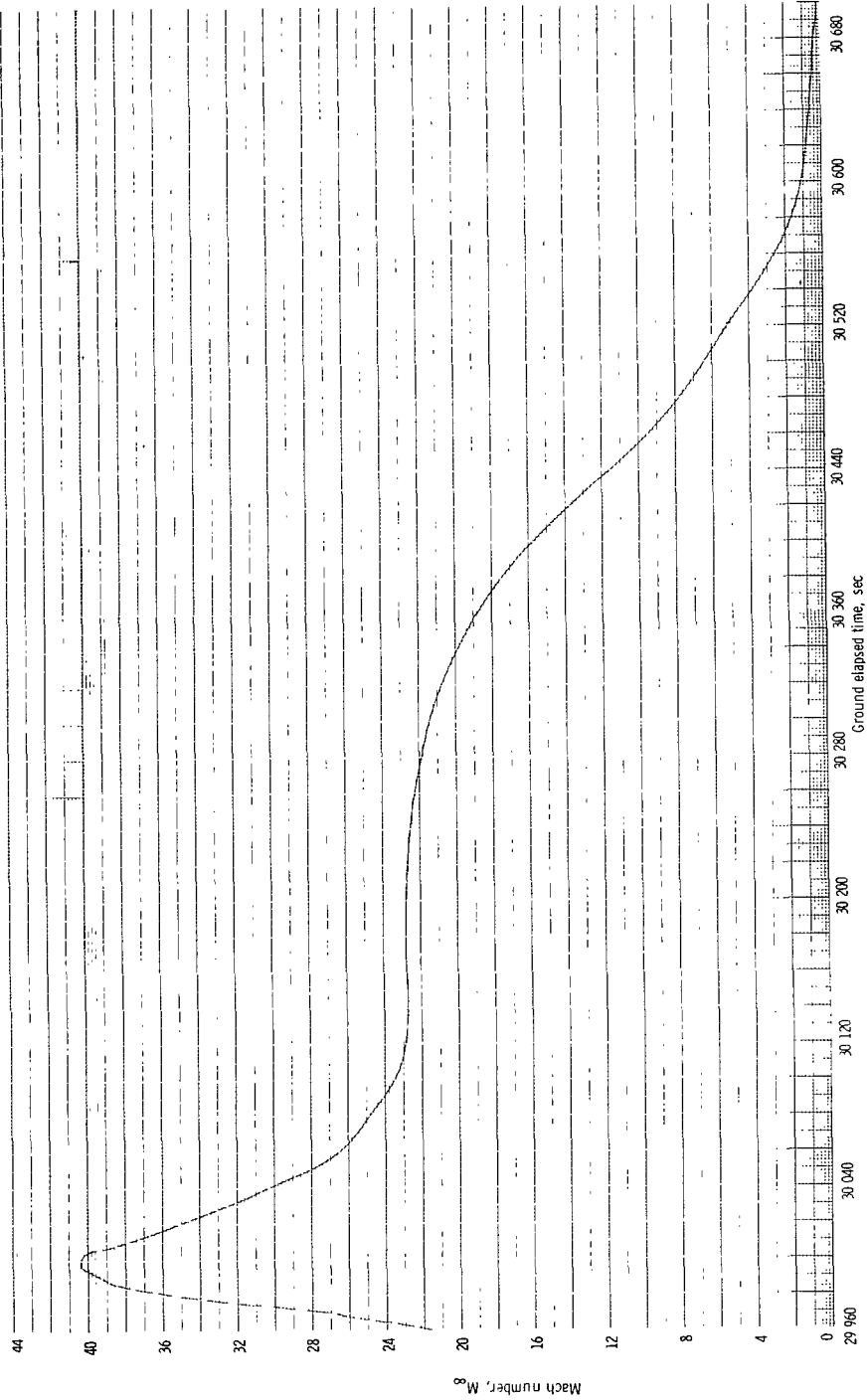
(c) Deceleration load factor  $L_f$ .

Figure 7. - Concluded.



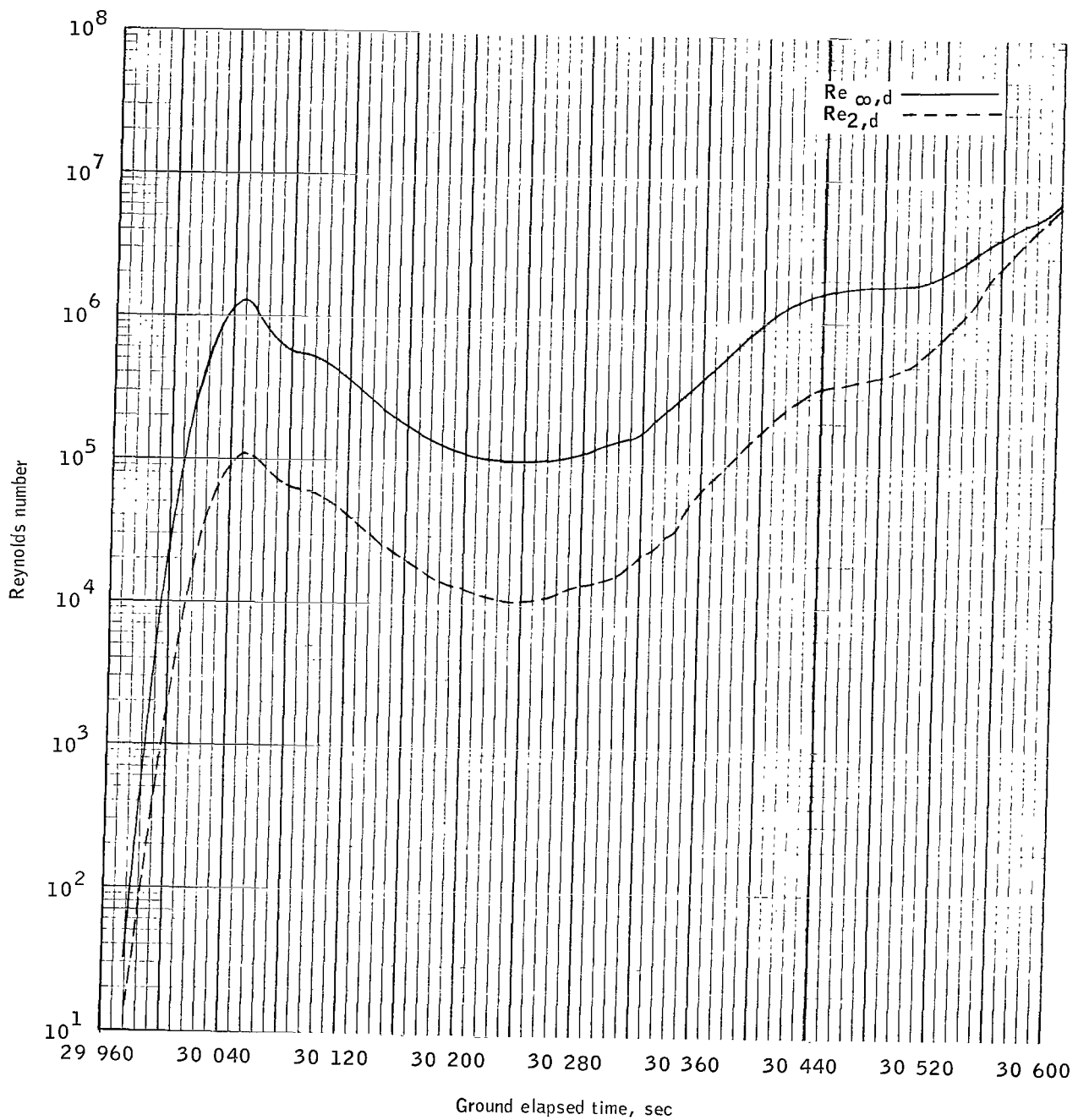
(a) Dynamic pressure.

Figure 8. - Time histories of trajectory/atmosphere data.



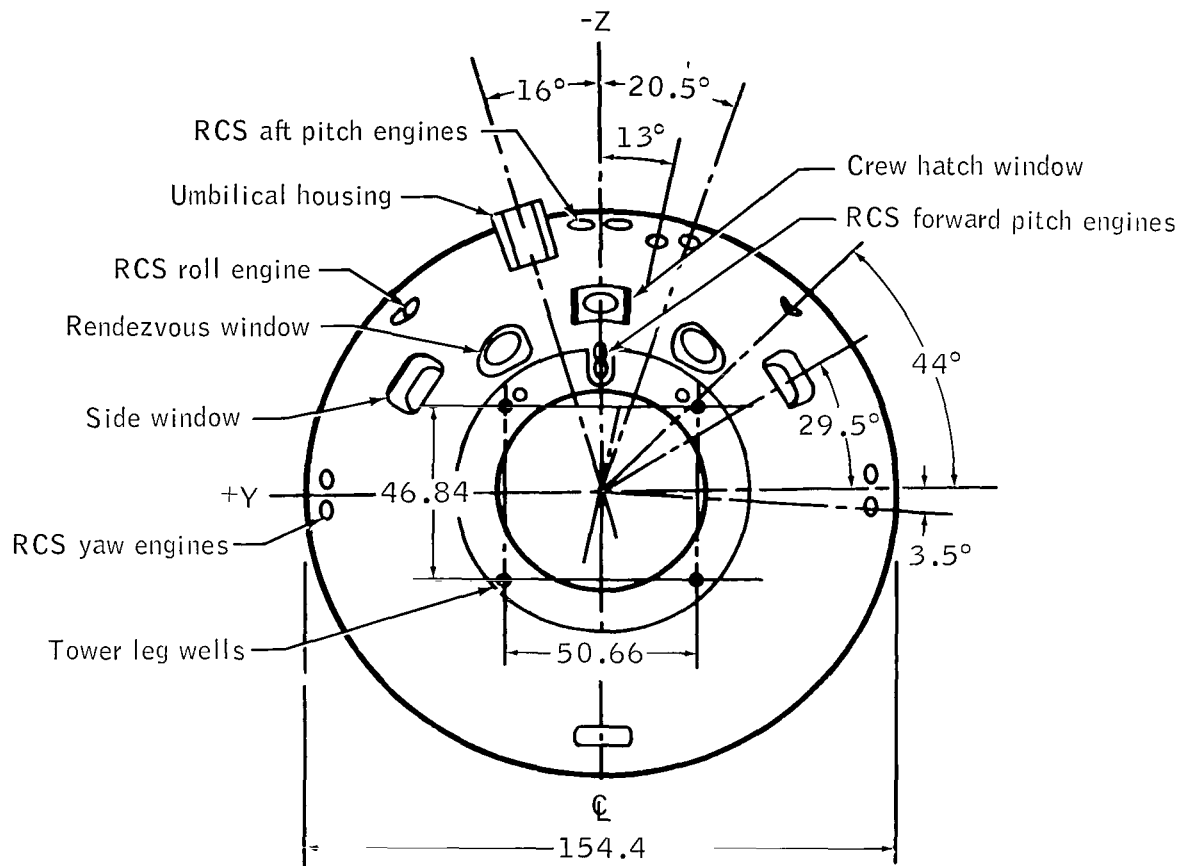
(b) Mach number  $M_{\infty}$

Figure 8. - Continued.



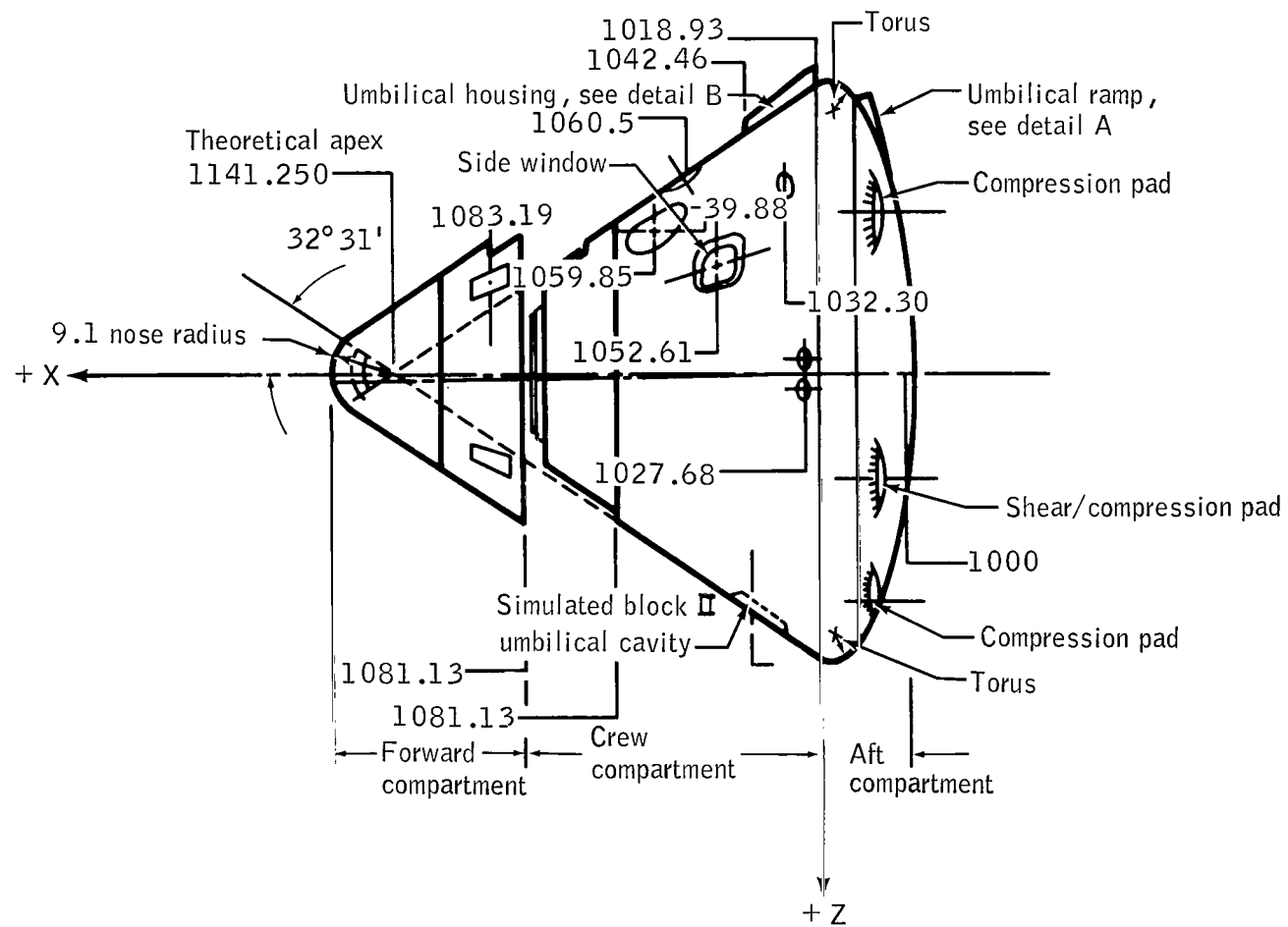
(c) Reynolds number.

Figure 8. - Concluded.



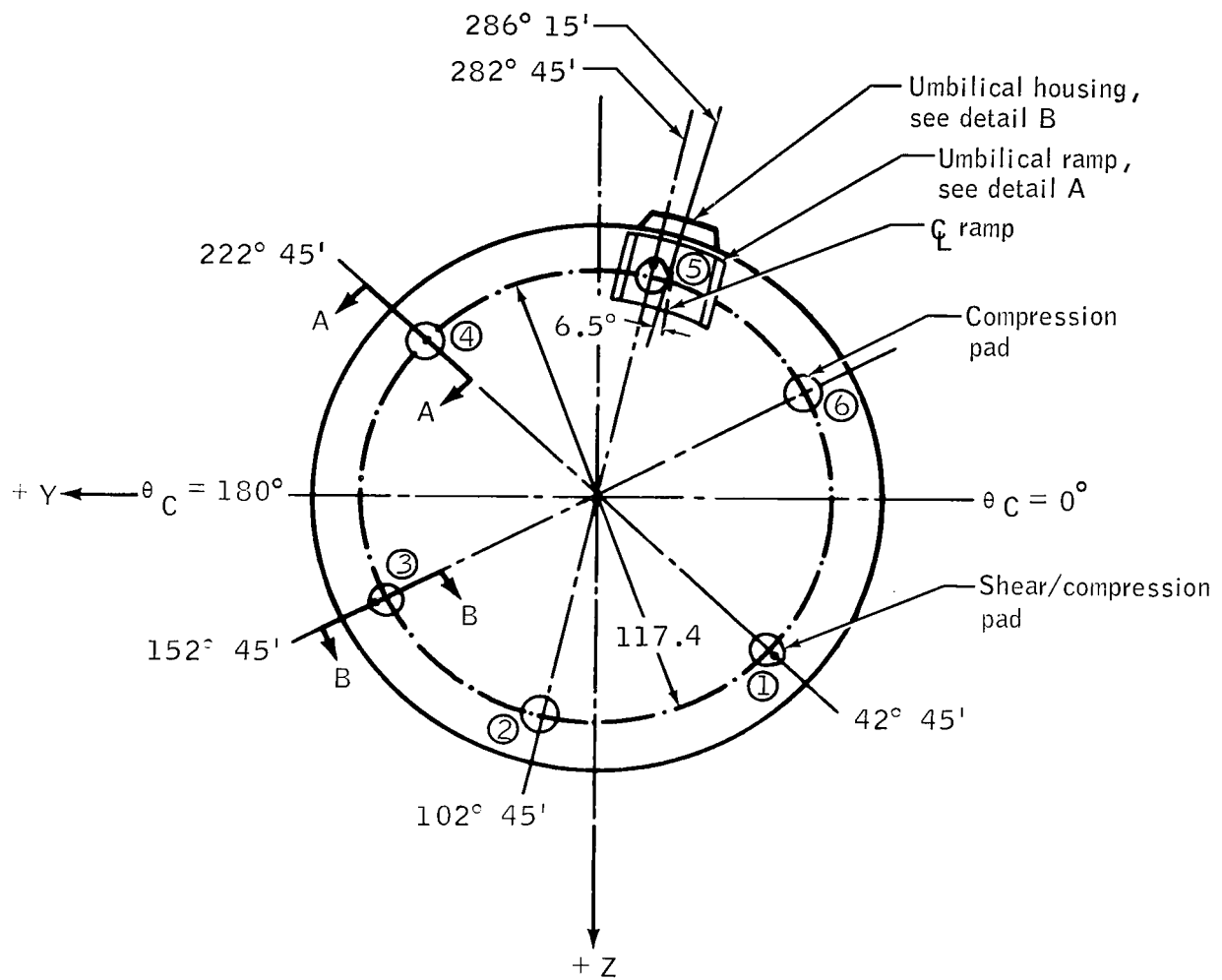
(a) View looking aft.

Figure 9. - Command Module 017 external configuration.  
All linear dimensions are in inches.



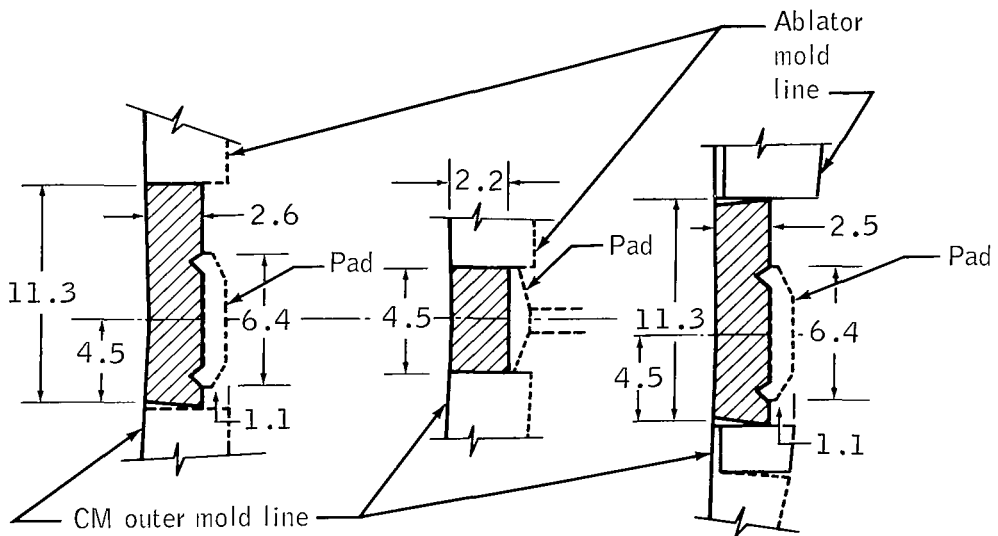
(b) Side view. X-stations are in inches.

Figure 9. - Continued.



(c) View looking forward. Pad numbers are shown in circles.

Figure 9. - Continued.



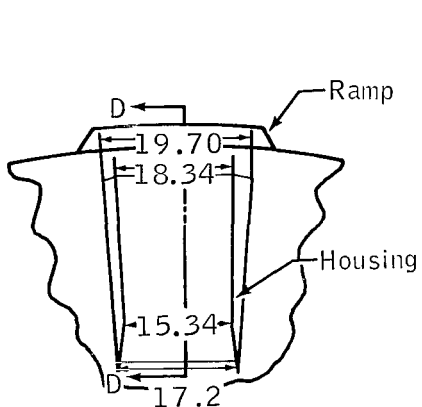
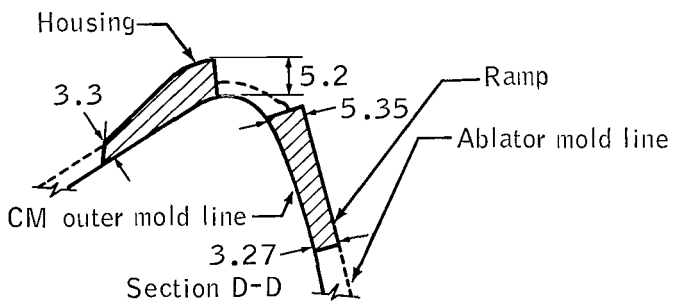
Section A-A,  
typical compression  
pads 2, 4, and 6

Section B-B,  
typical shear/  
compression  
pads 1 and 3

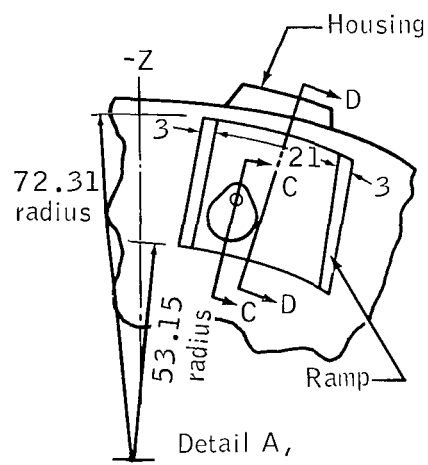
Section C-C,  
shear/compression  
pad 5

(d) Detail of shear/compression pads. Dimensions are only approximate (in inches).

Figure 9.- Continued.



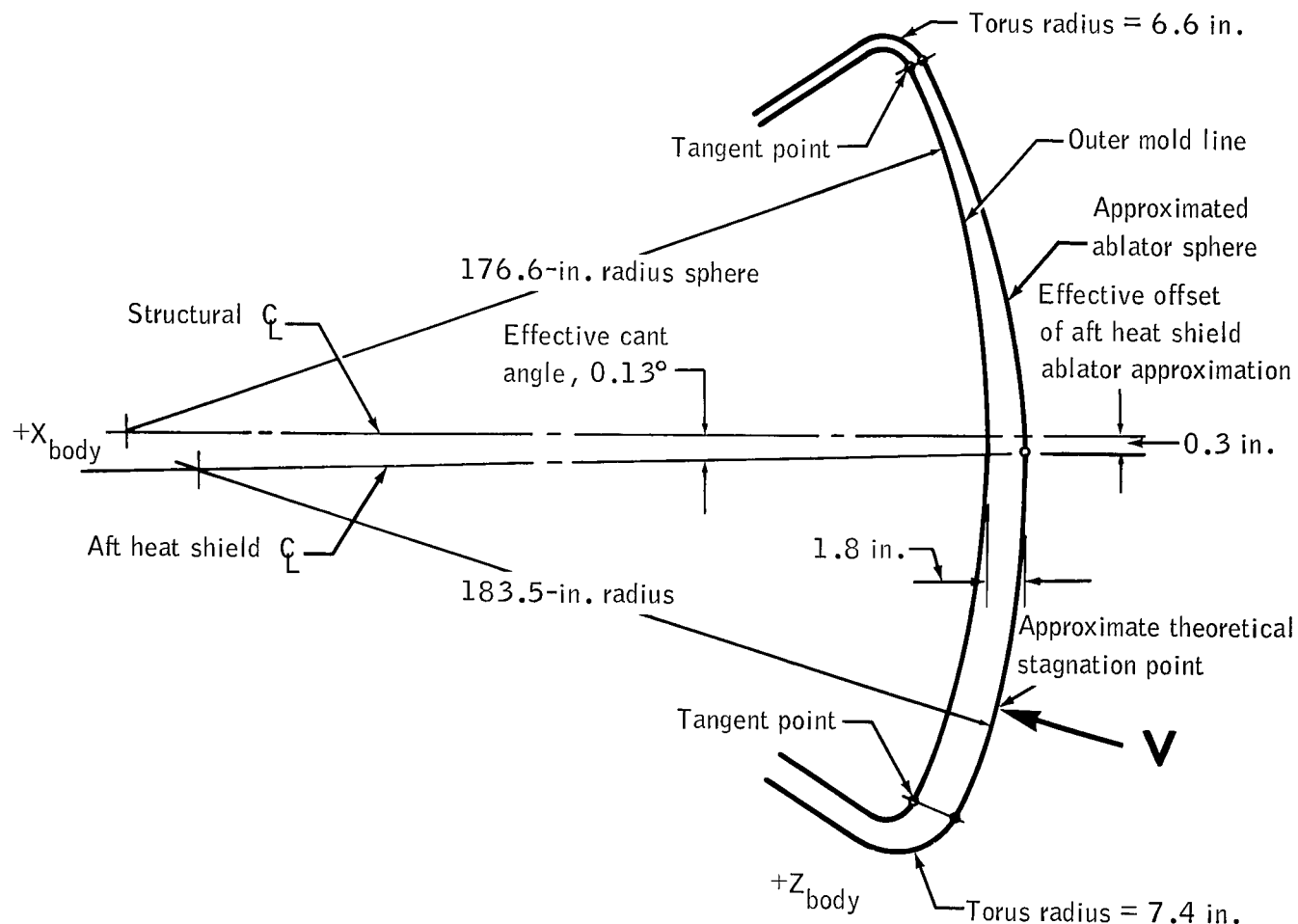
Detail B,  
umbilical housing  
(top view)



Detail A,  
umbilical ramp  
(looking forward)

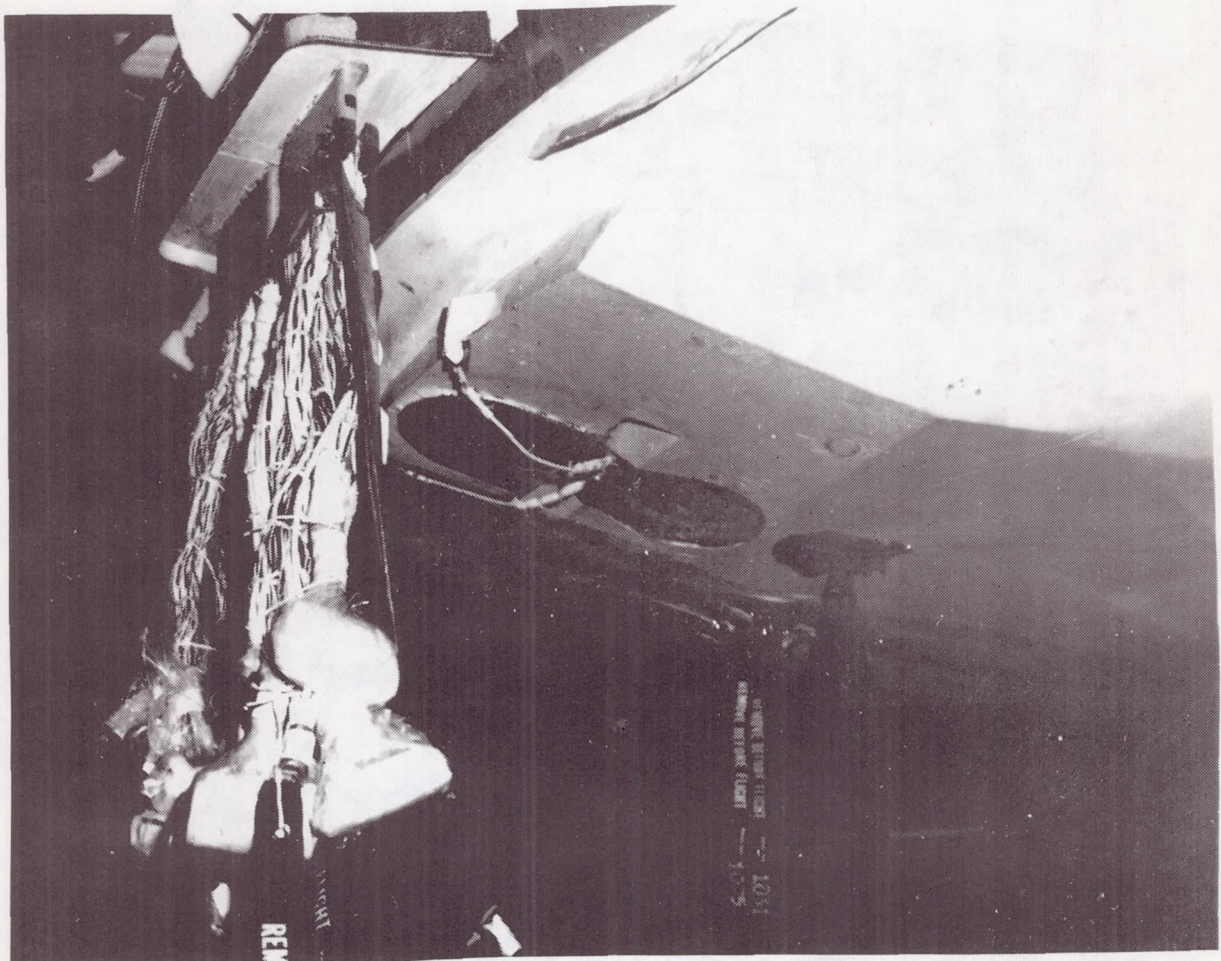
(e) Details of umbilical system.

Figure 9. - Continued.



(f) Exaggerated view of a cross section of the aft heat shield taken in the X-Z plane.

Figure 9. - Continued.



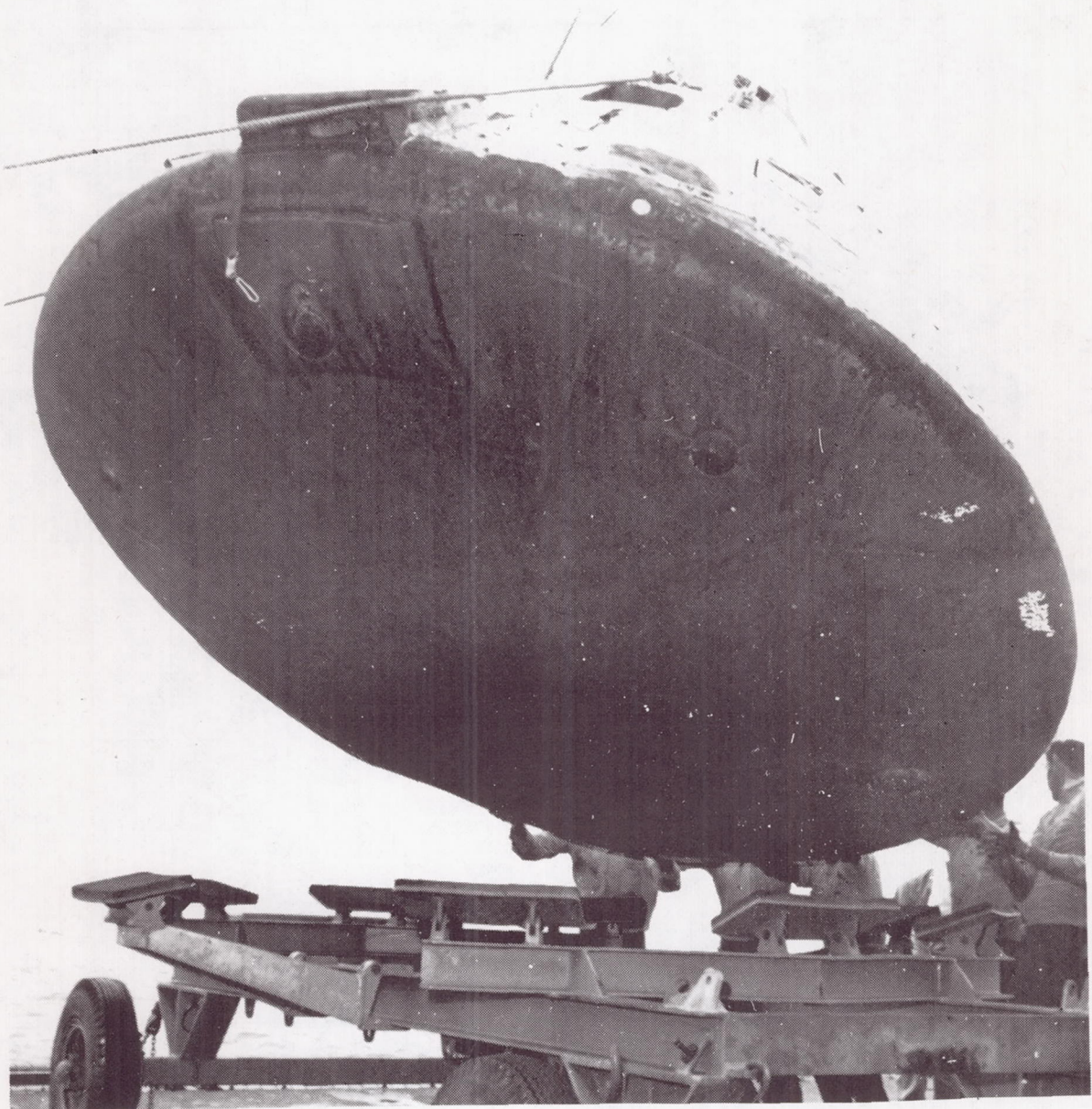
(g) Preflight photograph of CM-017 umbilical housing and ramp.

Figure 9. - Continued.



(h) Postflight photograph of CM-017 umbilical housing and ramp.

Figure 9.- Continued.



(i) Overall photograph of CM-017 on deck of recovery ship.

Figure 9. - Concluded.

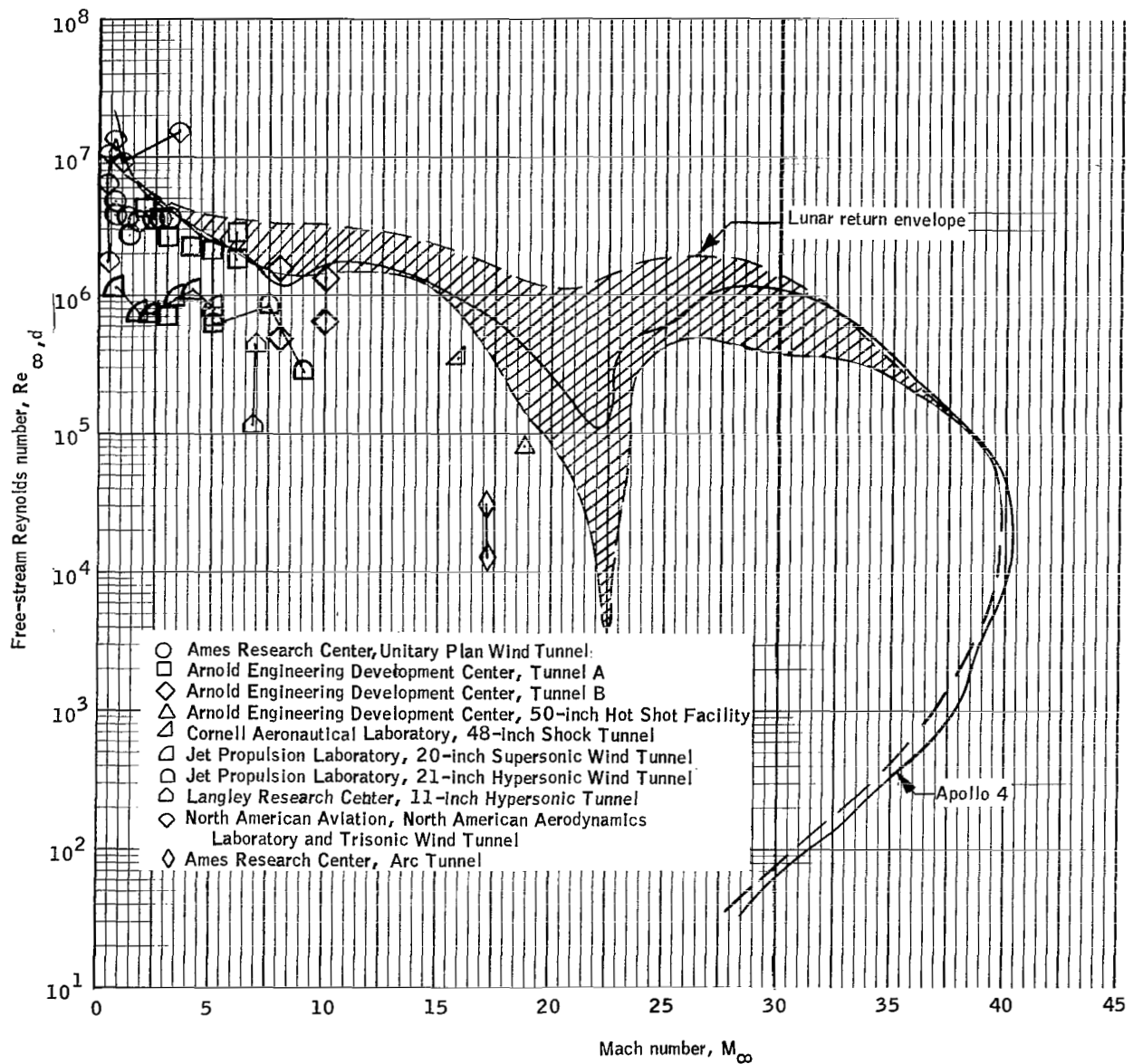


Figure 10. - Comparison of Apollo entry flow conditions with ground-facility capabilities.

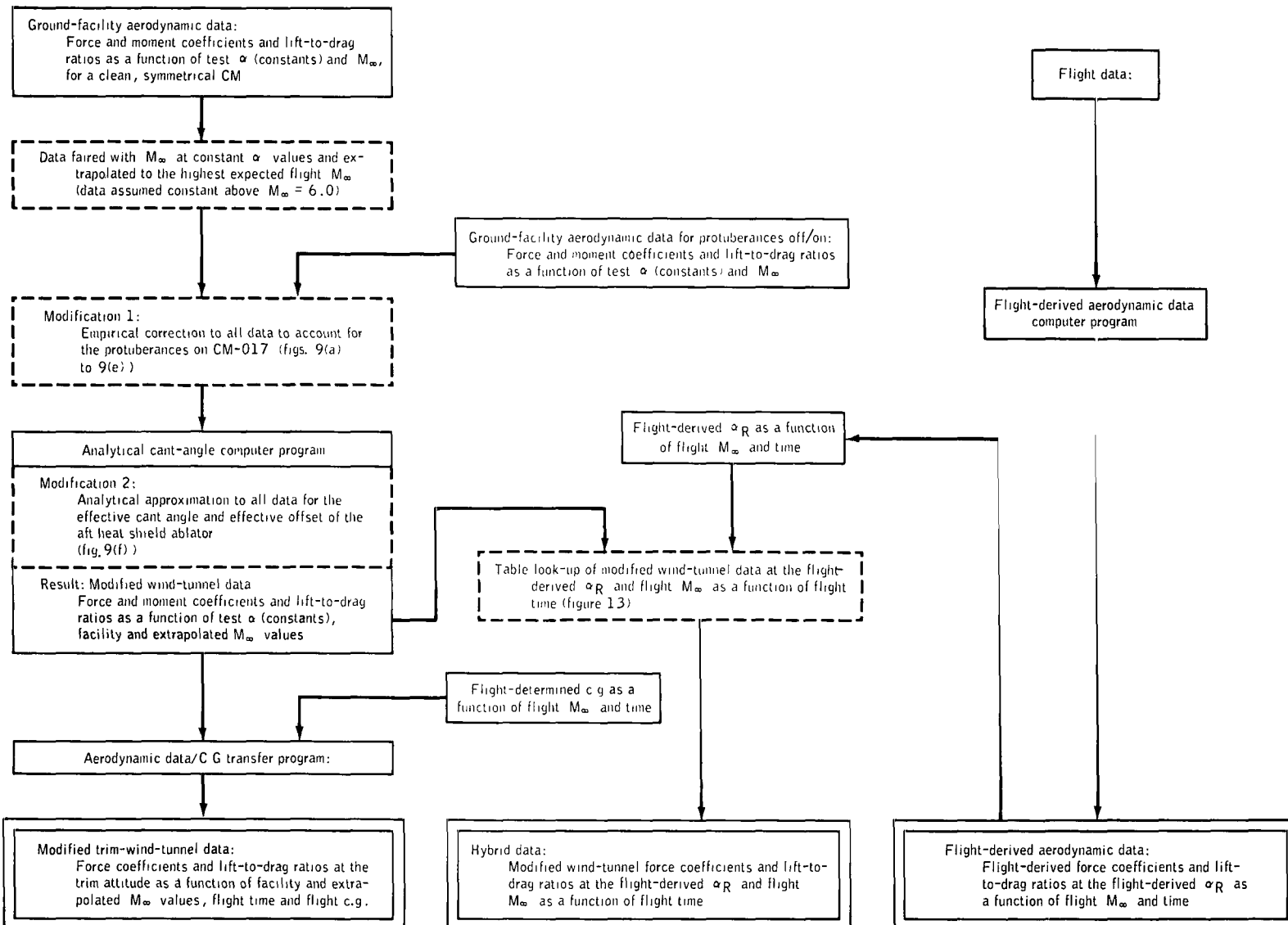


Figure 11. - Formulation of modified trim-wind-tunnel and hybrid aerodynamic data.

||||| ||

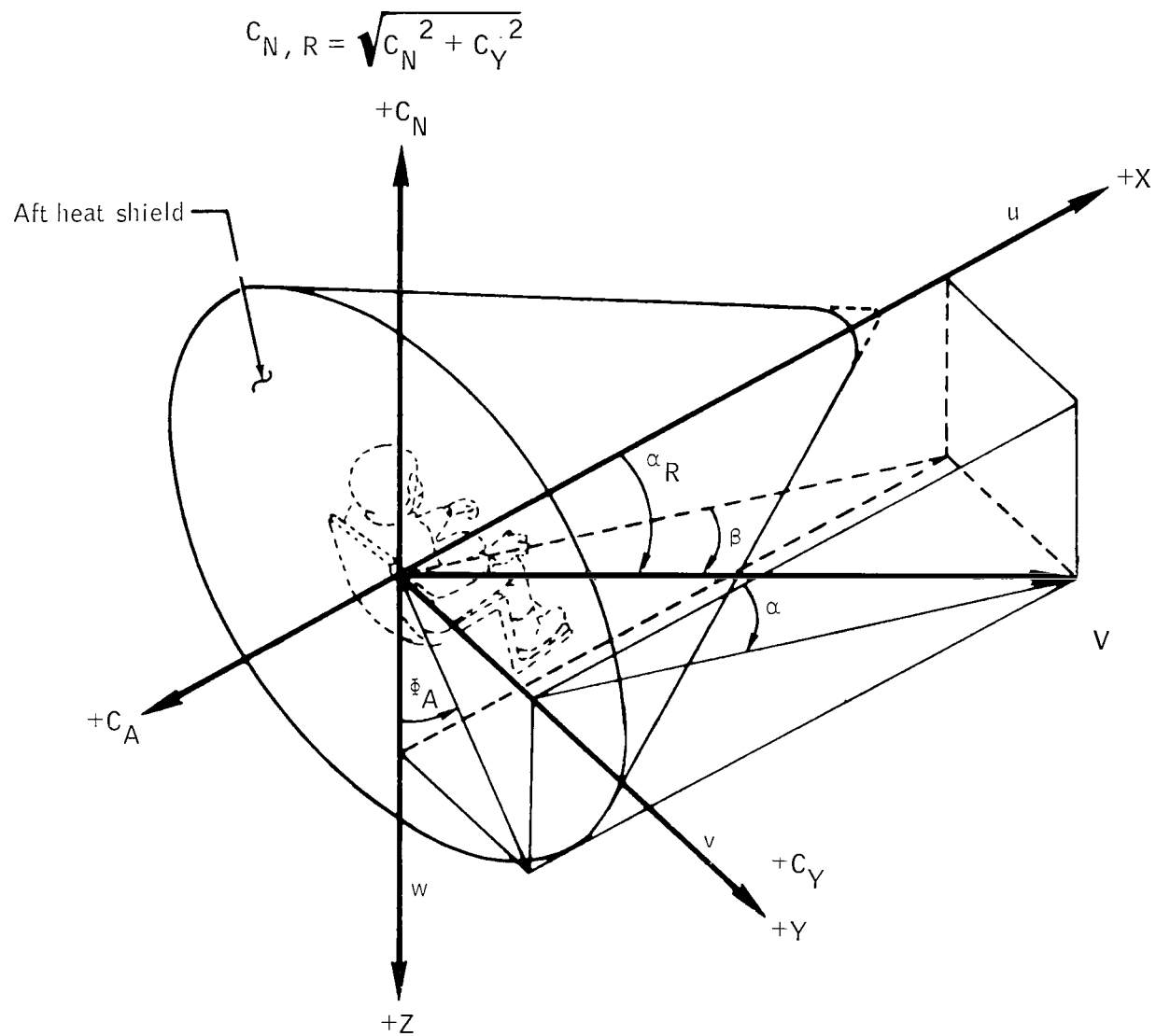


Figure 12. - Body-axis system showing positive directions of aerodynamic angles and aerodynamic body force coefficients.

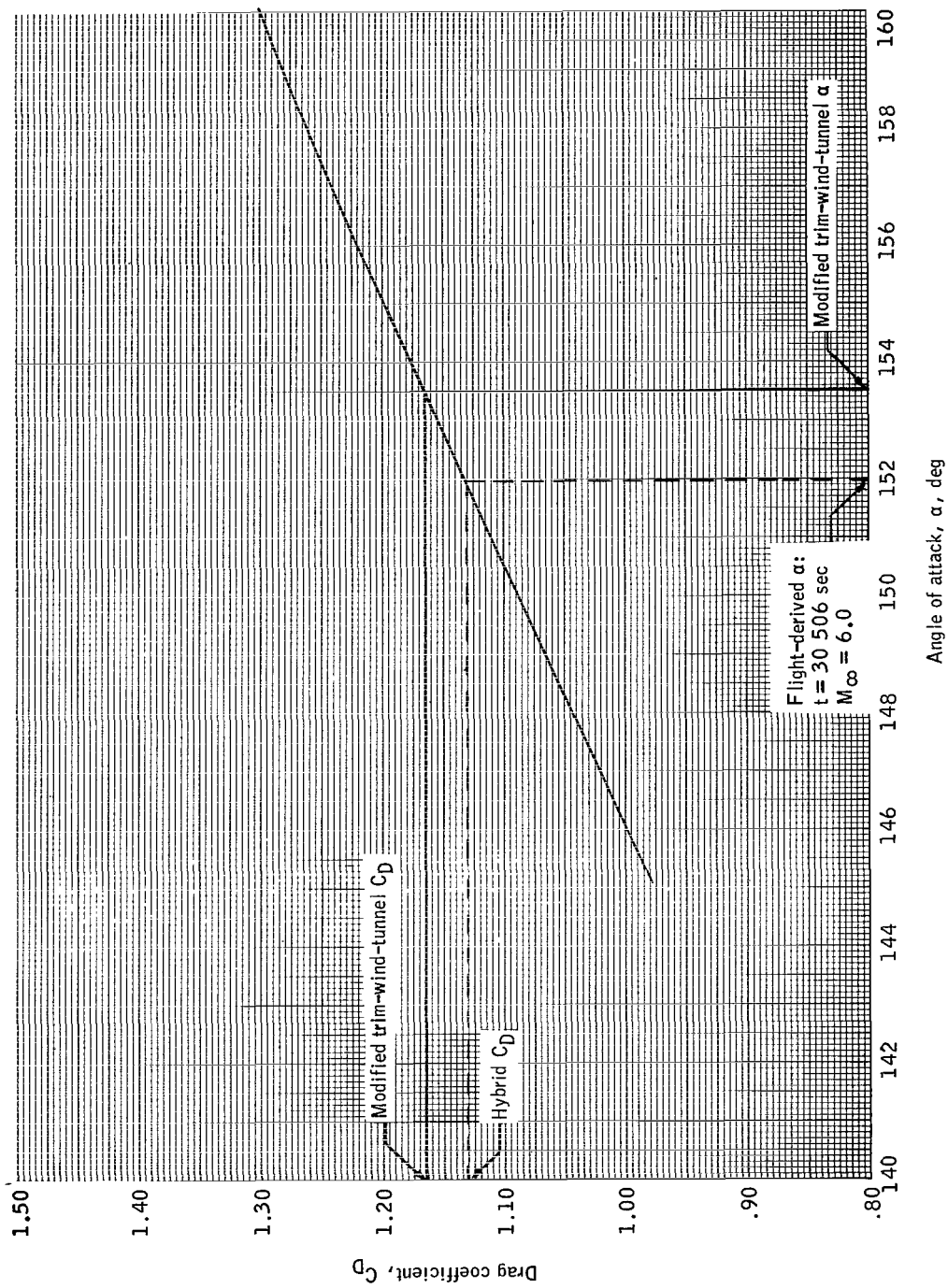
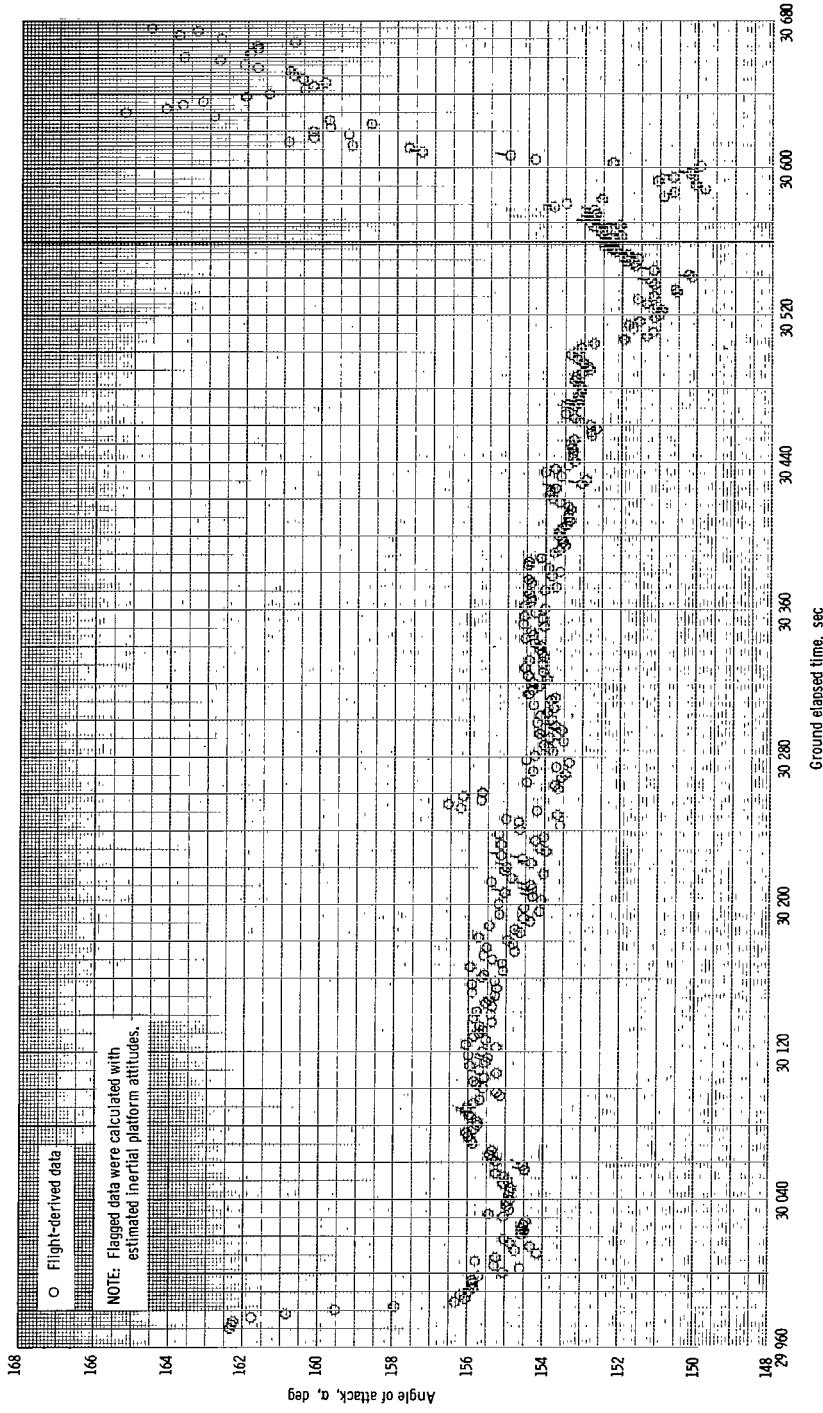
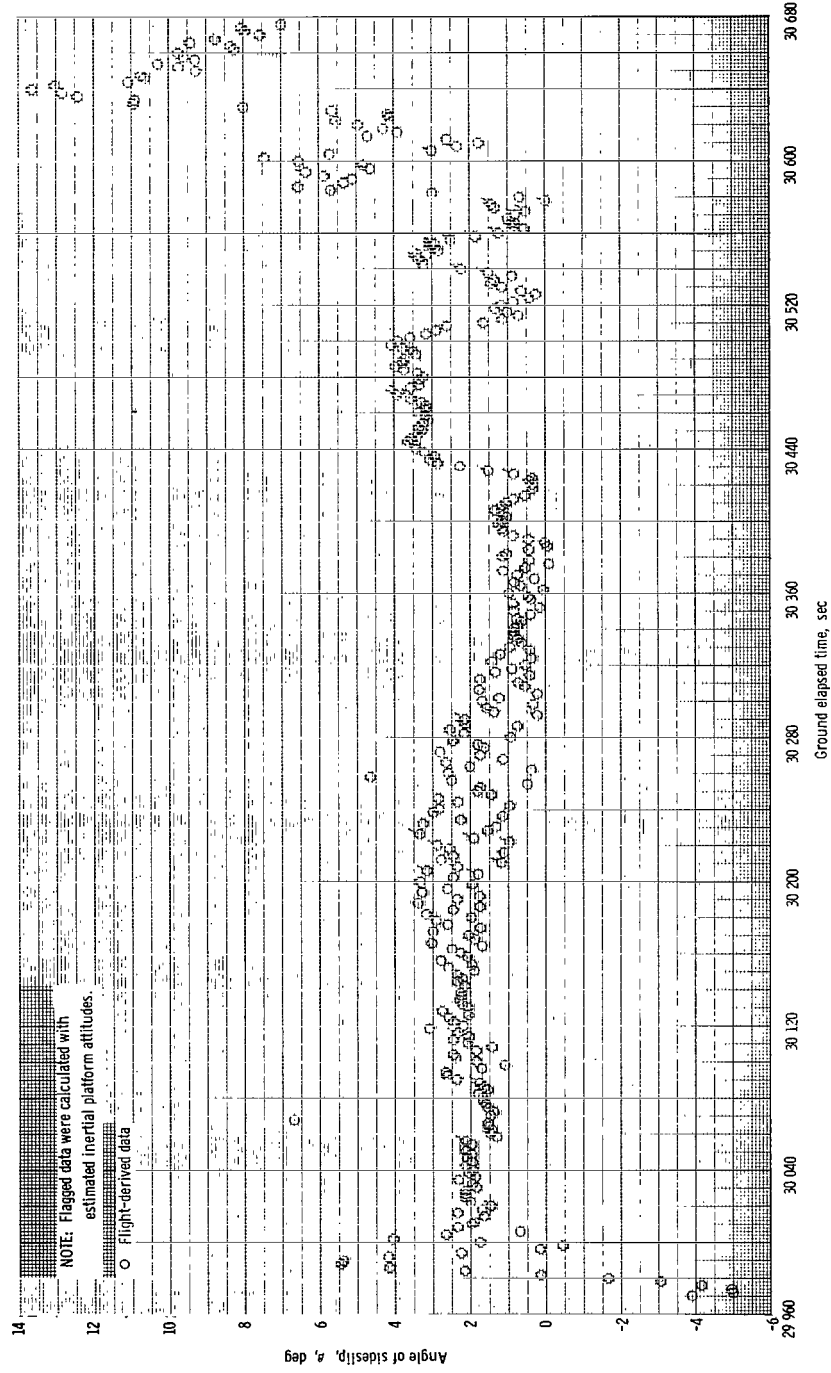


Figure 13. - Variation of modified trim-wind-tunnel drag coefficient  $C_D$  with test angle of attack  $\alpha$  for  $M_\infty = 6.0$ .



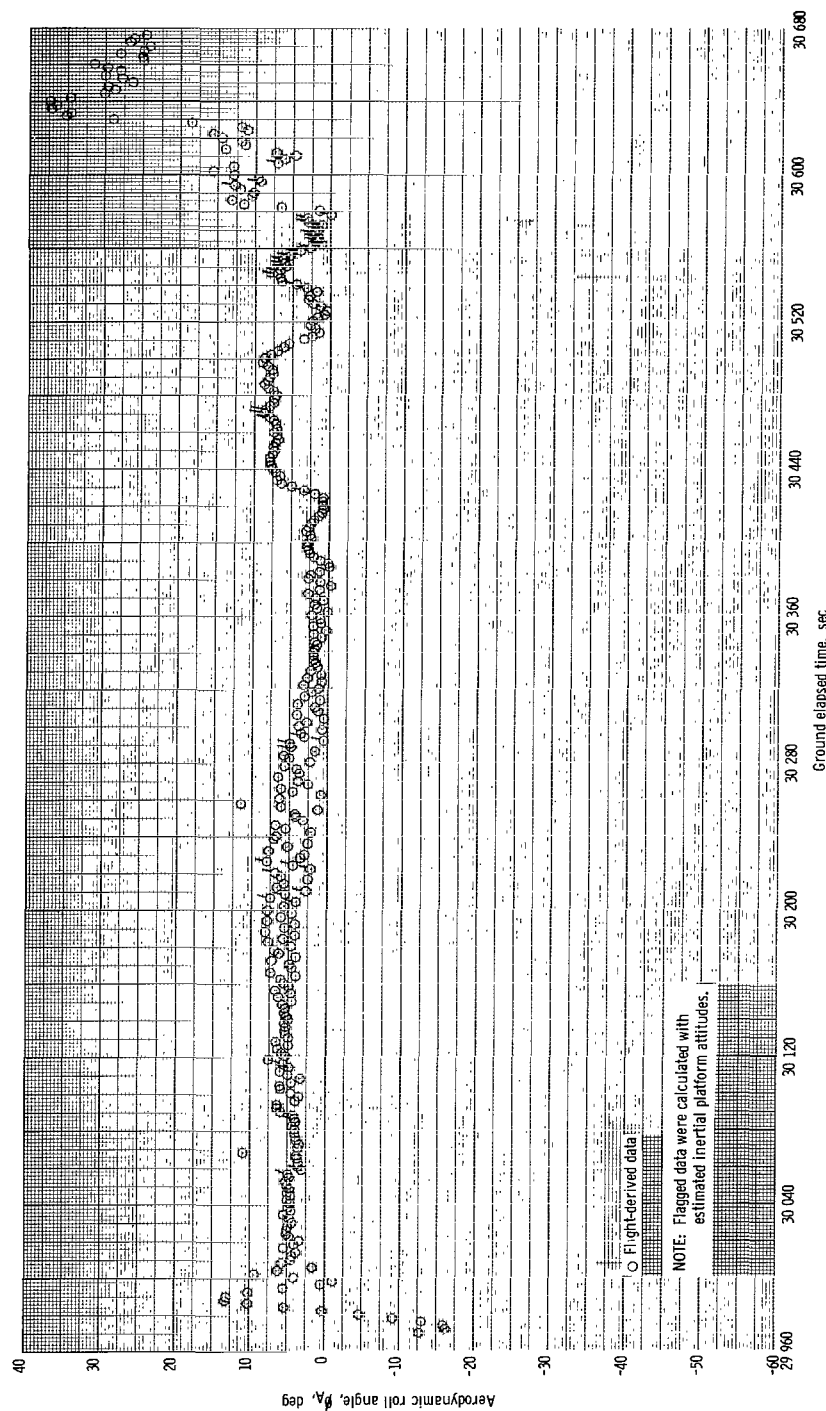
(a) Angle of attack  $\alpha$ .

Figure 14. - Time histories of aerodynamic angles.



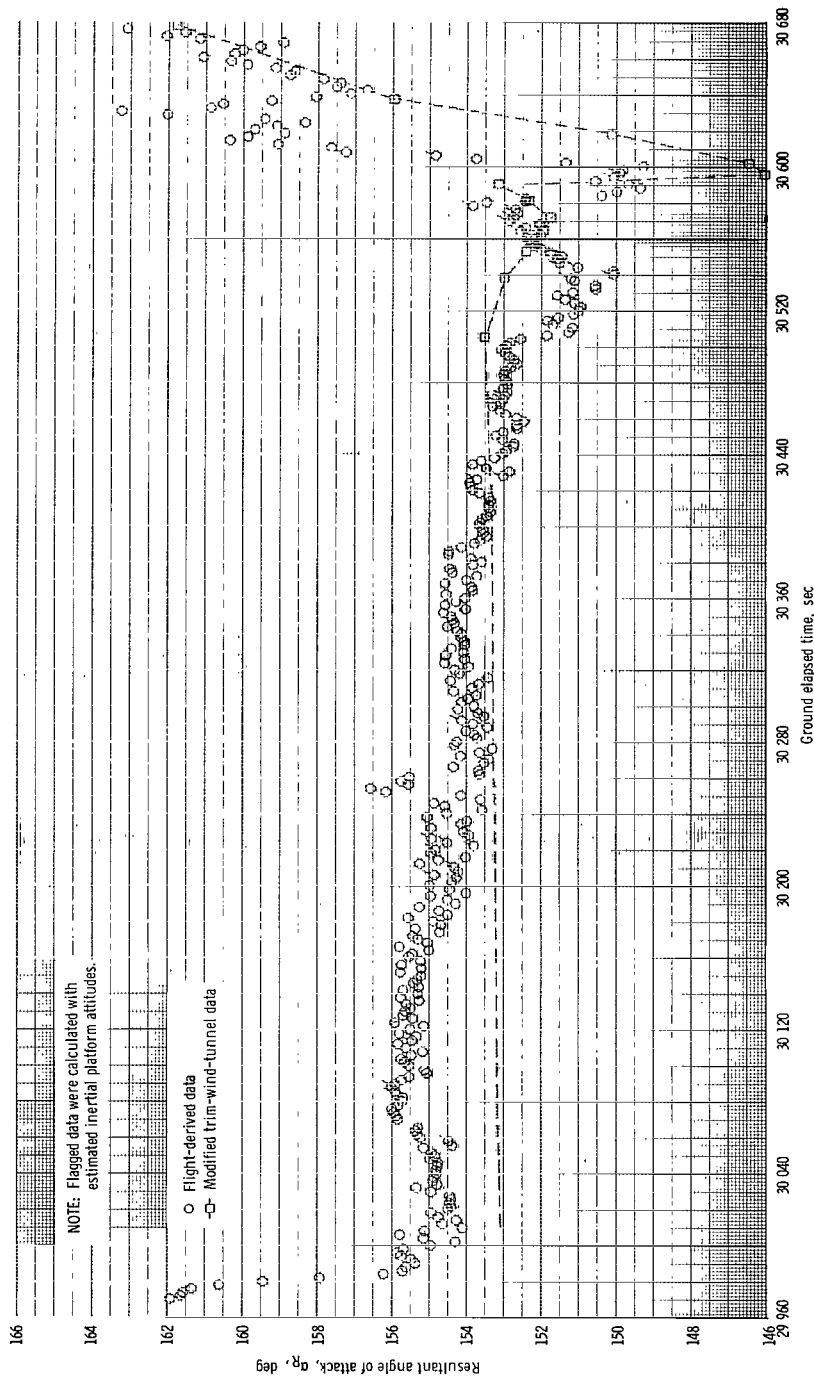
(b) Angle of sideslip  $\beta$ .

Figure 14. - Continued.



(c) Aerodynamic roll angle  $\phi_A$ .

Figure 14. - Continued.



(d) Resultant angle of attack  $\alpha_R$ .

Figure 14. - Concluded.

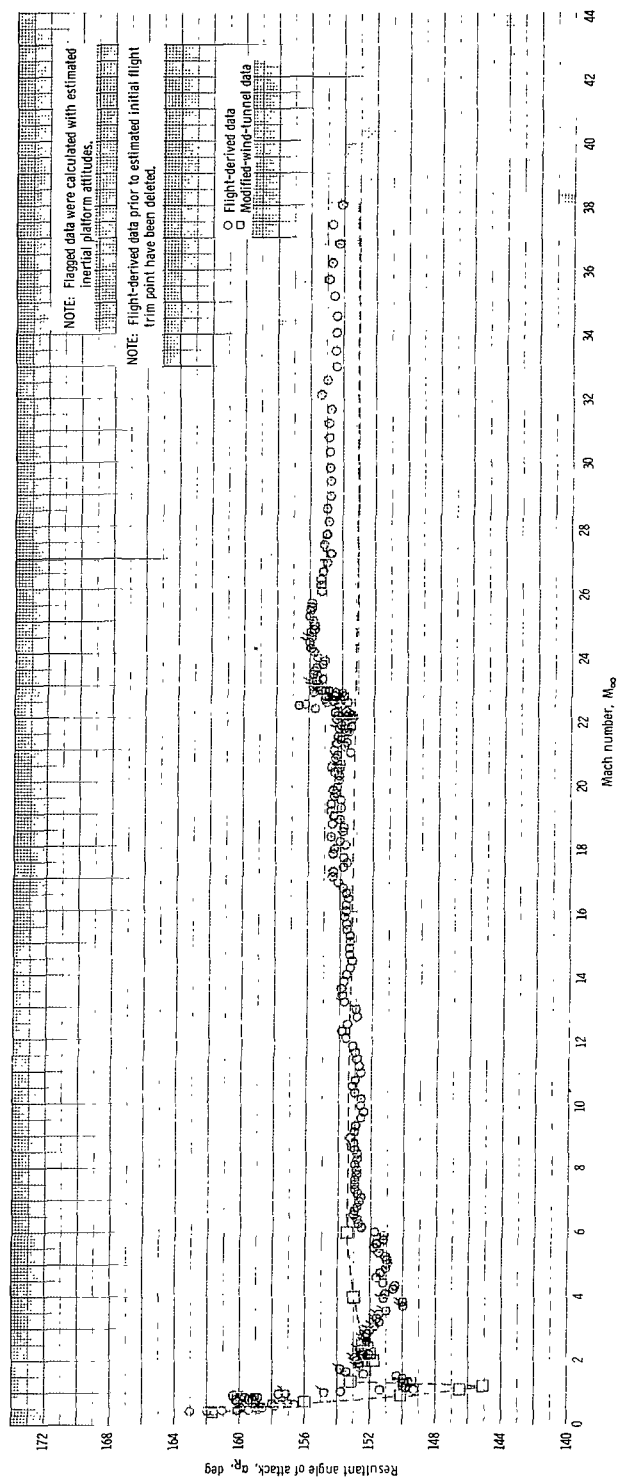
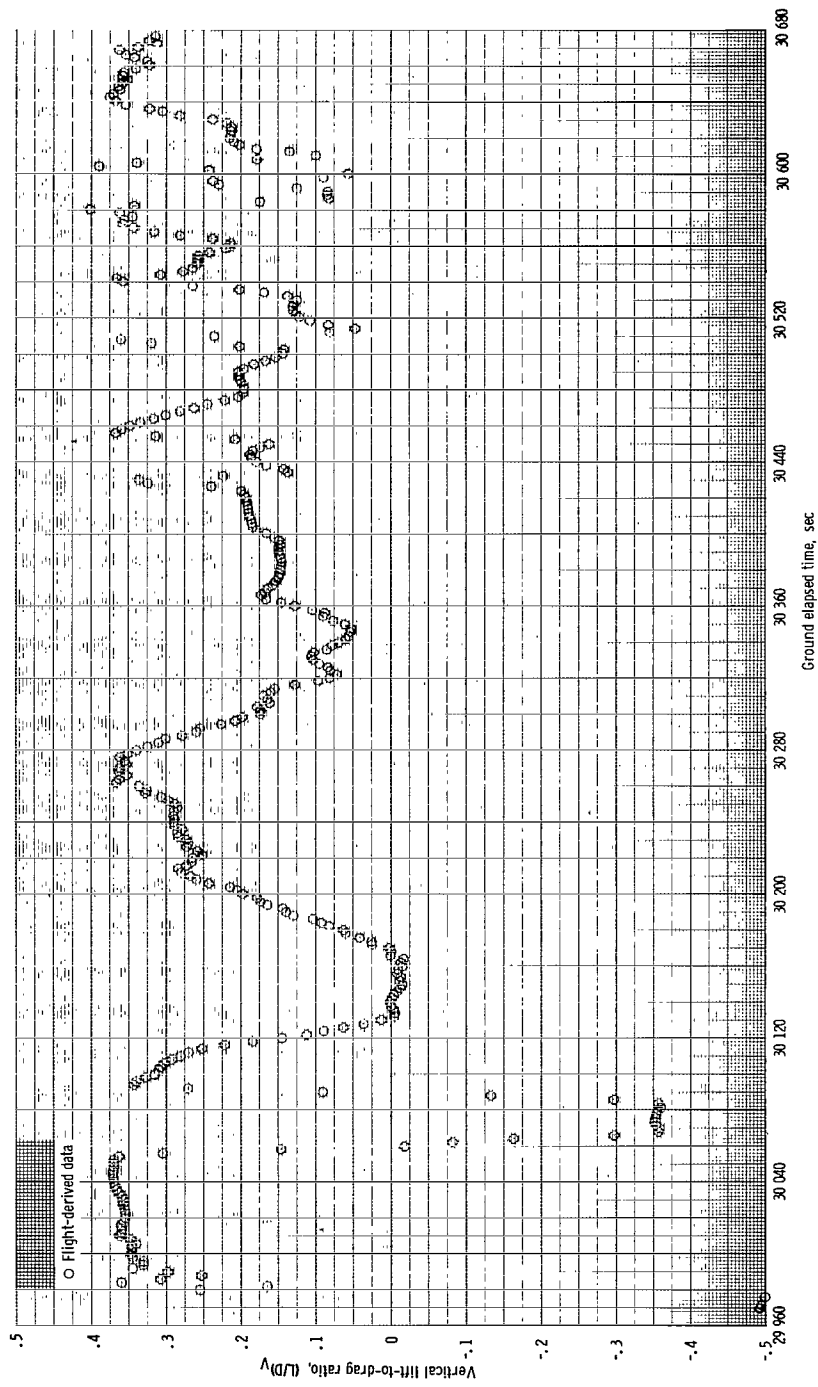
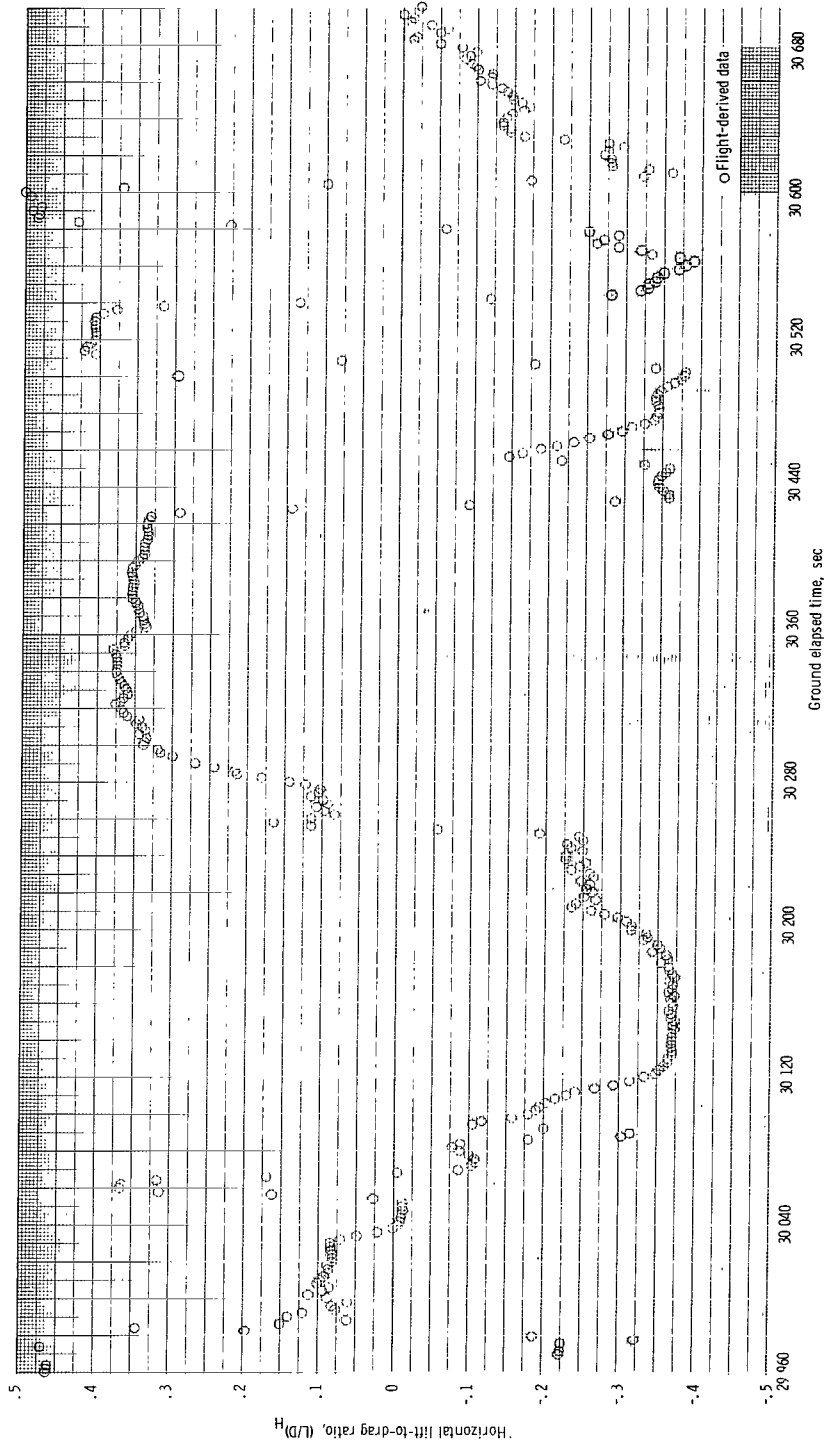


Figure 15. - Resultant angle of attack  $\alpha_R$  plotted against Mach number  $M_\infty$ .



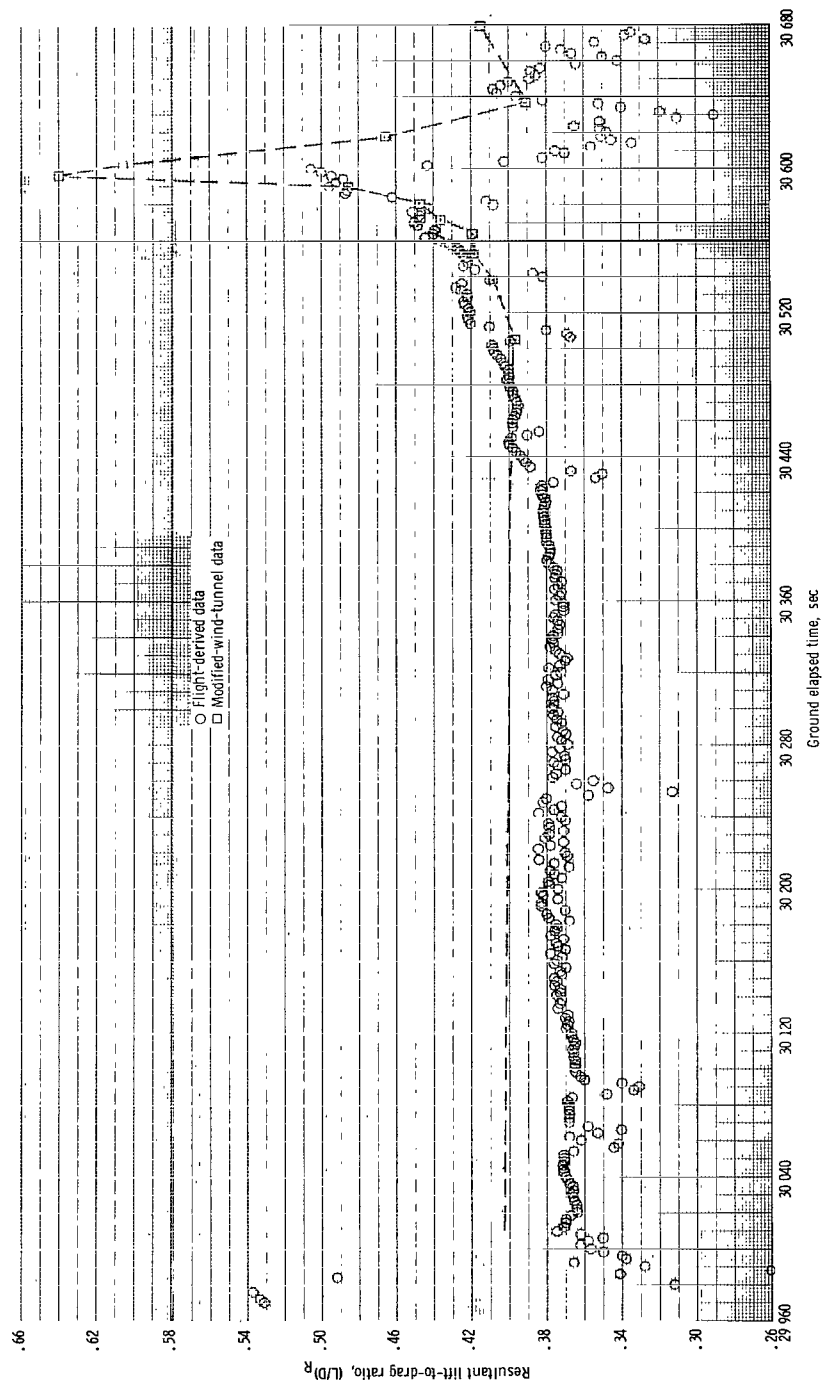
(a) Vertical lift-to-drag ratio  $(L/D)_V$

Figure 16. - Time histories of lift-to-drag ratios.



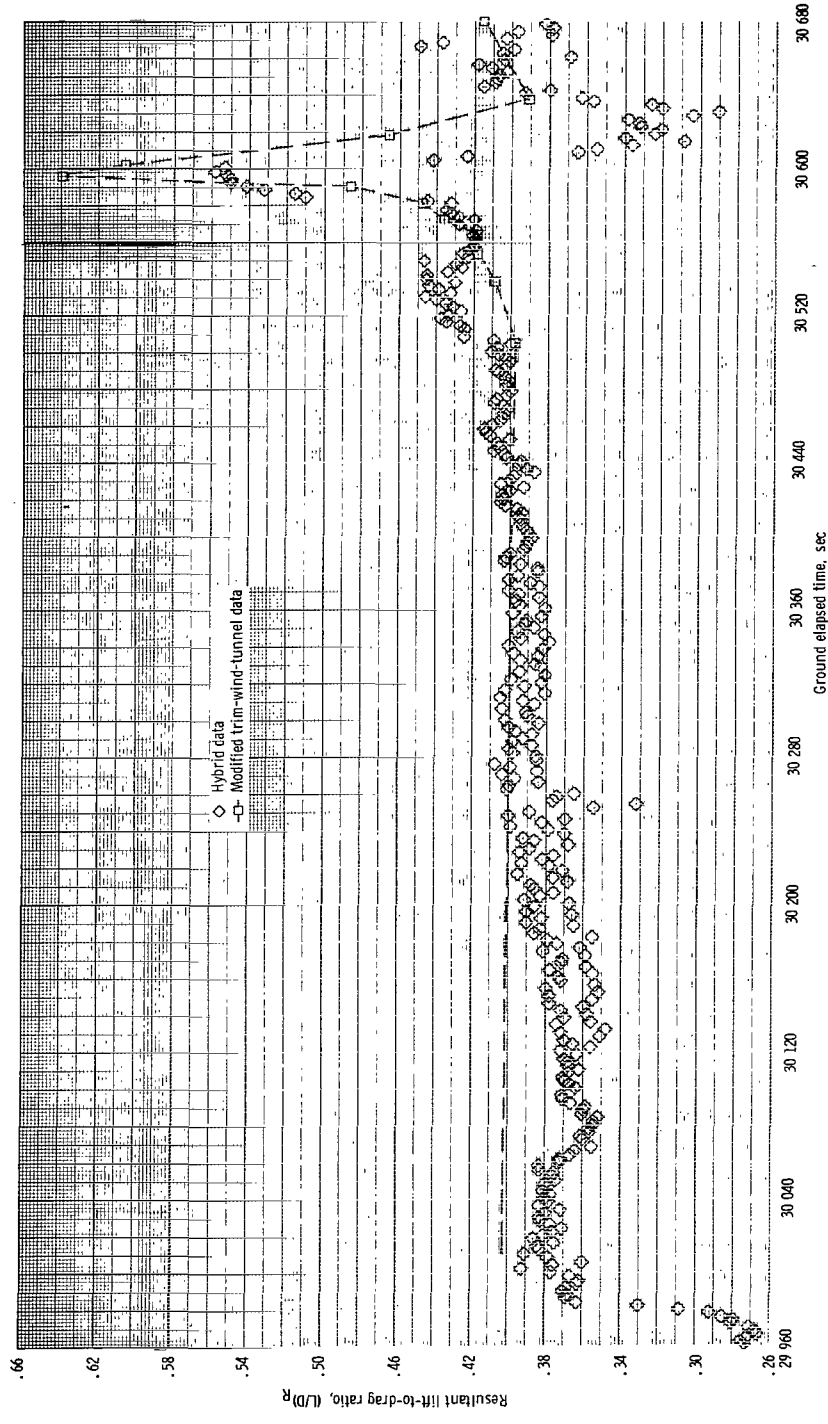
(b) Horizontal lift-to-drag ratio  $(L/D)_H$ .

Figure 16. - Continued.



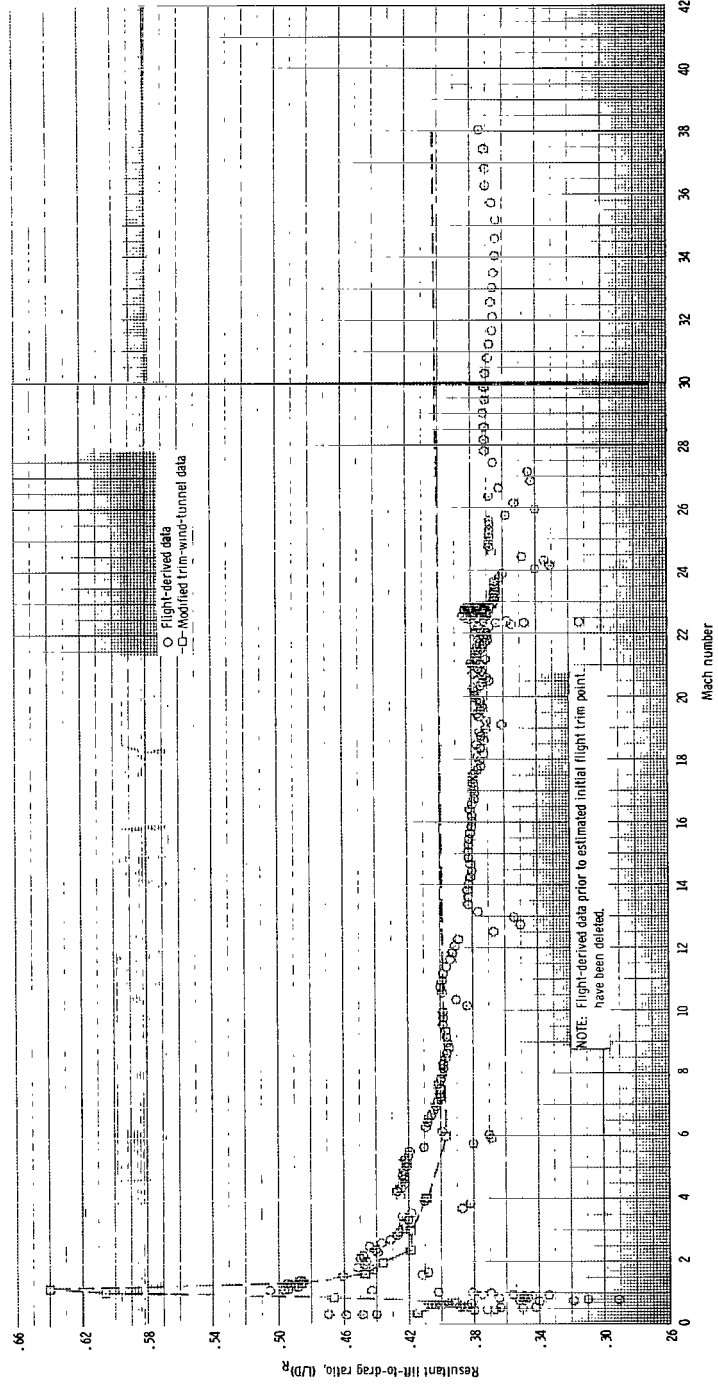
(c) Flight-derived resultant lift-to-drag ratio  $(L/D)_R$ .

Figure 16. - Continued.



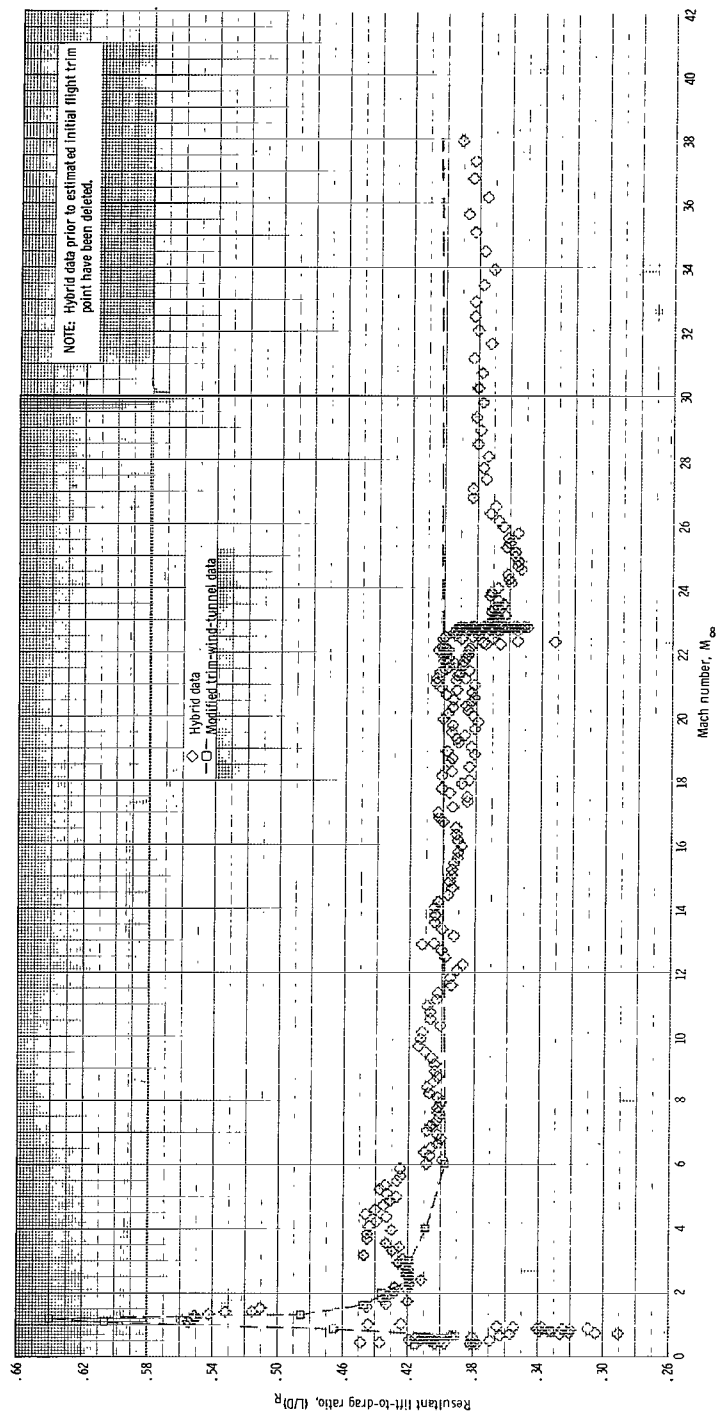
(d) Hybrid resultant lift-to-drag ratio  $(L/D)_R$ .

Figure 16. - Concluded.



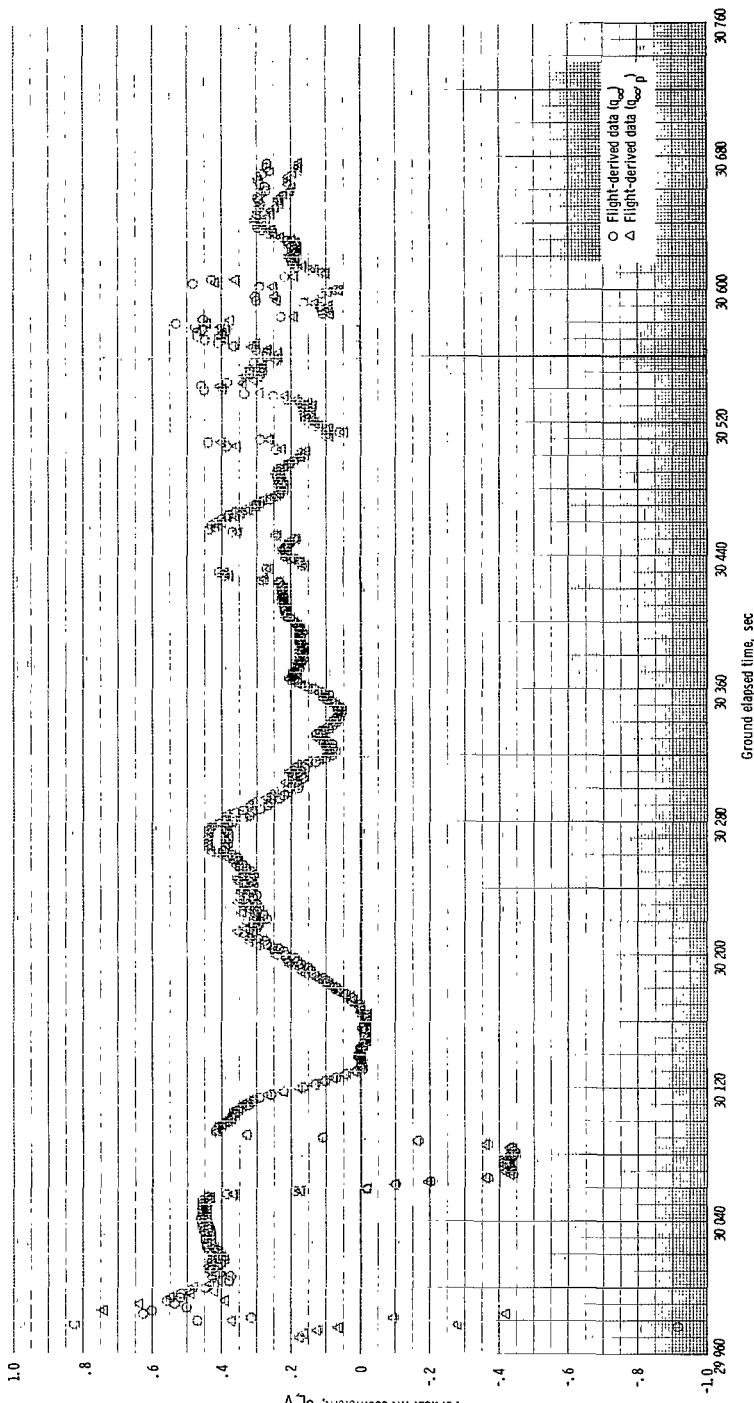
(a) Flight-derived lift-to-drag ratio  $(L/D)_R$ .

Figure 17. - Resultant lift-to-drag ratio  $(L/D)_R$  plotted against Mach number  $M_\infty$ .



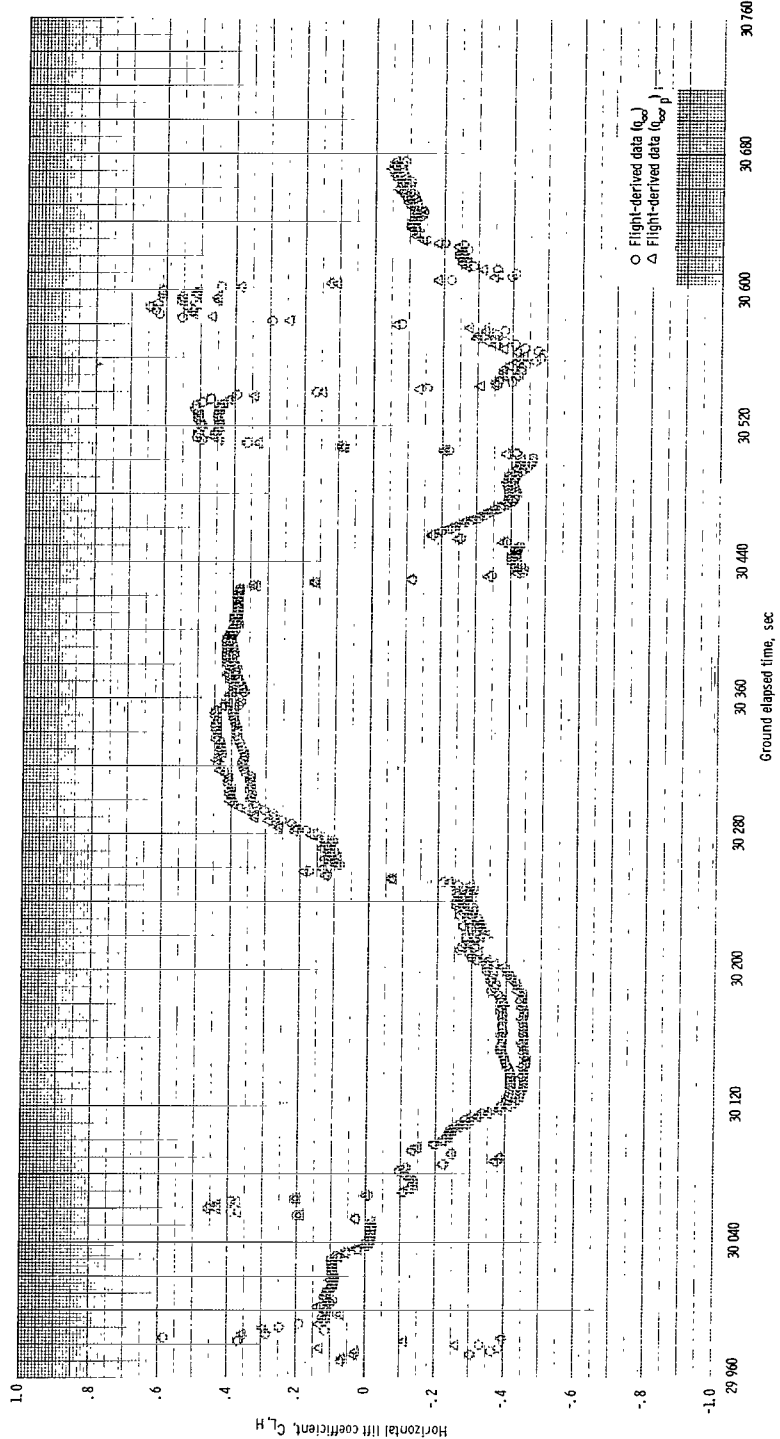
(b) Hybrid lift-to-drag ratio  $(L/D)_R$ .

Figure 17. - Concluded.



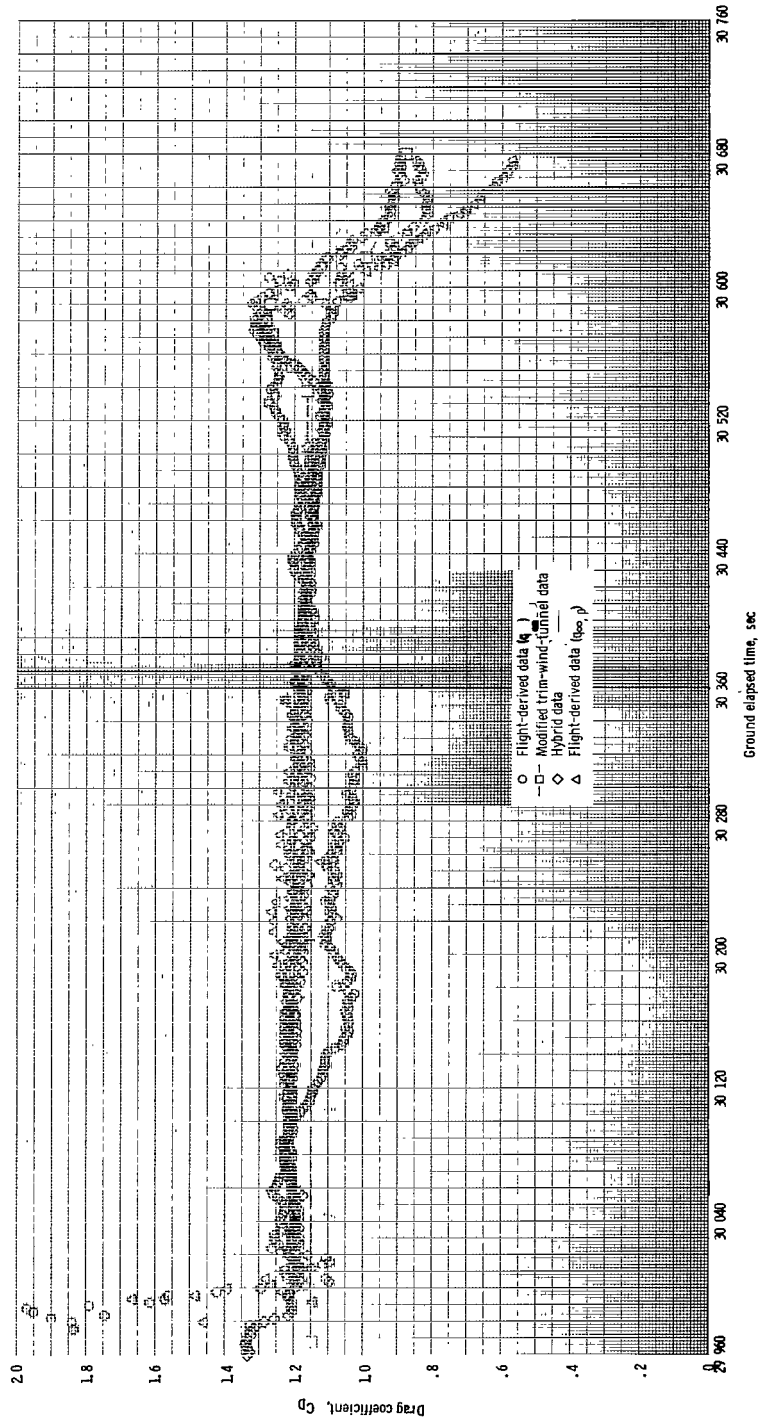
(a) Vertical lift coefficient  $C_{L,V}$

Figure 18. - Time histories of aerodynamic stability-axis force coefficients.



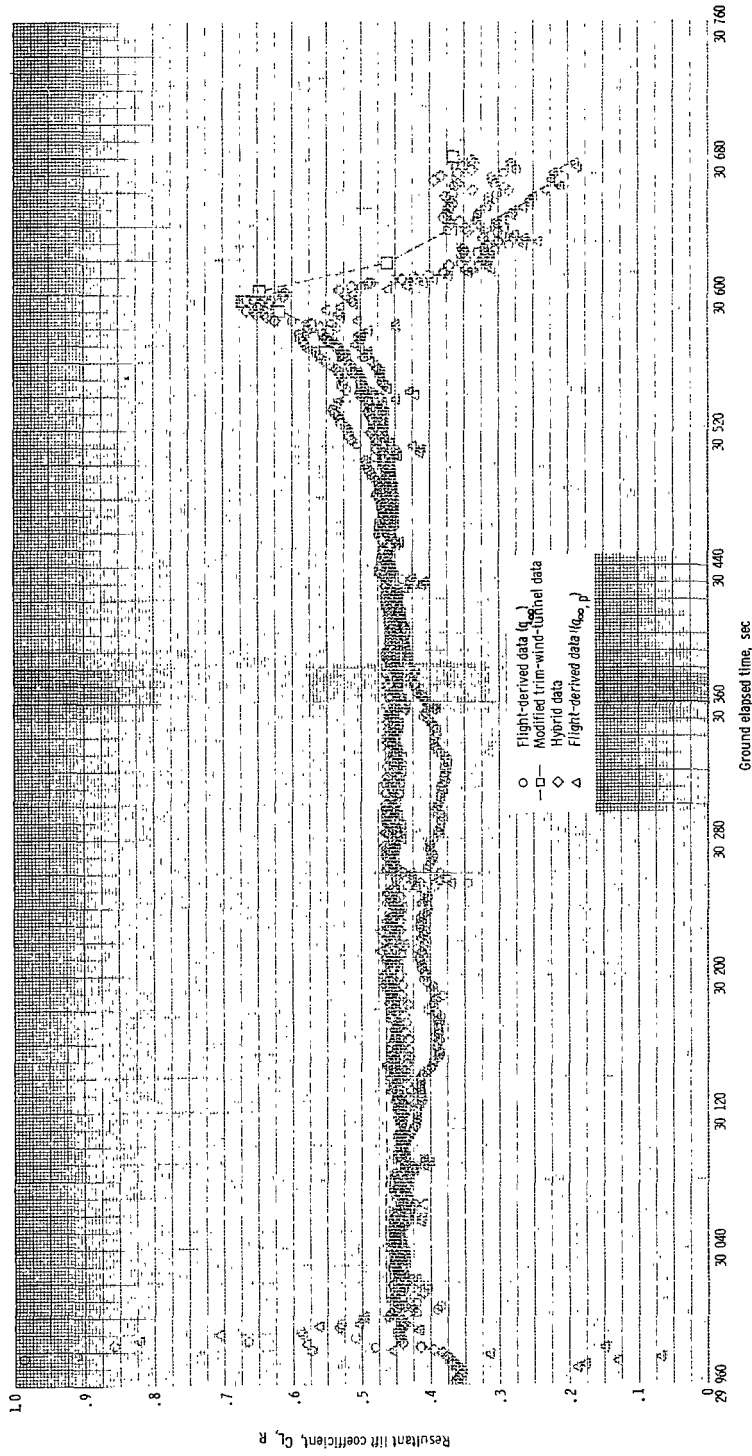
(b) Horizontal lift coefficient  $C_{L,H}$ .

Figure 18. - Continued.



(c) Drag coefficient  $C_D$ .

Figure 18. - Continued.



(d) Resultant lift coefficient  $C_{L,R}$ .

Figure 18. - Concluded.

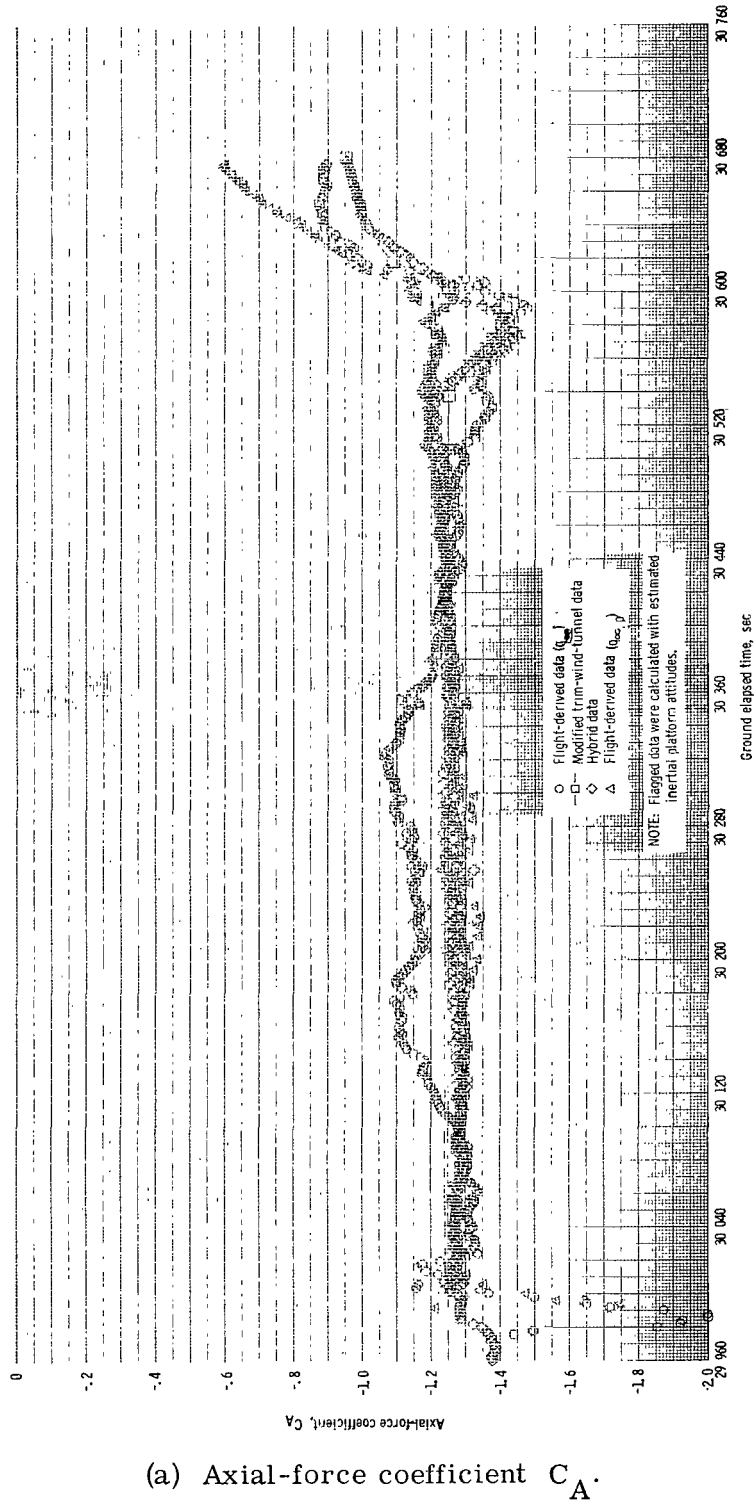
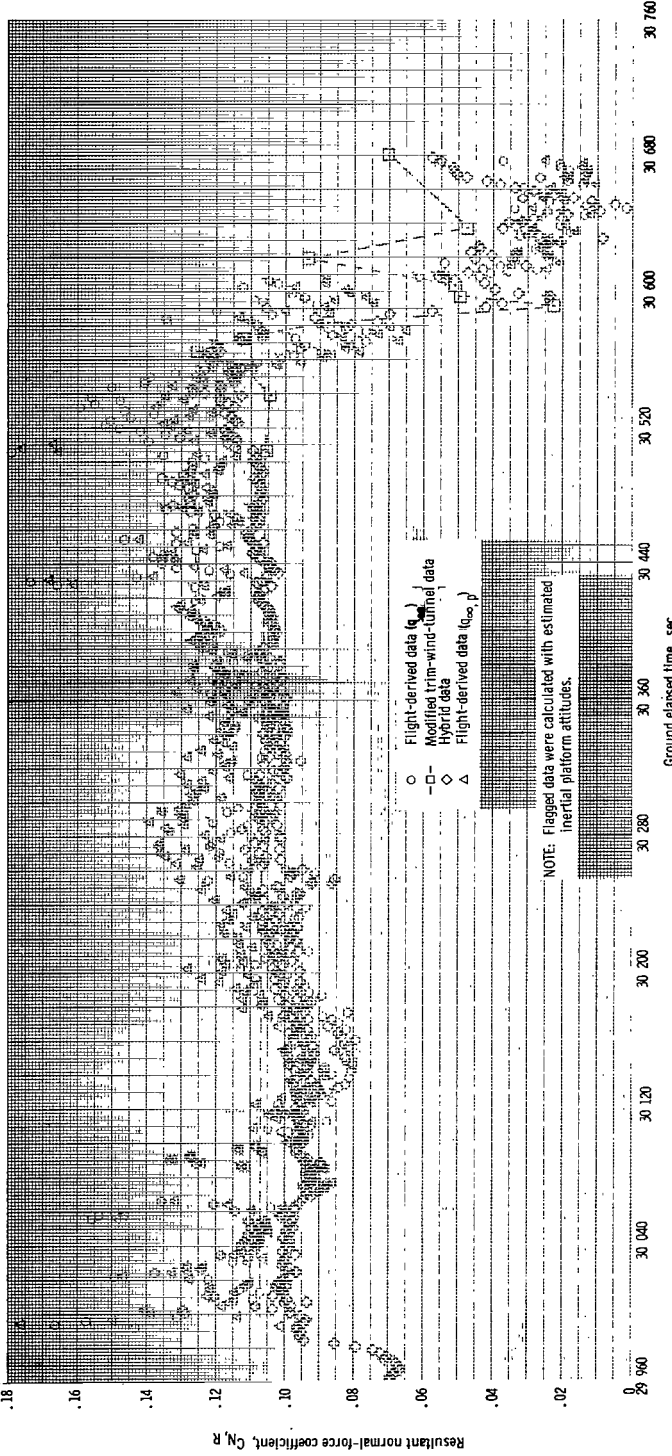
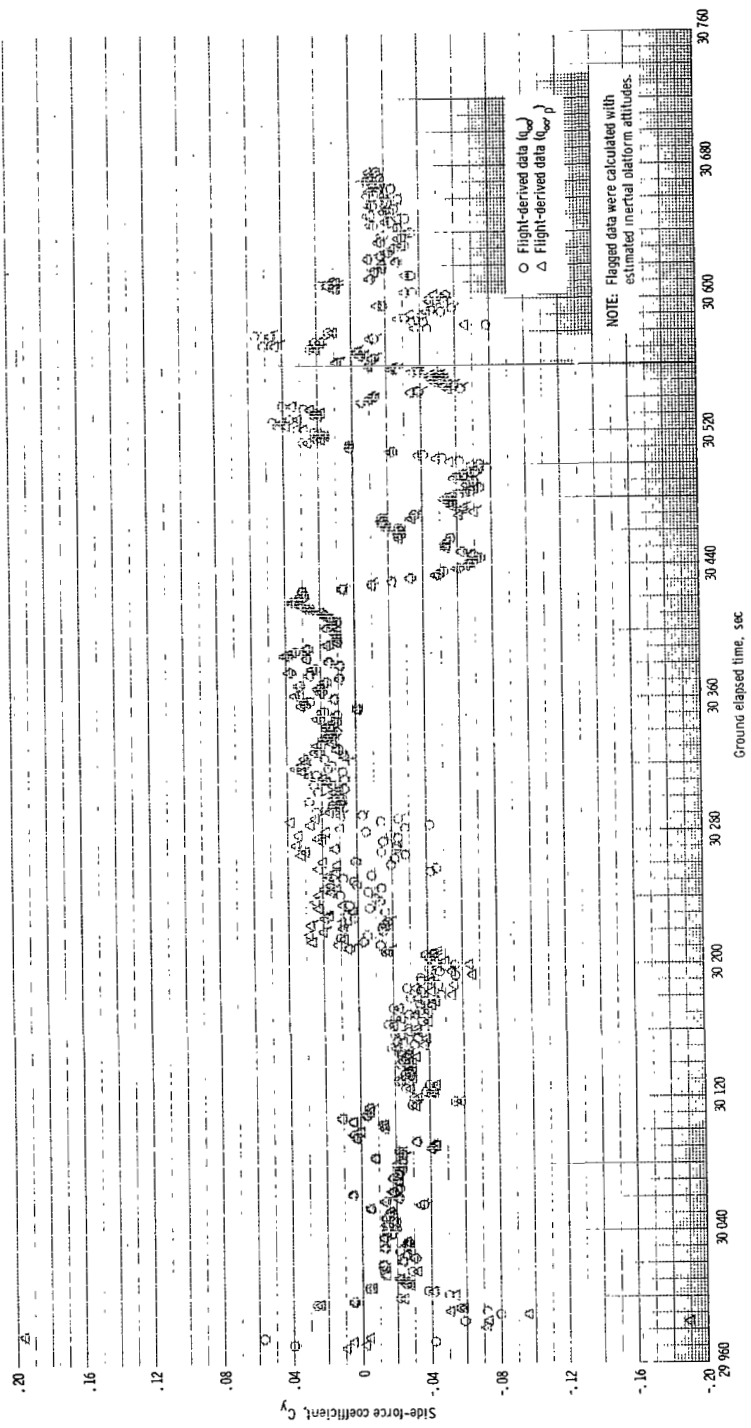


Figure 19. - Time histories of aerodynamic body-axis force coefficient.



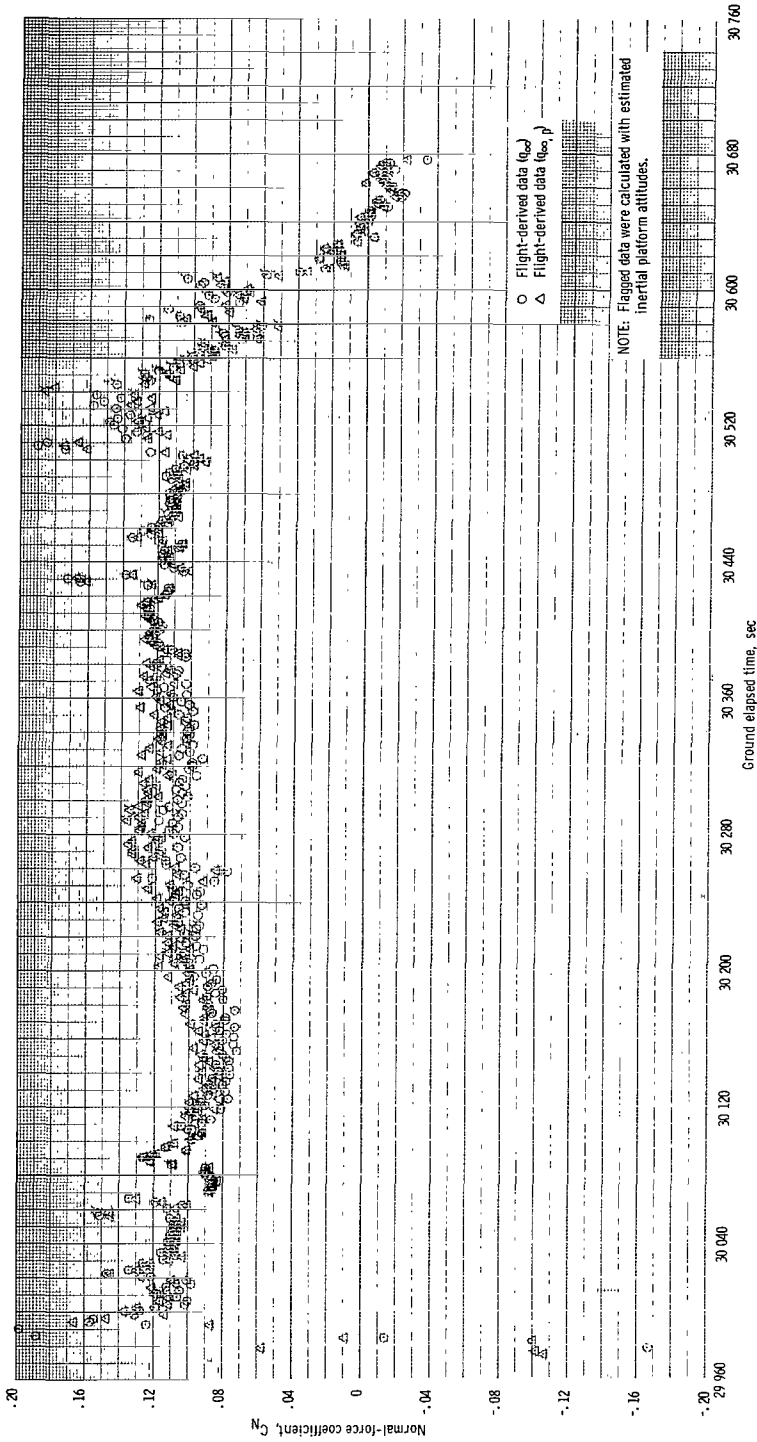
(b) Resultant normal-force coefficient  $C_{N,R}$ .

Figure 19. - Continued.



(c) Side-force coefficient  $C_Y$

Figure 19. - Continued.



(d) Normal-force coefficient  $C_N$ .

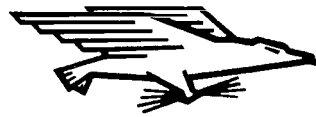
Figure 19. - Concluded.

NATIONAL AERONAUTICS AND SPACE ADMINISTRATION

WASHINGTON, D. C. 20546

OFFICIAL BUSINESS

FIRST CLASS MAIL



POSTAGE AND FEES PAID  
NATIONAL AERONAUTICS AND  
SPACE ADMINISTRATION

POSTMASTER: If Undeliverable (Section 158  
Postal Manual) Do Not Return

*"The aeronautical and space activities of the United States shall be conducted so as to contribute . . . to the expansion of human knowledge of phenomena in the atmosphere and space. The Administration shall provide for the widest practicable and appropriate dissemination of information concerning its activities and the results thereof."*

— NATIONAL AERONAUTICS AND SPACE ACT OF 1958

## NASA SCIENTIFIC AND TECHNICAL PUBLICATIONS

**TECHNICAL REPORTS:** Scientific and technical information considered important, complete, and a lasting contribution to existing knowledge.

**TECHNICAL NOTES:** Information less broad in scope but nevertheless of importance as a contribution to existing knowledge.

**TECHNICAL MEMORANDUMS:** Information receiving limited distribution because of preliminary data, security classification, or other reasons.

**CONTRACTOR REPORTS:** Scientific and technical information generated under a NASA contract or grant and considered an important contribution to existing knowledge.

**TECHNICAL TRANSLATIONS:** Information published in a foreign language considered to merit NASA distribution in English.

**SPECIAL PUBLICATIONS:** Information derived from or of value to NASA activities. Publications include conference proceedings, monographs, data compilations, handbooks, sourcebooks, and special bibliographies.

**TECHNOLOGY UTILIZATION PUBLICATIONS:** Information on technology used by NASA that may be of particular interest in commercial and other non-aerospace applications. Publications include Tech Briefs, Technology Utilization Reports and Notes, and Technology Surveys.

*Details on the availability of these publications may be obtained from:*

**SCIENTIFIC AND TECHNICAL INFORMATION DIVISION**  
**NATIONAL AERONAUTICS AND SPACE ADMINISTRATION**  
**Washington, D.C. 20546**